LBL-13650

Lawrence Berkeley Laboratory
UNIVERSITY OF CALIFORNIA

CHEMICAL BIODYNAMICS DIVISION

PHOTO-INDUCED ELECTRON-TRANSFER REACTIONS
IN HETEROGENEOUS MEDIA

RECEIVED
LAWRENCE
BERKELEY LABORATORY

JAN 20 1982

LIBRARY AND
DOCUMENTS SECTION

Jer-Ming Yang
(Ph.D. thesis)

November 1981

TWO-WEEK LOAN COPY

This is a Library Circulating Copy
which may be borrowed for two weeks.
For a personal retention copy, call
Tech. Info. Division, Ext. 6782

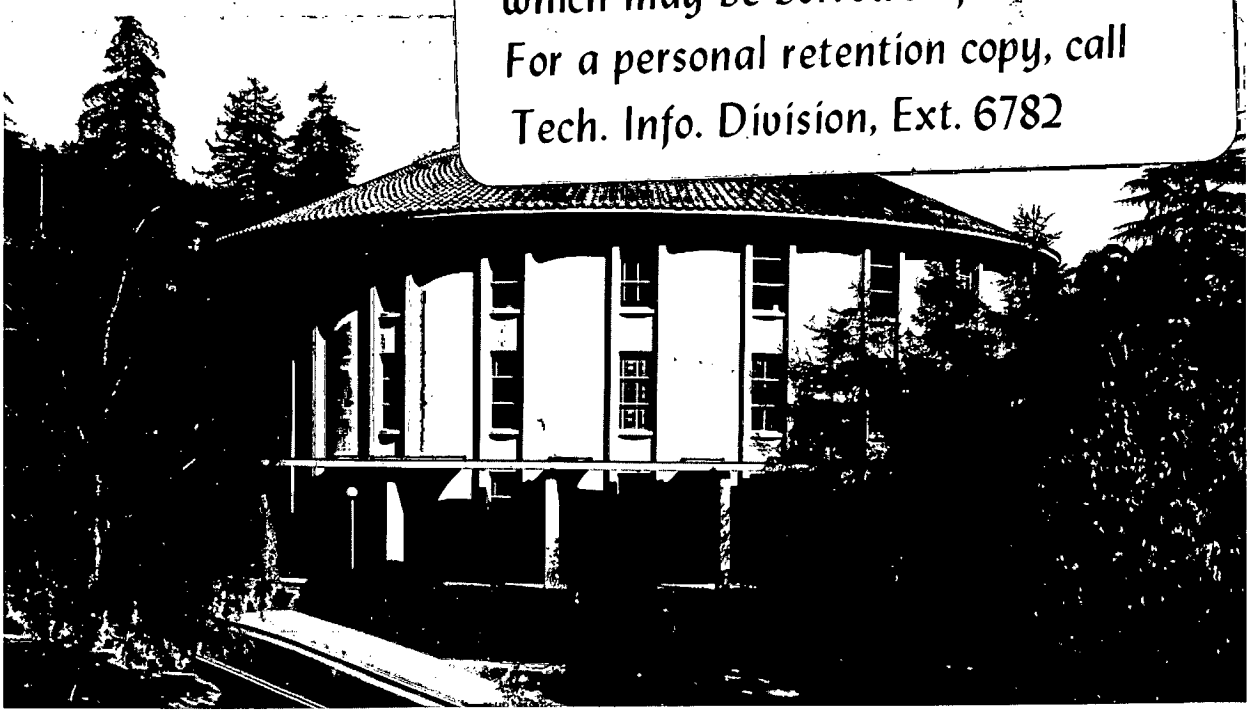

Prepared for the U.S. Department of Energy under Contract W-7405-ENG-48

LBL-13650 c.2

DISCLAIMER

This document was prepared as an account of work sponsored by the United States Government. While this document is believed to contain correct information, neither the United States Government nor any agency thereof, nor the Regents of the University of California, nor any of their employees, makes any warranty, express or implied, or assumes any legal responsibility for the accuracy, completeness, or usefulness of any information, apparatus, product, or process disclosed, or represents that its use would not infringe privately owned rights. Reference herein to any specific commercial product, process, or service by its trade name, trademark, manufacturer, or otherwise, does not necessarily constitute or imply its endorsement, recommendation, or favoring by the United States Government or any agency thereof, or the Regents of the University of California. The views and opinions of authors expressed herein do not necessarily state or reflect those of the United States Government or any agency thereof or the Regents of the University of California.

LBL-13650

PHOTO-INDUCED ELECTRON-TRANSFER REACTIONS IN HETEROGENEOUS MEDIA

Jer-Ming Yang

Ph.D. Thesis

November 1981

Chemical Biodynamics Division
Lawrence Berkeley Laboratory
University of California
Berkeley, CA 94720

This research was supported by the Division of Chemical Sciences, Office of Basic Energy Sciences of the U.S. Department of Energy under Contract W-7405-ENG-48.

Photo-Induced Electron-Transfer Reactions in Heterogeneous Media

by

Jer-Ming Yang

ABSTRACT

The conversion of solar energy into chemical energy has been pursued by two approaches. One is the photo-induced electron transfer reactions in heterogeneous media, and the other is the photo-decomposition of water with liquid-junction solar cells.

Photo-induced electron-transfer reactions in heterogeneous media with colloidal silica or poly-acrylate were studied by flash photolysis. The negative surface potential near silica particles greatly enhances the fluorescence quenching reaction between excited tris-(bipyridine)ruthenium(II) ($Ru(bpy)_3^{2+}$) and N,N'-dimethyl-4,4'-bipyridium (MV^{2+}) by concentrating both on the surface of the particles. With propylviologen sulfonate (PVS°) as the quencher, the back recombination reaction between $Ru(bpy)_3^{3+}$ and PVS^{-} was considerably retarded from a fast diffusion-controlled reaction in homogeneous solution ($k_b = 7.9 \times 10^9\ M^{-1}s^{-1}$) to a slow reaction in the presence of colloidal silica ($k_b = 5.7 \times 10^7\ M^{-1}s^{-1}$). In addition, the effects of surface potential were examined by varying the pH, temperature, and ionic strength. All the results are consistent with the existence of a high surface potential of about -180 mV near the interface. Similar effects were observed in the solution containing poly-acrylate, but the effect of electrostatic interactions on ionic reactions was not as strong. This is explained in terms of the lower surface potential on this poly-electrolyte.

As a sensitizer, zinc tetra(N-methyl-4-pyridyl)porphyrin ($ZnTMePyP^{4+}$) has not only a long-lived excited triplet state but also a high quantum efficiency of product separation from the solvent cage. By cyclic voltammetric measurement, the reduction potential of $ZnTMePyP^{5+}/ZnTMePyP^{4+}$ was determined to be +1.22 V versus saturated calomel electrode in acetonitrile. Such a high reduction potential is attributed to the difficulty in removing an electron from the porphyrin ring with four positively charged pyridinium substituents.

In an effort to illustrate that small band-gap semiconductors can be protected from photo-corrosion through surface modification, the surface of polycrystalline ZnO was chemically coated with zinc phthalocyanine and the electron-transfer process across the coated ZnO-electrolyte interface was studied by photo-electrochemical techniques. The results indicate that the polycrystalline photo-electrode retains most of the features of single crystal material as far as solar energy conversion is concerned, and electron transport through the space-charge layer of the semiconductor as well as across the solid-liquid interface can be influenced by surface modifications.

Since manganese complexes have been suggested to be the most probable candidate for the oxygen-formation catalyst in water decomposition and the epoxidation of organic substrates, the electrochemistry of manganese-containing porphyrins was studied by electrochemical techniques including a thin-layer, optically transparent electrode. From the absorption spectrum of the oxidized Mn(III) porphyrin and the heterogeneous electron-transfer rate constant, it was deduced that in the oxidation the electron originates from the central

Mn atom or a ligand orbital that interacts strongly with the central Mn atom.

M. Calvin

ACKNOWLEDGEMENTS

I wish to thank Professor Melvin Calvin for his stimulating advice and support during my graduate study. His boundless enthusiasm and critical insight were extremely helpful and influential towards my scientific education. I also thank Dr. John Otvos for his constant encouragement and many fruitful discussions. Especially, I would like to express my deep gratitude for the immense patience he has shown me to the completion of this thesis.

I am indebted to Professor Kenneth Sauer and Dr. Melvin Klein who have helped me in many experiments with their wealth of knowledge.

I must thank my wife Bea-Jane for her unfailing support and care through these years. Her confidence in me has sustained me during my graduate career and in difficult times.

I am also indebted to Ben Gordon, Mike Press, Dick O'Brien, Horace Olive, and Gary Smith who have aided me in several technical problems and given me invaluable lessons in perspective. I want to thank John McCracken for helping me construct my dye-laser flash photolysis apparatus. Thanks are due to Anne McGuire, Esther Yang, Mary Mclean, Esther Nemethy, Janet Splitter, David Baker, Craig Hodges, Hisao Yokota, and Tom Wydrzynski for their friendship.

Many thanks go to Everett Harvey and Beth Klingel for bringing out this thesis.

This research was supported by the Division of Chemical Sciences, Office of Basic Energy Sciences of the U.S. Department of Energy under contract W-7405-ENG-48.

To my parents

TABLE OF CONTENTS

Abstract	1
Acknowledgements	i
Dedication	ii
Table of Contents	iv
I. Introduction	1
References	6
II. General Experimental	7
1. Electrochemistry	7
2. Excited-State Lifetime Measurements	15
3. Flash Photolysis	20
References and Notes	49
III. Photo-Induced Electron-Transfer Reactions in Homogeneous Solutions	50
Experimental	55
Results and Discussion	57
(1) Fluorescence quenching experiments	57
(2) Continuous photolysis studies	57
(3) Flash photolysis studies	63
Appendix	85
References	93
IV. Photo-Induced Electron Transfer Reactions in Heterogeneous Media	94
Experimental	98
Results and Discussion	101

Part A. Photochemistry in colloidal Silica 101

(1) Characteristics of colloidal silica 101

(2) Electrochemistry 105

(3) Excited-state lifetime measurements 105

(4) Fluorescence quenching studies 114

(5) Flash photolysis studies in solutions containing colloidal silica 122

(6) Summary 148

Part B. Photochemistry in polyelectrolytes 152

(1) Electrochemistry of $ZnTMePyP^{4+}$ 152

(2) With $Ru(bpy)_3^{2+}$ as the sensitizer 158

(3) With $ZnTMePyP^{4+}$ as the sensitizer 161

(4) Summary 170

References 171

V. Liquid-Junction Solar Cell 173

5.1 Introduction 173

5.2.1 Some basic notions on semiconductors 175

5.2.2 Electrochemistry of zinc oxide 179

5.3 Experimental 190

5.4 Results and Discussion 196

References 221

VI. Electrochemical Studies of Manganese (III) Porphyrin 223

Experimental 223

Results and Discussion 224

References 233

CHAPTER 1

INTRODUCTION

Since the dawn of our living world, the sun has continuously furnished us with all the energy necessary for survival and growth. In the past, the supply of solar energy was more than enough, and the excess was cleverly saved as fossil fuels through photosynthesis. However, as our society evolves with the expanding population, the energy demands will soon no longer be met by the current energy supply from photosynthesis and other resources such as the depleting fossil energy. Now, it is time for us to seek ways of increasing the rate of solar energy harvesting before we can develop and securely handle nuclear energy [1].

In this study, I have been interested in converting solar energy into chemical fuels either via the electronic excitation of dye molecules in solution or via the band-gap excitation of semiconductors. Following these excitations, many possible reactions may ensue to store energy. Among them, the decomposition of water (eq.1) into hydrogen and oxygen will be emphasized mainly because water is ubiquitous and hydrogen is a non-polluting fuel.

$$2\ H_2O \xrightarrow{h\nu} 2\ H_2 + O_2 \qquad (1)$$

However, water decomposition is not as simple a reaction as it may look. Because water is transparent to solar radiation in the ultraviolet and visible region, a direct photolysis is not feasible and the reaction must be sensitized by redox dye catalysts. After the photo-induced electron-transfer reaction takes place between the excited dye and a quencher, at least two more continuing reactions are necessary

to split water, i.e.

$$2\ A^- + 2\ H_2O \longrightarrow 2\ A + 2\ OH^- + H_2 \qquad (2)$$

$$4\ D^+ + 2\ H_2O \longrightarrow 4\ D + 4\ H^+ + O_2 \qquad (3)$$

These involve a two-electron reductive reaction and a four-electron oxidative reaction, respectively. Without wasting some electrochemical energy in driving the reactions forwards or without some specific catalysts present, they will not proceed at practical rates.

Recently, a number of homogeneous and micro-heterogeneous solutions with ultrafine catalysts have been reported to produce hydrogen from water under solar irradiation in the presence of a sacrificial electron donor [2]. These ultrafine catalysts (~30 Å) can be evenly dispersed in aqueous solutions so that reaction 2 may proceed with a near diffusion-controlled rate. So far, reaction 3 for the oxygen evolution still is the limiting factor in this approach. Although this reaction was found to be catalyzed by PtO_2, IrO_2 [3], and RuO_2 [4], the rates were low. In order to complete the cycle of a dye-sensitized photo-decomposition of water, more specific homogeneous catalysts such as polynuclear complexes should be designed and synthesized to participate in this multi-electron-transfer reaction [5].

In addition to the dye-sensitized decomposition of water, several cyclic chemical reactions have been discussed by Balzani et al. [6]. Using water or its dissociated ions as the quencher, they have determined the threshold energy of 420 nm for the cycles involving binuclear complexes and of 841 nm for those with hydrido complexes. Alternatively, Bolton and others propose a system with two photochemical centers, which is in analogy to natural photosynthesis [7]. For this coupled process, the threshold energy even including an

unavoidable loss of 0.8 eV for the driving force can be shifted toward the near-infrared region (~877 nm).

My approach is to carefully and individually study each of the reactions involved in a dye-sensitized photodecomposition of water so that an optimized system can be designed later on. In studying these electron-transfer reactions, several techniques and instruments are essential, e.g., the measurement of the excited-state lifetime of a sensitizer by a nanosecond flash lamp, the study of excited-state quenching reactions with a fluorimeter, the investigation of fast redox reactions by a flash photolysis setup, and the determination of the redox potentials of reactants by electrochemical techniques. Most of these will be summarized in chapter 2 as a general experimental reference to other chapters.

In chapter 3, some photo-induced electron-transfer reactions in homogeneous solutions will be examined. From the results obtained in this simple system, one realizes that the back electron-transfer reaction (eq. 6) following the initial quenching reaction (eq. 5) is the most serious obstacle to achieving a higher conversion efficiency.

$$\text{Dye} + h\nu \longrightarrow {}^{*}\text{Dye} \qquad (4)$$

$$^{*}\text{Dye} + \text{A} \longrightarrow \text{Dye}^{+} + \text{A}^{-} \qquad (5)$$

$$\text{Dye}^{+} + \text{A}^{-} \longrightarrow \text{Dye} + \text{A} \qquad (6)$$

In order to retard the undesired back reaction and to allow the reactants to react selectively, heterogeneous media are introduced and the photochemistry in such media is discussed in chapter 4. In my experiments, heterogeneous media with either colloidal silica or polyacrylate were found to influence the ionic reactions strongly. These media typically consist of two sub-phases with a charged interface.

For instance, the solution containing dispersed colloidal silica has a micro solid phase, a bulk phase, and a charged silanol interface in between. Through the electrostatic interactions, ions can be concentrated near the interface or repelled away into the bulk solution. In this way, the course of reaction is guided and the reaction rates can be accelerated or retarded at will. More importantly, the inclusion of a second micro phase allows us to have more freedom in designing the system. For example, the hydrophobic core in the micelle permits the solubilization of organic reactants in the aqueous micellar solution, and the semiconducting properties of dispersed semiconductor particles help the charge separation in dye-sensitized reactions [8].

In chapter 5, liquid-junction solar cells for converting solar energy into chemical fuels will be discussed. These solar devices consist of a semiconductor electrode immersed in a liquid solution containing a conducting counter electrode. The circuit is completed by connecting an external wire between these two electrodes. In such a device, photo-generated electron-hole pairs in the space-charge layer of the semiconductor are effectively separated by the built-in electric field. For instance, in an n-type semiconductor, the electron is first swept into the bulk of the semiconductor and then travels through the external conducting wire to reach the counter electrode. If the semiconductor is properly chosen with a flat-band potential more negative than that of the $H^+/H_{2(g)}$ couple, this electron may reduce water on the counter electrode. In the mean time, the photo-generated hole is attracted to the semiconductor surface, where it may oxidize water or other substrates. In this study, I am particularly interested in protecting small band-gap semiconductors from photo-dissolution so

that they can be utilized in absorbing solar energy while staying intact in aqueous solutions.

In chapter 6, heterogeneous electron-transfer reactions between manganese porphyrin and metal electrode are examined by cyclic voltammetric techniques and a thin-layer optically transparent electrode. From the measured heterogeneous electron-transfer rate constant and the optical spectrum, some indication of whether the oxidized manganese porphyrin is composed of a Mn(IV) with an intact porphyrin ring or a Mn(III) with an oxidized porphyrin ring will be discussed.

References

1. M. Calvin, 'Synthetic Chloroplasts' in Faraday Discussions of the Royal Society of Chemistry, 70, 383 (1980).

2. (a) P.-A. Brugger, P. Cuendet, and M. Grätzel, J. Amer. Chem. Soc., 103, 2923 (1981).

   (b) M. Kirsch, J. M. Lehn, and J. P. Sauvage, Helv. Chim. Acta, 62, 1345 (1979).

3. J. Kiwi and M. Grätzel, Angew. Chem., Int. Ed. Engl., 17, 860 (1978).

4. (a) J. Kiwi and M. Grätzel, Angew. Chem., 91, 659 (1979).

   (b) J. M. Lehn, J. P. Sauvage, and R. Ziessel, Nouv. J. Chim., 3, 423 (1979).

5. J. P. Collman, P. Denisevich, Y. Konai, M. Marrocco, C. Koval, and F. C. Anson, J. Amer. Chem. Soc., 102, 6027 (1980).

6. V. Balzani, L. Moggi, M. F. Manfrin, F. Bolletta, and M. Gleria, Science, 189, 852 (1975).

7. J. R. Bolton, Science, 202, 705 (1978).

8. (a) M. T. Spitler and M. Calvin, J. Chem. Phys., 66, 4294 (1977).

   (b) I. Izumi, W. W. Dunn, K. O. Wilbourn, F.-R. F. Fan, and A. J. Bard, J. Phys. Chem., 84, 3207 (1980).

CHAPTER II

GENERAL EXPERIMENTAL

1. Electrochemistry

In the past ten years, electrochemical techniques have been increasingly used in the studies of photo-sensitized reactions on semiconductors and electron-transfer reactions on polymer- or catalyst-coated electrodes in addition to the traditional applications in the various fields of chemistry. Their versatility and popularity are established on the advent of the well-developed transition-state theory of electrode processes and modern electronic instrumentation. Through these quantitative treatments, detailed characterization of chemical species and dynamic processes in the solution phase is made possible.

Since electron-transfer reactions are of primary concern in this study, the determination of the redox potentials as well as the reversibility of a redox reaction will be stressed. With regard to these two aspects, cyclic voltammetry is considered to be the most convenient and informative tool among all the possible electrochemical techniques.

The theory of cyclic voltammetry on the stationary electrode applied to reversible, quasi-reversible, and irreversible systems has been developed by Nicholson and Shain [1]. Those results on the first two systems will be summarized here as a general background for the subsequent electrochemical studies.

A. Reversible charge transfer

First, consider a system with a reversible redox couple in the solution containing an excess of supporting electrolyte.

$$Ox + ne^- \rightleftharpoons Red$$

The concentrations of the redox couple, Ox and Red, on the surface of electrode are determined by the Nernst equation. Solving the boundary value problem of a semi-infinite linear diffusion, one obtains the following two equations which express the concentrations of electro-active species in terms of the current at time t, i(t), and other parameters [2].

$$C_O(0,t) = C_O^* - \int_0^t \frac{i(\tau)\, d\tau}{nFA\,(\pi D_O\{t-\tau\})^{1/2}}$$

$$C_R(0,t) = C_R^* + \int_0^t \frac{i(\tau)\, d\tau}{nFA\,(\pi D_R\{t-\tau\})^{1/2}}$$

where C_O and C_R denote the concentrations of the oxidized and reduced species, and C_O^* and C_R^* are the concentrations in the bulk phase, respectively; the electrode area is given by A, n is the number of electrons transferred per molecule, D_O and D_R are the rates of diffusion of the electrode-active species in the solution, and F is the Faraday constant.

In the linear voltage sweep or cyclic voltammetric experiment, the relation of the applied potential versus time is given by

$$E(t) = \begin{cases} E_i - vt & \text{for } 0 \leq t \leq \lambda \\ E_i - 2v\lambda + vt & \text{for } t \geq \lambda \end{cases}$$

where E_i is the initial potential, v is the rate of potential scan, and λ is the time at which the scan is reversed. For a reversible reaction, the peak current is deduced to be

$$i_p = 2.69 \times 10^5\, n^{3/2} A\, D_O^{1/2} C_O^* v^{1/2} \qquad \text{at } 25°C,$$

which is often called the Randles-Sevcik equation with i in μamperes, A in cm^2, n in faradays, D in cm^2/sec, C in millimoles/liter, and v in volts/sec. From the general solution of this boundary value problem,

several features of a reversible charge-transfer reaction are derived as listed below [3a].

a. The peak potential, E_p, and the peak separation, $E_p^c - E_p^a = 59/n$ mV at 25°C are independent of the scan rate v. a and c stand for the anodic and cathodic scans.

b. $i_p / v^{1/2}$ is independent of v.

c. i_p^a / i_p^c is unity and independent of v.

d. The relations between the peak potential, half-wave potential, and the formal electrode potential, $E^{\circ\prime}$, are

$$E_p = E_{1/2} - 28.5/n \text{ mV}$$

$$E_{1/2} = E^{\circ\prime} - \frac{0.059}{n} \log\left(D_O^{1/2} / D_R^{1/2} \right) \qquad \text{at } 25°C$$

B. <u>Quasi-reversible charge transfer</u>

The above derivation and features are for a system comprised of a reversible redox couple. The current or the electrons transferred through the electrode are solely controlled by the diffusion of molecules near the interfacial boundary. In a quasi-reversible charge-transfer reaction, the current is controlled by the charge-transfer kinetics as well. Consequently, absolute rate theory must be considered instead of the Nernst equation. Since the charge transfer rate is potential dependent, the net current is expressed as:

$$i(t)/nFA = C_O(0,t)\, k_s \exp\left(\frac{-\alpha nF}{RT} \left\{ E(t) - E^\circ \right\} \right)$$

$$- C_R(0,t)\, k_s \exp\left(\frac{\beta nF}{RT} \left\{ E(t) - E^\circ \right\} \right)$$

where k_S is the charge-transfer rate constant at the standard potential E° of this redox pair, α is the charge transfer coefficient of the reduction step, and $\beta = 1 - \alpha$. α is a symmetry factor which

determines what fraction of the electrical energy resulting from the displacement of the potential from the equilibrium value affects the rate of electrochemical transformation. α is typically around 0.5 [3b]. The characteristics of a cyclic voltammetric curve derived from the general solution are the following:

a. E_p shifts with scan rate v, and $E_p^c - E_p^a$ may approach 60/n mV at low v but increases as v increases.

b. $i_p / v^{1/2}$ is virtually independent of v.

c. i_p^a / i_p^c equals unity only for $\alpha = 0.5$

d. The cyclic voltammogram approaches that of an irreversible charge transfer as v increases.

In addition to these two cases, other types of charge-transfer mechanisms and kinetics, which have been well discussed by Brown and Large [3], will not be described here.

Apparatus

A. Cyclic voltammetry

A three-electrode cell, which consists of working, auxiliary, and reference electrodes, is used in this study. This kind of controlled-potential voltammetry is preferred because the problem of iR drop across the solution can be largely avoided and the potential of the working electrode can be accurately monitored by a reference electrode. On the contrary, the polarization effect of the reference electrode and iR drop have seriously hampered the prospect of two-electrode cells especially in non-aqueous solutions.

Cyclic voltammetric measurements were obtained with a Princeton Applied Research (PAR) Model 173 potentiostat and a PAR Model 175 universal programmer. Usually, an isolated platinum wire served as the

auxiliary electrode and a Beckman 39270 fiber-junction saturated Calomel electrode (SCE) as the reference electrode, which was separated from the sample solution by a salt bridge. In non-aqueous solutions, the fiber junction of the SCE was easily clogged by the precipitated potassium perchlorate, so a Beckman 40250 sleeve-junction SCE was used instead. A medium porosity sinter frit was occasionally used to separate the solution in the salt bridge from the solution of interest, but in most cases a PAR Vycor tip fitted inside a heat-shrinkable teflon tubing was chosen. Special care was paid to these tips since they cracked very easily on exposure to a different environment, i.e. immersed in an organic solvent but the salt bridge filled with an aqueous solution. It is possible to prevent the tip from cracking by equilibrating the tip for a few hours in a mixture of the two environments prior to the dip in the non-aqueous solution.

The selection of the working electrode depends on what kind of solvent is used and what potential range is under study. In non-aqueous solutions, a Beckman 39273 platinum inlay electrode was chosen, while in aqueous solutions a hanging mercury electrode was used to study the redox reactions in a potential range below the on-set potential for the oxidation of mercury.

In order to prevent the mass transport of electrode-active ions in an electric field and to provide a conducting medium, an inert supporting electrolyte was added to all solutions studied. A simplified schematic diagram of the potentiostat and the three-electrode cell used are shown in Figure 1a .

Figure 1. (a) Simplified schematic diagram of a potentiostat and an electrochemical cell with three-electrode configuration. WE: working electrode; CE: counter electrode; RE: reference electrode

(b) Thin-layer, optically transparent electrode (OTE). The half-cell with the reference electrode is separated from that with working electrode by a salt bridge fitted with a vycor tip.

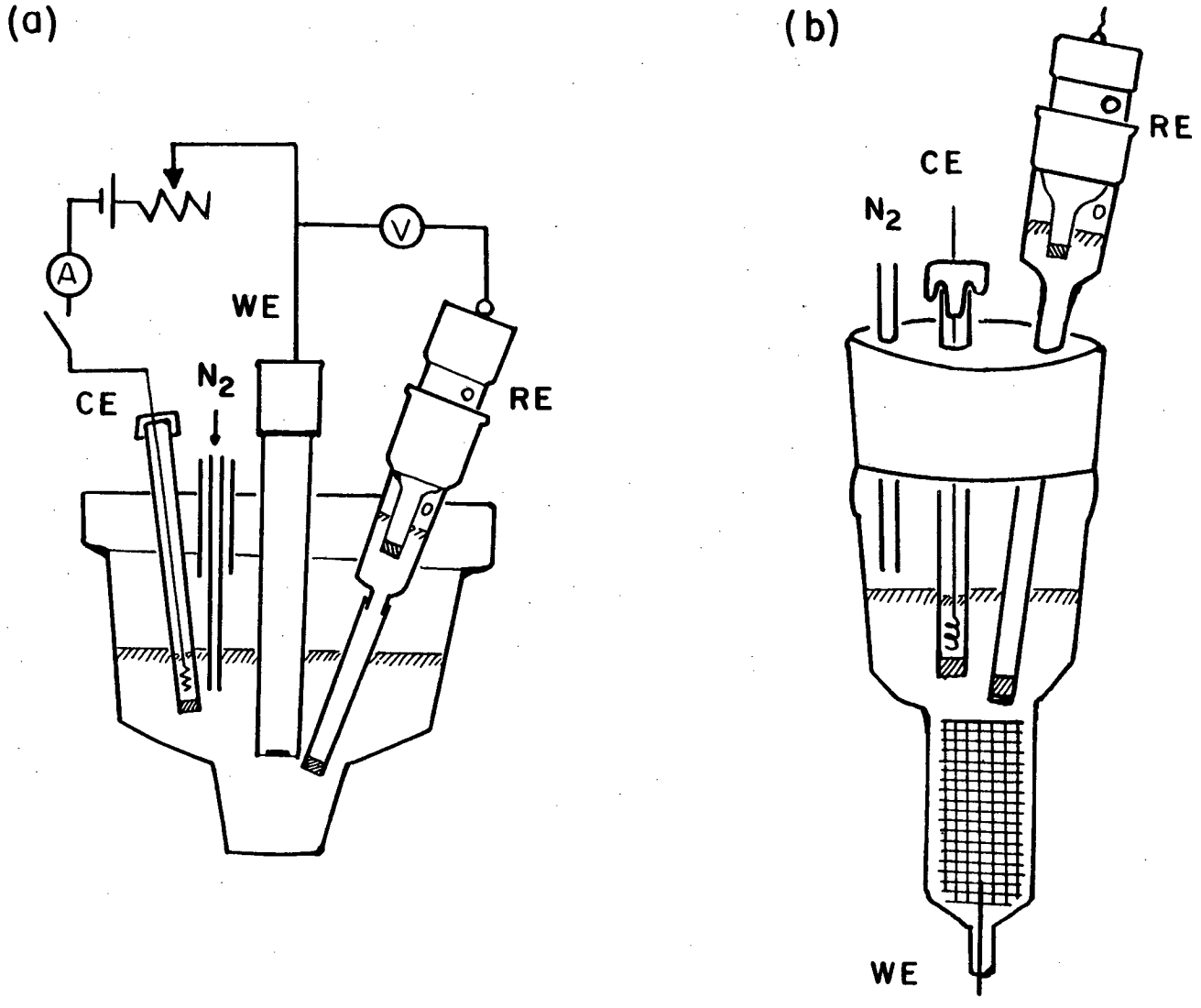

XBL 819-4938

B. Thin-layer, optically transparent electrode

With a potentiostat, the potential in the sample compartment can be varied such that the oxidation state of a compound may be controlled. After a complete electrolysis, the optical characteristics of the oxidized or reduced species can be followed by retrieving a small aliquot of solution and recording its absorption spectrum with a spectrophotometer. However, this requires a lot of manipulation and cautions. If one is dealing with an oxidized sample with a high reduction potential, partial conversion of the sample back to the original oxidation state is unavoidable.

A thin-layer, optically transparent electrode (OTE) is frequently used to alleviate these difficulties and to record the spectral changes in situ. Several have been designed, but the most useful one is shown in Figure 1b. It was made by pyrex glass with a narrow spacing of 0.2 millimeters in the optically flat region. A platinum mesh of 0.18 mm thick and 70 wires per inch was inserted in between to serve as the working electrode. This cell has an optical transmission of about 50%. If a higher light transmission and faster electrolysis is desired or if the medium is an aqueous solution, a gold mesh with 200 wires per inch, 0.0044 inches thick, and 78% transmission from Buckbee-Mears Company (Saint Paul, Minnesota) may be useful.

2. Excited-state Lifetime Measurements

The measurement of the excited-state lifetime of a sensitizer is essential to the understanding of its photochemistry. Knowing this parameter in conjunction with other steady-state experiments allows one to picture the dynamics of the internal de-activation and other external quenching processes. Because excited-state lifetimes range from milliseconds down to a few nanoseconds, experimental methods for obtaining these decay constants vary accordingly. Among the various methods [4], pulse fluorometry was chosen for this study.

In this particular technique, the excitation is a recurrent light pulse of short duration, which approximates a delta-function, and the fluorescence from the excited sample is followed by a photomultiplier. Since the decay of luminescent intensity normally follows a first-order rate law after the extinction of the excitation pulse, data reduction consists simply of making a semi-logarithmic plot of the luminescent intensity versus time. From the reciprocal of the slope, the mean lifetime cna be calculated.

$$I = I * \exp(-t/\tau) \quad \text{or}$$

$$d \ln I/dt = - t/\tau$$

Deconvolution is usually necessary when the excitation flash is not much shorter than the decay time of the excited sample. Many procedures to deconvolute the data have been well examined by J. N. Demas [5]. The particular curve simulation used in the deconvolution is outlined as follows.

$$D(t) = K * \exp(-t/\tau) \int_{x=0}^{x=t} F(x)\exp(x/\tau) \, dx$$

$$D(t) = F(t) = 0 \qquad \text{for } t \leq 0$$

where D(t) and F(t) are the observed sample decay curve and the

observed flash profile, respectively. With a computer or programmable calculator, the experimental curves can be fitted by the following equations.

$$D^{Calc}(t_n) = \tau\{M_n(t_n - \tau) + B_n + \exp(-\Delta t/\tau)[M_n(\tau_n - t_{n-1}) - B_n]\} + D^{Calc}(t_{n-1})\exp(-\Delta t/\tau)$$

$$M_n = [F(t_n) - F(t_{n-1})] / (t_n - t_{n-1})$$

$$B_n = F(t_n) - M_n t_n$$

where $\Delta t = t_n - t_{n-1}$ and $F(t_1) = D(t_1) = 0$

In this fitting, the flash profile is digitized at arbitrarily spaced n points with t_1 set to the beginning of the flash.

Apparatus

Two different instruments were set up for the measurements of excited-state lifetime. One measured the decay in the range of tens of nanoseconds and longer. The other was the dye-laser flash photolysis apparatus (see the next section). The latter measured the excited-state lifetime by monitoring the decay of the absorption of excited species, and it had its useful range of a microsecond and longer.

A TRW 31A nanosecond spectral source system (TRW Instruments, El Segundo, Calif.) was used for those samples with short excited-state lifetimes. Although it is no longer available from the manufacturer, several of its components can be modified and assembled into a new apparatus, which will be discussed later. The block diagram is shown in Figure 2. A N_2 lamp which emitted 140 Watts into a line spectrum extending from 297.8 nm to 399.8 nm was used for all experiments. The particular N_2 lamp chosen had a pulse duration at half-width of 28 ns, which was measured by the same external photomultiplier by light scattering. This duration was longer than that rated by the

Figure 2. Block diagram of TRW Model 31A Nanosecond Spectral Source System used for the measurement of fluorescent decay time.

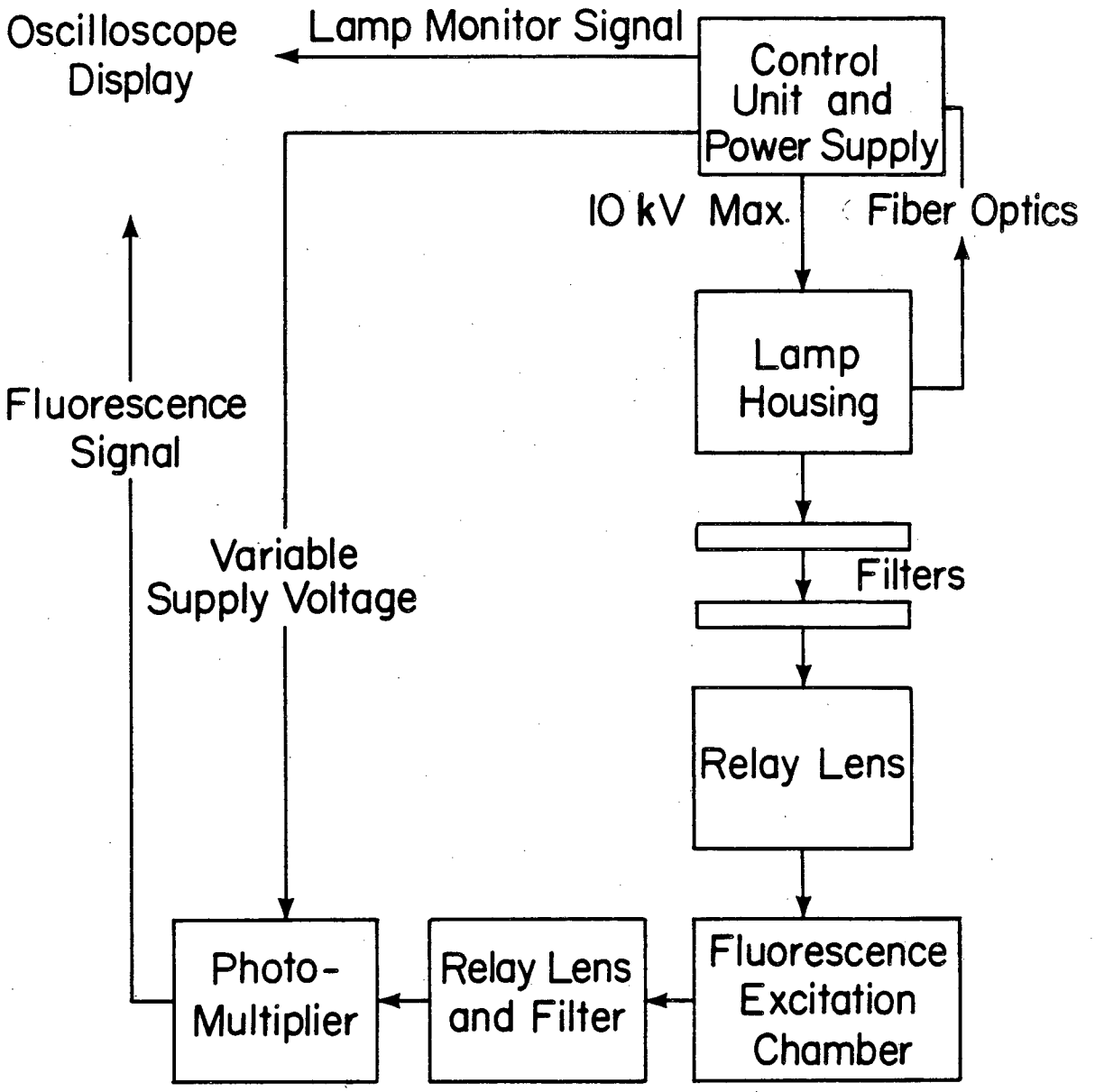
Oscilloscope Display
Lamp Monitor Signal
Control Unit and Power Supply
10 kV Max.
Fiber Optics
Lamp Housing
Fluorescence Signal
Variable Supply Voltage
Filters
Relay Lens
Photo-Multiplier
Relay Lens and Filter
Fluorescence Excitation Chamber

XBL 819-4677

manufacturer, but it was certainly dependent on the convolution of all measuring devices and coaxial cable used. The relay lens assembly contained an adjustable quartz collimating lens system (f/1.5 with aperture 4.8 millimeters). A RCA 931A photomultiplier with a 1.6 nsec risetime powered by a variable voltage source was attached to the oscilloscope via a 50-Ohm coaxial cable for fluorescence signal recording. Appropriate filters were used to separate excitation light from the luminescence.

A storage oscilloscope, Tektronix Type 564B equipped with Type 3T76 sampling dual-trace plug-in (rise time $\leq$ 0.4nsec) and Type 3T77 sampling sweep unit, was used to record the fluorescence decay signal; a Tektronix oscilloscope camera Type C-12 with Polaroid 3000 speed films was used for permanent data recording. The Type 3T77 unit also provided a sweep mode to an external x,y-recorder. With this option, data could be handled more accurately as compared to those obtained from photographic films. Generally, the pulse repetition rate was adjusted to be about 500 or 1000 Hz for the sampling measurements.

Since replacement parts for the TRW Model 31A radiation source are no longer available, a new version which utilizes parts of the old system has been designed. The N_2 lamp can be replaced by a Xenon Model 437A nanopulser (Xenon Corporation, Medford, Mass.) equipped with a Type N-789B high intensity nanolamp, which has a half width of 20 nseconds and emits 5 K watts into a continuum extending from 175 nm into the near infrared. The fluorescent decay signal can be synchronized with the flash pulse by feeding part of the excitation light into the internal photomultiplier inside the TRW 31A via an optical fiber glass.

3. FLASH PHOTOLYSIS

In the study of photo-induced electron transfer reactions, flash photolysis is the most informative technique. It provides an intense, short light flash to populate the desired excited state of a sensitizer, and then it monitors the decay processes subsequent to excitation either by flash spectroscopy involving measurement of a complete absorption spectrum at a pre-set time after the flash, or by flash kinetic spectrophotometry, where changes in transient absorption with time are followed by a photodetector at a fixed wavelength.

Upon excitation of a sensitizer, the time scale of the decay processes ranges from picoseconds (for the vibrational relaxation in condensed media) to milliseconds (for triplet decay). In order to compete with these decay processes and retain the absorbed light energy in the form of chemical energy, quenchers are usually added into the solution as electron donors or as electron acceptors together with some accessory components, such as catalysts and a charged interface. With enough quenchers, electron transfer reactions may dominate and the highly concentrated intermediates involved can be easily followed. By analyzing the decay transients as functions of time and other experimental parameters, one can obtain kinetic and mechanistic data.

Since the first appearance of the flash photolysis system designed by Norrish and Porter in 1948, the instrumentation and techniques used have been progressively improved. Especially, the development of pulsed lasers pushes the time resolution of flash photolysis down to nanosecond range and even further to a few picoseconds by using mode-locked lasers. These submicrosecond excitation light sources allow direct studies of fluorescence decays, quenching events, energy

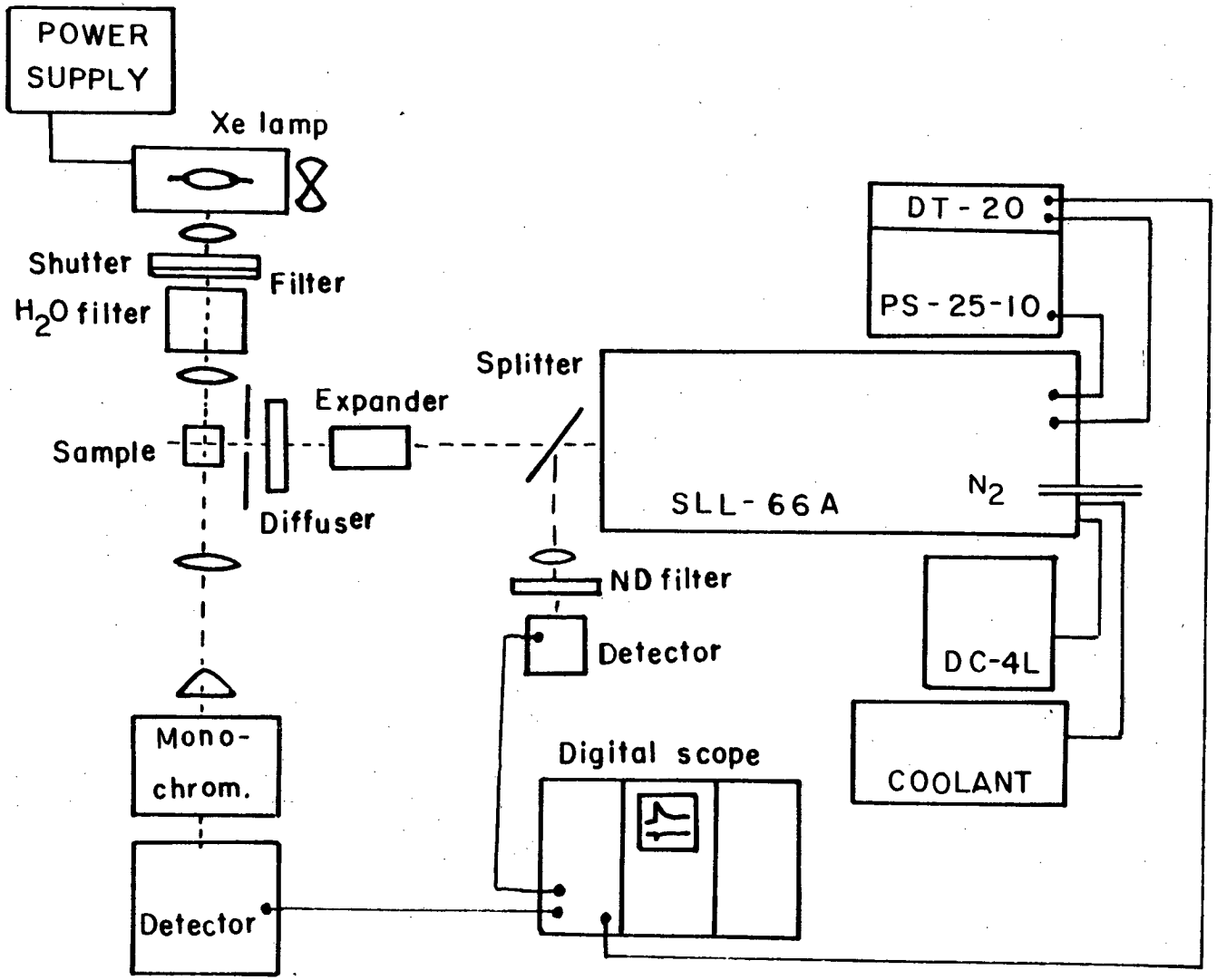
POWER SUPPLY
Xe lamp
Shutter
Filter
H_2O filter
Sample
Expander
Diffuser
Splitter
ND filter
Detector
Mono-chrom.
Detector
Digital scope
DT-20
PS-25-10
SLL-66A
N_2
DC-4L
COOLANT

XBL 819-4936

(A) excitation source, (B) monitoring source and optics, and (C) detector.

(A) The excitation source consists of

flashlamp-pumped dye laser (Candela SLL-66A),
power supply (PS-25-10),
trigger generator and delay (DT-20), and
dye circulation system (DC-4L).

All these parts are from Candela Corp., Natick, Mass. A modified quadraxial lamp dye laser with the dye cell separated from the water jacket by a concentric evacuated annulus (of borosilicate glass) was chosen (Figure 4). It has been shown that the addition of an insulating jacket between the dye solution and the flashlamp cooling water in a coaxial dye laser provides an increase in beam quality and stability that is as good or better than that obtained by precision temperature control of the cooling water in a triaxial system [6]. While in the triaxial configuration the temperature of cooling water has to be held within ±0.05°C of the optimum value (usually, several tenths of a celsius cooler than the dye cell), the temperature difference can be as great as 3°C in the quadraxial configuration. A pair of diffusers, which direct dye solution in a smooth axially symmetric manner into the cell and thus reduce the effects of pressure fluctuations, pressure gradients, and thermal gradients, are used as the end caps in conjunction with two broadband dye cell windows (with anti-reflection coating on one side). One broadband Max Reflector (Candela BBMX) and one broadband output coupler with 40% reflection (Candela BBOC-40) are used for the resonator. In cases where monochromatic laser beam is required, a prism tuner with a 60° adaptor should

Figure 4. Modified quadraxial flashlamp used in Candela 66A dye laser.

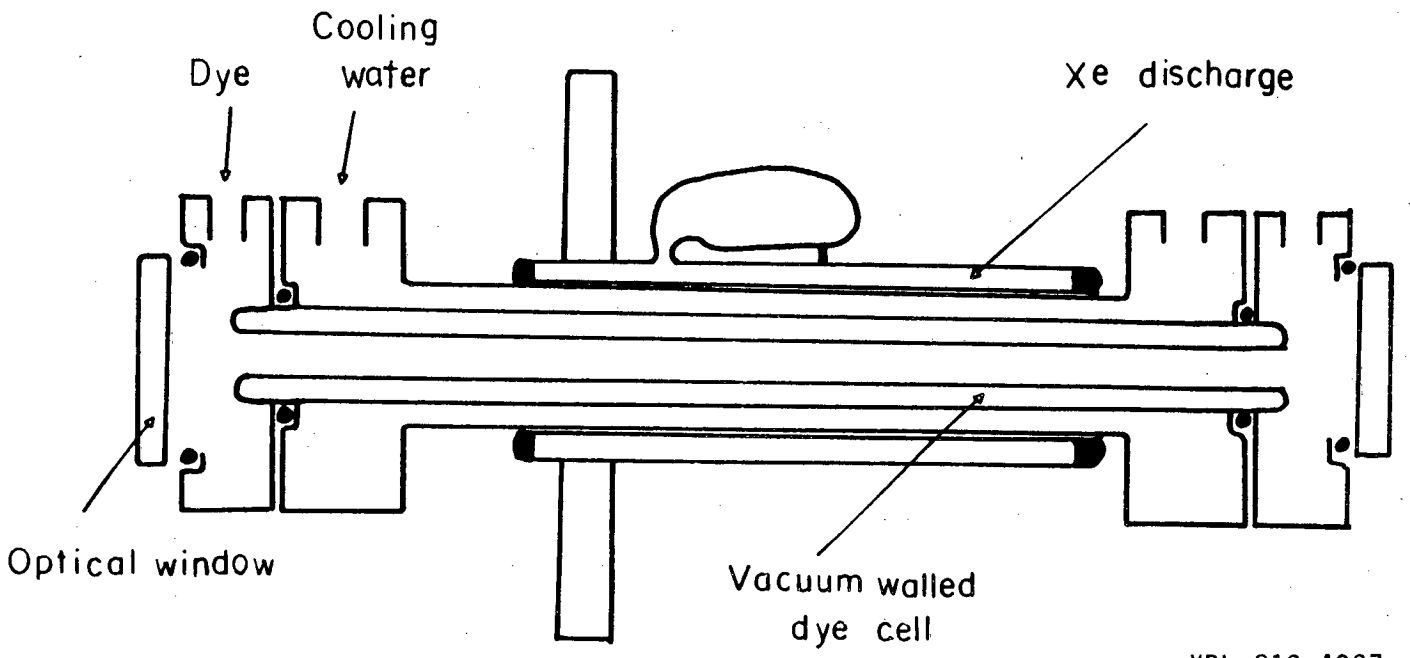
Cooling
water
Dye
Xe discharge
Optical window
Vacuum walled
dye cell

XBL 819-4937

be substituted for the rear reflector.

This SLL-66A laser is driven by a low inductance, spark-gap switched electric driver. Although this type of driver provides higher power, it introduces more noise. To decrease this interference, a second home made shielding case was constructed. With this shielding case, the noise transmitted through space could be largely eliminated, and the fear of saturation of some amplifiers in the detecting system is thus relieved. However, even without this shielding case, the noise lasts only 2 microseconds.

(B) Monitoring source and optics

A 75 watt xenon lamp (US K-1 kinectic arc lamp, Xenon Co.) was used as the monitoring light source and was dc powered by two 12-volt batteries (US-Model G). This small lamp provides satisfactory light intensity between 400 and 850 nm as long as the solution under study has low absorbance ($A \leq 0.2$). The stability of intensity (in terms of the light falling on the entrance slit of monochromator) is mostly limited by arc wandering and external mechanical vibrations (caused by motors and mechanical pumps nearby). In order to examine the spectral region where the sample has high absorbance, a power supply (Oriel) used for 1000 watt xenon lamp was modified such that a capacitor bank can be inserted to smooth out the line cycles. Also, a 150 watt xenon lamp was occasionally used.

On top of the 4-foot precision, high stability optical bench (Oriel) were mounted a few focussing lenses, sample holder, xenon lamp housing, electronic controlled shutter, filter holders, beam splitter, monochromator (Oriel 7240 grating monochromator with a 7271 gratings, 6.4 nm/mm), and detector. If temperature regulation is necessary,

the simple sample holder should be replaced by a thermostated copper block with a sample compartment and four windows. It is important to mount all the above components on a optical bench so that after optics adjustment they can be displaced together as wish. A few diffusing glass plates to homogenize the laser beam were also prepared by grinding sand powders between two glass plates. Care should be taken concerning the surface roughness. Too rough a surface will cause severe beam scattering instead of homogenization.

(C) Detector

Our first detector is almost the same as that designed by J. A. Van Best and P. Mathis [7], and its circuit is shown in Figure 5. This ac detector has a convenient linear time-response from 0.5 μs up to 1 ms and a linear voltage output at least up to 400 mV. It has a 22-volt battery to bias the photodiode (United Detector Technology, PIN-8LC Schottky barrier photodiode) and a pair of rechargeable NiCd batteries for powering transistors and operational amplifier. By virtue of these internally stored power sources, the noise level in the output is only 5 milli-volts (mostly high frequency noise generated by the operational amplifier).

UV-enhanced PIN-8LC is a low capacity device and has a good spectral response from 350 to 1000 nm with its specified linear response from 10^{-12} to 10^{-3} watts. Typically with the monochromator set at 1mm (λ= 600 nm), the photocurrent generated by the light from a 75 watt xenon lamp was measured to be 6 micro-amperes (60 milli-volt across a 10 K-ohm resistor) [8].

In most experiments, changes in absorbance were in the range of 10^{-2} to 10^{-4}. With the assumption that photocurrent is

Figure 5. Schematic diagram of the fast transient detector. The sensor is a PIN-8LC photodiode (United Detector Technology)

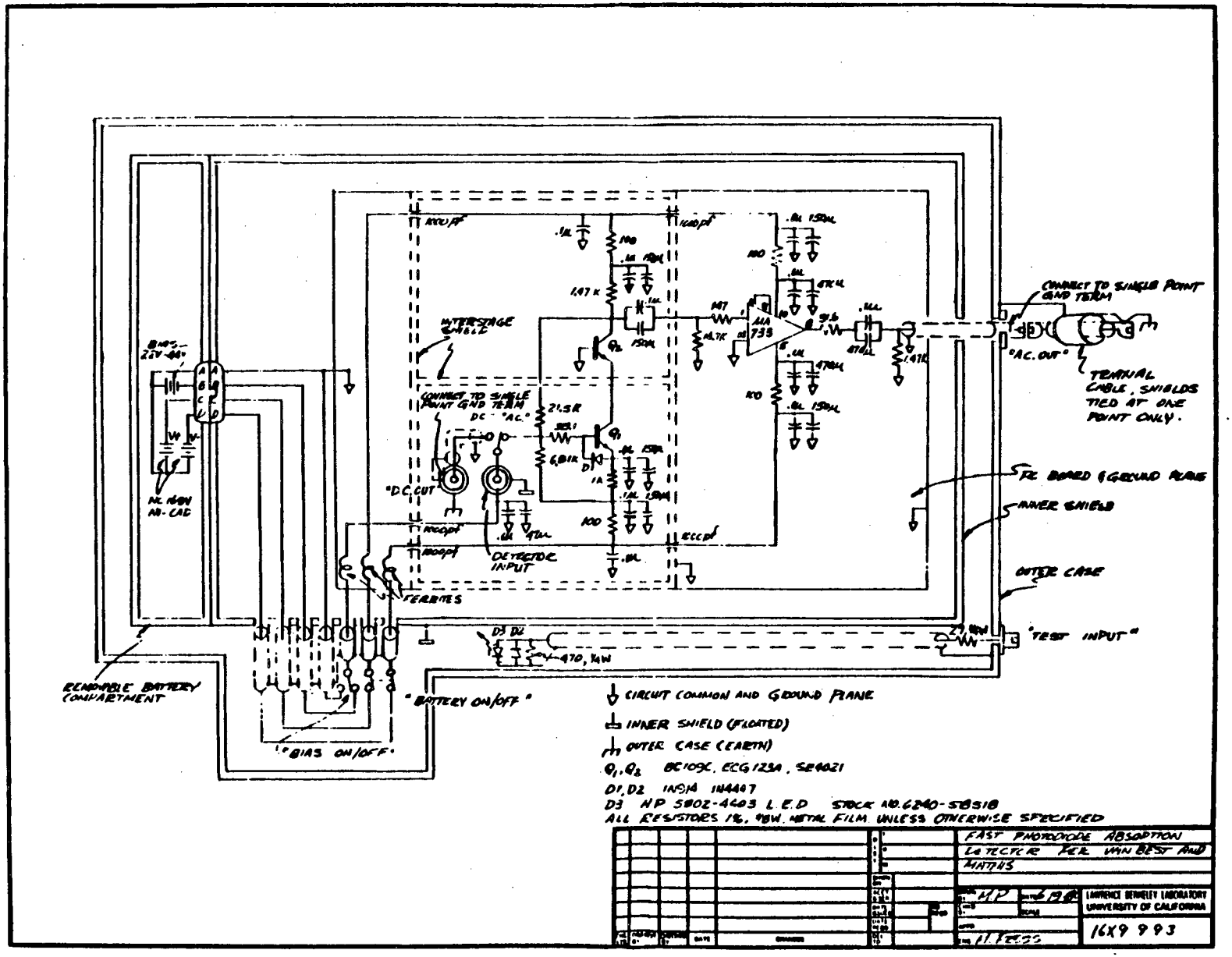
CONNECT TO SINGLE POINT GND TERM
"A.C. OUT"
TRIAXIAL CABLE, SHIELDS TIED AT ONE POINT ONLY.
PC BOARD & GROUND PLANE
INNER SHIELD
OUTER CASE
"TEST INPUT"
INTERSTAGE SHIELD
CONNECT TO SINGLE POINT GND TERM
DC - "AC"
"D.C. OUT"
DETECTOR INPUT
FERRITES
BIAS 2.2V-4.4V
NC 1.4V NI-CAD
REMOVABLE BATTERY COMPARTMENT
"BATTERY ON/OFF"
"BIAS ON/OFF"
CIRCUIT COMMON AND GROUND PLANE
INNER SHIELD (FLOATED)
OUTER CASE (EARTH)
Q1, Q2 BC109C, ECG123A, SE4021
D1, D2 1N914 1N4447
D3 HP 5082-4403 L.E.D STOCK NO. 6240-5851B
ALL RESISTORS 1%, 1/8W, METAL FILM UNLESS OTHERWISE SPECIFIED
FAST PHOTODIODE ABSORPTION DETECTOR FOR VAN BEST AND MATTUS
LAWRENCE BERKELEY LABORATORY
UNIVERSITY OF CALIFORNIA
16X9 993

proportional to light intensity and with a typical I = 10 μA, ΔI is about 10^{-8}A. Such a small variation in photocurrent is brought up to a measurable voltage by the ac amplifier in our detector, which has a total substitution impedance of 710 K-ohms in the present condition.

An Explorer IIIA digital oscilloscope with a 204A plug-in unit monitors the output (AC-OUT) from the detector via a triaxial 50-ohm cable and a 10K-ohm resistor. With this 204A plug-in, Explorer IIIA has two channel capability, 8-bit resolution, and a 20M Hz sampling rate. Its 4096 words can be halved or quartered so that a maximum of four scans can be stored in the memory. These stored data are then recorded on an X-Y recorder (Hewlett-Packard 7004B). One of the most useful features of this digital scope is its cursor triggering mode, which allows viewing of the signal prior to the triggering.

With this set of detecting and recording components, many photo-induced electron transfer reactions in homogeneous solutions were carried out. However, when heterogeneous systems were studied, it was necessory to have a detector capable of following the transients up to a fraction of a second. So, a second detector was home-built. It consists of two photo-diodes; one monitors the sample beam, the other monitors the light intensity of the measuring light source (Figure 6). With such a configuration, one does not have to worry about the line cycle and the intensity fluctuation of the light source. Figures 7(a-d) show the circuit diagrams of this detector. In contrast to the first detector, this one has a dc amplifier and is powered by an external source. As a dc detector, it measures the total light intensity and the transient response through the same dc amplifier; the dc level is offset by a signal from the reference photodiode when measuring the

Figure 6. Schematic diagram of flashlamp-pumped dye laser with a fast double-beam spectrophotometer.

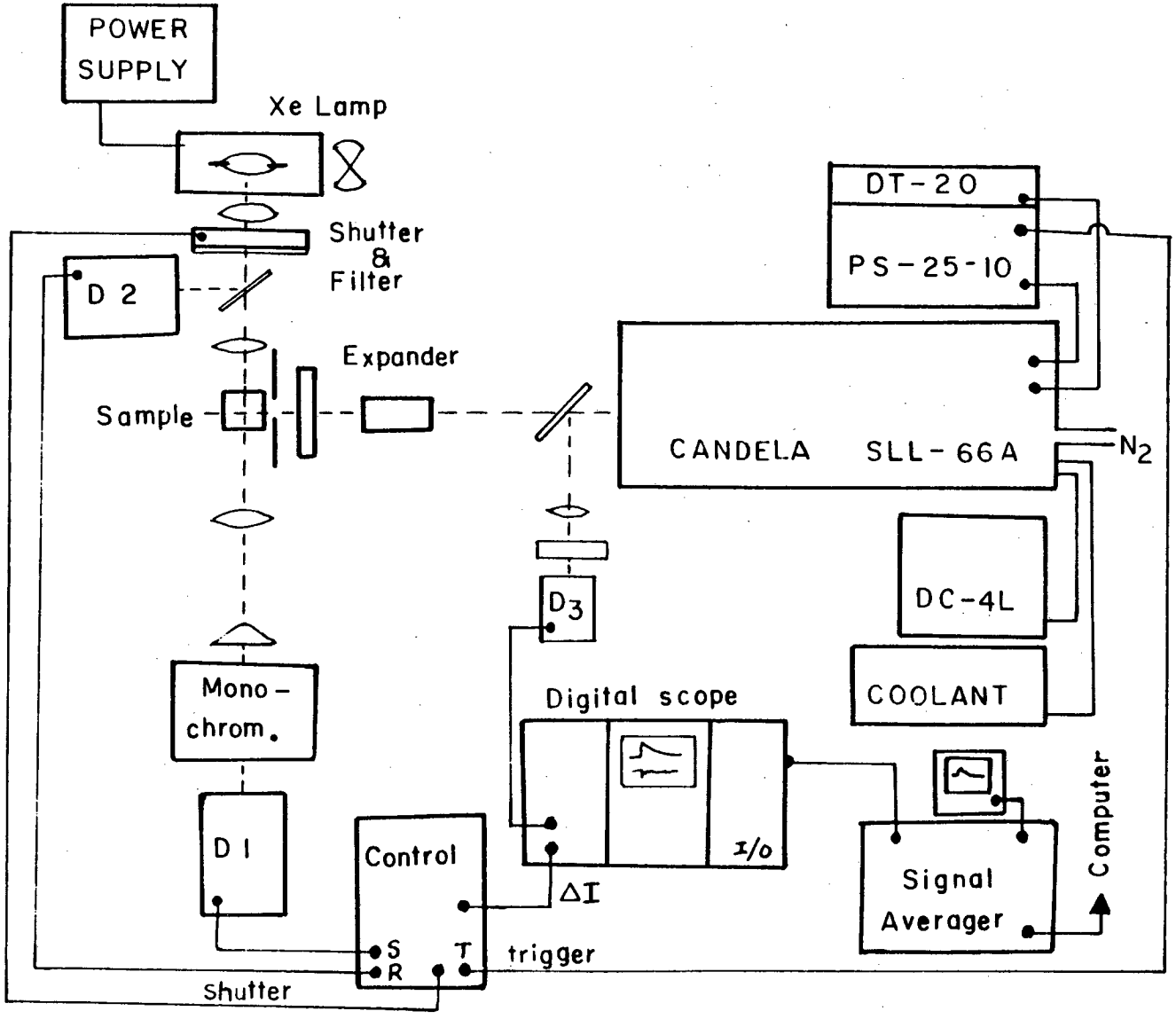
POWER SUPPLY
Xe Lamp
Shutter & Filter
D 2
Expander
Sample
Mono-chrom.
D 1
Control
S
R
T
trigger
Shutter
D3
ΔI
Digital scope
I/o
DT-20
PS-25-10
CANDELA SLL-66A
N2
DC-4L
COOLANT
Signal Averager
Computer

XBL 819-4939

Figures 7. Circuit diagrams of the transient detector with a wide bandwidth from 1 MHz down to a few Hz. Two photodiodes are used. One senses the sample beam, the other monitors the reference beam from a beam splitter.

(a) Preamp of the fast photodetector.

(b) Signal processing unit.

(c) Shutter and laser control logic unit.

(d) Modifications of associated commercial equipments.

Left: control on Ealing shutter supply

Right: interlock on Candela SLL dye laser

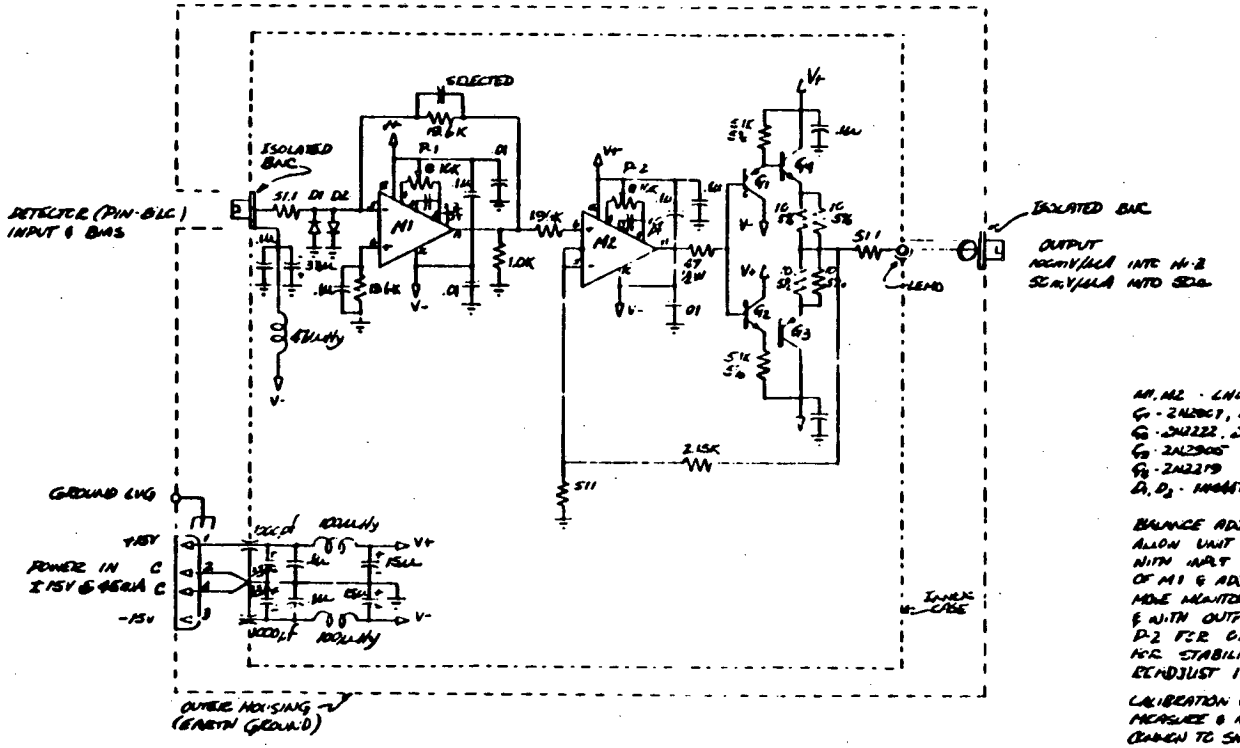

M1, M2 - LH0042CG
Q1 - 2N2907, 2N3906
Q2 - 2N2222, 2N3904
Q3 - 2N2905
Q4 - 2N2219
D1, D2 - 1N4447

BALANCE ADJUSTMENT:
ALLOW UNIT TO WARM UP FOR 2K MIN WITH INPUT OPEN MONITOR PIN 11 OF M1 & ADJUST P1 FOR CONV = .1mV. MOVE MONITOR TO OUTPUT CONNECTOR & WITH OUTPUT OPEN ADJUST P2 FOR CONV = 5mV. CHECK FOR STABILITY AFTER 15 MIN & READJUST IF NECESSARY

CALIBRATION CHECK:
MEASURE & NOTE VOLTAGE FROM CENTER TO SHIELD OF INPUT BNC CONNECTOR (≈ 15V). CONNECT 1MEG 1% RESISTOR ACROSS INPUT CONNECTOR OUTPUT SHOULD READ .1 (+0.05, -5%)

FLOW ANALYSIS SYSTEM
FAST PHOTODETECTOR PREAMP
WITH LINE DRIVER

M.F. 9 9 81
M. PRESS
LAWRENCE BERKELEY LABORATORY
UNIVERSITY OF CALIFORNIA
26X1163 S1

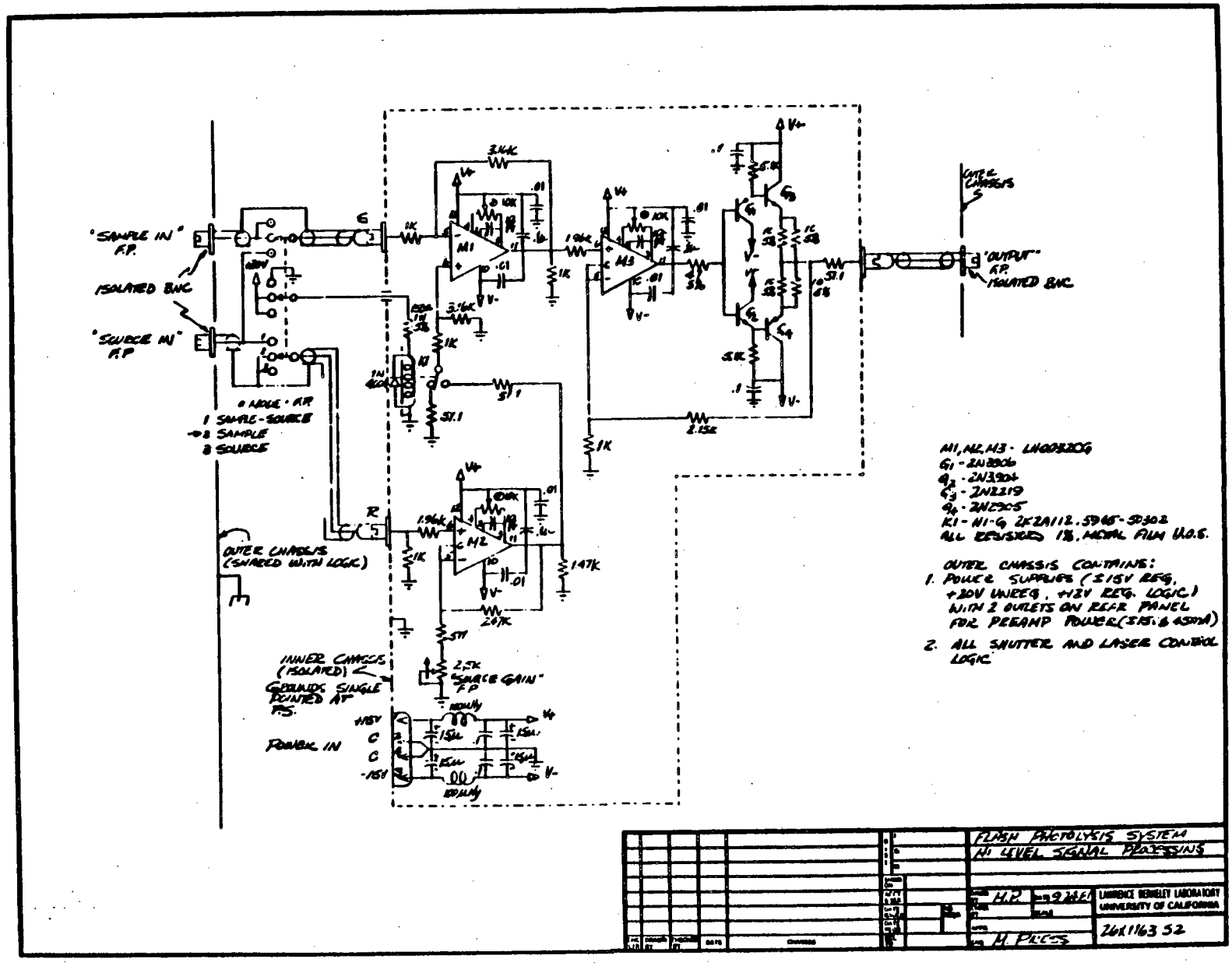
"SAMPLE IN" F.P.
ISOLATED BNC
"SOURCE IN" F.P.
0 HOLE - F.P.
1 SAMPLE-SOURCE
2 SAMPLE
3 SOURCE
OUTER CHASSIS (SHARED WITH LOGIC)
INNER CHASSIS (ISOLATED)
GROUNDS SINGLE POINTED AT P.S.
POWER IN
"SOURCE GAIN" F.P.
OUTER CHASSIS
"OUTPUT" F.P.
ISOLATED BNC
M1, M2, M3 - LH0032CG
G1 - 2N3906
Q2 - 2N3904
Q3 - 2N2219
Q4 - 2N2905
K1 - HI-G 2K2A112.5945-50302
ALL RESISTORS 1%, METAL FILM U.O.S.
OUTER CHASSIS CONTAINS:
1. POWER SUPPLIES (±15V REG, +20V UNREG, +12V REG. LOGIC) WITH 2 OUTLETS ON REAR PANEL FOR PREAMP POWER (±15, 6 450mA)
2. ALL SHUTTER AND LASER CONTROL LOGIC
FLASH PHOTOLYSIS SYSTEM
HI LEVEL SIGNAL PROCESSING
LAWRENCE BERKELEY LABORATORY
UNIVERSITY OF CALIFORNIA
M. PICCS
26X1163 52

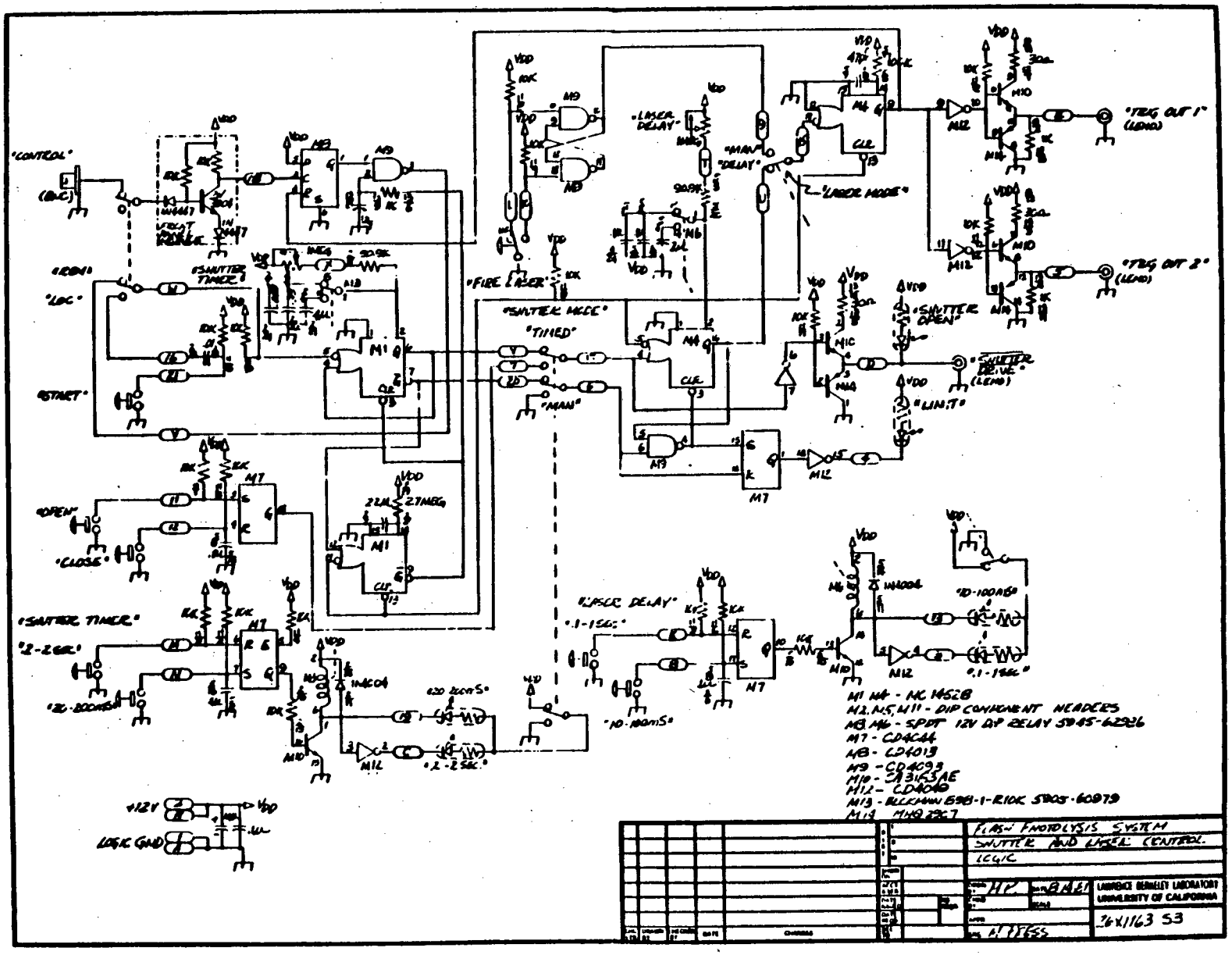
"CONTROL"
"LOC"
"START"
"OPEN"
"CLOSE"
"SHUTTER TIMER"
"2-2SEC"
"SHUTTER MODE"
"TIMED"
"MAN"
"FIRE LASER"
"LASER DELAY"
"MAN"
"DELAY"
"LASER MODE"
"TRG OUT 1"
(LEMO)
"TRG OUT 2"
(LEMO)
"SHUTTER OPEN"
"SHUTTER DRIVE"
(LEMO)
"LIMIT"
"LASER DELAY"
"10-100nS"
"0.1-1SEC"
+12V
LOGIC GND
M1 M4 - MC 14528
M2, M5, M11 - DIP COMPONENT HEADERS
M3, M6 - SPDT 12V DIP RELAY 5945-62936
M7 - CD4044
M8 - CD4013
M9 - CD4093
M10 - 2N3053AE
M12 - CD4049
M13 - BECKMAN 598-1-R10K 5905-60979
M14 - MK9 2367
FLASH PHOTOLYSIS SYSTEM
SHUTTER AND LASER CONTROL
LOGIC
LAWRENCE BERKELEY LABORATORY
UNIVERSITY OF CALIFORNIA
76X1163 53

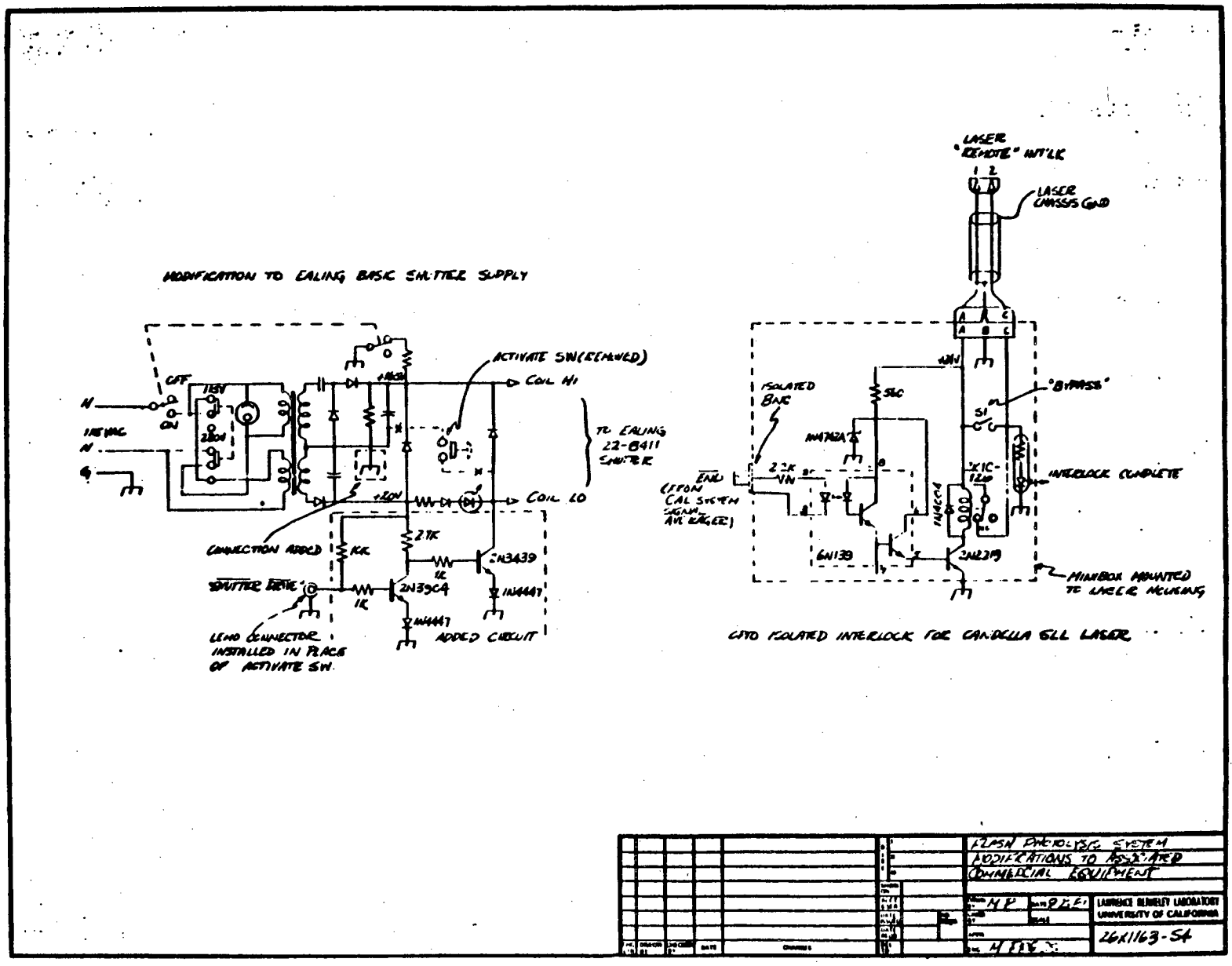
MODIFICATION TO EALING BASIC SHUTTER SUPPLY
ACTIVATE SW (REMOVED)
COIL HI
COIL LO
TO EALING 22-8411 SHUTTER
CONNECTION ADDED
SHUTTER RETN
LEMO CONNECTOR INSTALLED IN PLACE OF ACTIVATE SW.
ADDED CIRCUIT
2N3439
2N3904
1N4447
LASER "REMOTE" INT'LK
LASER CHASSIS GND
ISOLATED BNC
"BYPASS"
INTERLOCK COMPLETE
MINIBOX MOUNTED TO LASER HOUSING
OPTO ISOLATED INTERLOCK FOR CANDELA SLL LASER
FLASH PHOTOLYSIS SYSTEM
MODIFICATIONS TO ASSOCIATED COMMERCIAL EQUIPMENT
LAWRENCE BERKELEY LABORATORY
UNIVERSITY OF CALIFORNIA
26X1163-S4

transient response. Because the detector has a very wide bandwidth, three operational amplifiers, and an external power supply, the noise level is unavoidably several times higher than that of the first detector. In order to make use of this detector, a signal averager was also constructed. It adds signals and transmits the accumulated data to the computer located at the Melvin Calvin Laboratory. Through the averaging, noise and other interferences such as line cycle and arc wandering can be largely eliminated. Furthermore, with this signal averager the data can now be stored and displayed on a graphical terminal to facilitate curve analysis.

Operational procedures

Although some instructions are given in the manuals provided by manufacturers, they do not contain enough details. The following should provide more useful guides.

(a) Laser alignment

The laser head is first assembled with two dye-cell windows and fittings for tubings of the dye solution and coolant. Then, this head is carefully installed inside the laser housing. After attaching the tubings, circulate dye solution and cooling water at proper flow rate to check for any possible leakage.

The Model A version of the SLL laser is based on a three-foot cavity. To have low beam divergence, it is necessary to use its maximum spacing. However, if a higher power output and an easier alignment are desired, the length of laser cavity may be shortened to between 2 and 3 feet. In our experiment, because space is limited and the optical bench for detecting system, the sample holder and monitoring system were placed very close to the laser head. This eased

the stringent requirements of beam quality.

For the first-time alignment, a 0.5 mW Spectra-Physics Model 155 He-Ne laser should be used. Support this laser on two jacks at a distance of about 2 feet from the SLL laser housing, and align the He-Ne laser beam through the output hole, front coupler (40% R), front dye-cell window, dye cell with the two plexi-glass end cups provided by the manufacturer and rear window, and finally allow the beam to reach the center of the rear coupler. A piece of cardboard with a small hole (with a diameter slightly smaller than that of the He-Ne laser beam so that only the center most concentrated beam passes through) is then taped on the inner side of the output hole. The most important alignment now is to turn the rear coupler carefully so that the reflected beam from the rear coupler falls back on the same small hole drilled on the cardboard. After this adjustment, the beam will travel through the dye-cell twice in the same line. Make sure that the dye solution is flowing in the dye cell when aligning these optics. Next, bring the reflected beam from the back side of the front coupler through the center of the dye cell to the same spot that the laser beam first hits on the rear coupler. These two steps will assure that most of the light travels within the cavity through the same line and the lasing condition can be quickly established. Efforts to bring the other reflected beams from cell windows back in line are not critical since they represent only a minor loss.

After these adjustments, test the laser to see if the alignment is properly done. If the laser cannot lase at this point, another more careful alignment should be performed. If it lases, use a blank developed high-speed Polaroid film to check the beam quality. A well-

aligned laser beam should be able to burn a hole the size of the dye cell tubing. To facilitate the final fine adjustments, some of the safety interlocks may be disarmed, providing proper precautions and safety rules are observed. After masking the laser head, one may then slowly turn first the rear coupler to optimize the beam quality and then the front coupler until a round hole is burned evenly on the Polaroid film. One caution should be mentioned here. If an organic solvent is used and the lamp blows up, high voltage across electrodes might trigger a fire.

This laser uses an air-filled spark gap to hold the high voltage. Without pressurizing the spark gap, it can hold up to 15 kV. In order to increase the light intensity from xenon plasma and have a higher laser output, a higher voltage up to 25 kV may be supplied. This is made possible by pressurizing the spark gap 1 atm more for each 1 kV increment above 15 kV. Use only a minimal possible pressure so that the jitters of triggering may be minimized. Fill the spark-gap only with dry nitrogen to retard the aging of electrodes. Generally, 18 kV is enough for lasing with a rhodamine dye solution, and 21 kV for a coumarin dye. Voltage up to 25 kV may be used, but the lamp may age faster (the lamp has rated lifetime of about 100 k shots) [9]. Never trigger the laser when the voltage is below 12 kV because doing so will damage the circuit components.

Before firing the laser, circulate both dye solution and coolant for about 15 minutes to avoid any air bubbles trapped in the tubing, and check leaks. Also, flush the laser housing with nitrogen gas to avoid any possible fire. At the optimal concentration of dye, the laser burns a round hole evenly. If the concentration is not high

enough, the hole is burned mostly in the center. On the other hand, if the concentration is too high, a doughnut shaped spot will be seen because the light from the coaxial xenon lamp is mostly absorbed in the outer layer of the dye solution. The smaller the diameter of the dye cell, the higher the concentration of dye solution that should be used.

Since all dyes bleach gradually, the dye solution has to be replaced after a certain number of shots. For example, the coumarin 450 provides 25 to 40 Kjoule/liter. If 50 joules per shot is assumed, 2 liters of coumarin 450 dye solution lasts roughly 1000 to 1600 shots. Other dye solutions may degrade more slowly. In any event, it is better to replace the dye solution completely instead of adding a fresh one to a aged one, because the degraded dye may compete with the new dye to absorb light from xenon plasma or otherwise interfere with the lasing.

For this laser, two types of lamps are compatible.

CL-50 1 cm I.D. by 7 cm arc length. A quadrax dye cell can be fitted to this lamp and can be interchanged between lamps.

CL-66 6 mm I.D. by 10 cm arc length. The quadrax cannot be fitted to this lamp.

The manufacturer does not recommand the triax configuration though. With the quadrax adaptor used, the CL-50 lamp has only 3 mm I.D..

(b) Optics alignment

The best way is to insert one lens after another. At each insertion, make sure that the center spot of the light from the measuring lamp is still at the entrance slit of the monochromator. While the beam should be finally focussed on the entrance slit, its first focussed point should be at the middle of sample cell. One trick to

simplify the alignment is to fill a $Ru(bpy)_3^{2+}$ solution in the sample cell since this solution fluoresces strongly in the orange. With this solution, the light path can be easily visualized.

Our 75 watt xenon lamp did not come with the specifications of rated optimal current and voltage, so the voltage across the lamp was first measured and the current necessary to provide 75 watt energy consumption was computed to be 5.8 amperes. This lamp is powered by two auto batteries, which have to be charged after each use and checked periodically for fluid levels. Cooling for the lamp is not necessary, but an exhaust system should be provided to avoid ozone accumulation. Be careful that the cooling fan does not introduce more mechanical vibrations and noise. One thing, which most people are not aware of, is that it takes about 10 to 15 minutes for the xenon lamp to stabilize itself.

In case fluorescence of the excited sample causes problems, a monitoring lamp with higher intensity should be substituted. This allows us to use a smaller slit width, and thus the amount of fluorescence which reaches the detector decreases.

The accuracy of the monochromator is checked by a set of interference filters. At present, setting λ = 495.6 nm on the monochromator allows the light band peaked at λ = 500 nm to pass through. This indicates that there is a -4.4 nm shift on the actual readings. Occasionally, the screw controlling the slit may come loose and it has to be checked and then re-tightened.

Because all of the above optics and lamp are mounted on the same optical bench, they are displaced together. This allows us to position the laser beam through the center of the sample cuvette by simply

moving the optical bench. Again, a $Ru(bpy)_3^{2+}$ solution is used for alignment of these two crossed beams. In most experiments, the laser beam was first expanded to a larger area by a beam expander and then confined to a fixed width by a slit so that the 1x1 cm cuvette cell could be used and the alignment could be simplified.

(c) Detector

While the DC-OUT on the detector is used to measure the total intensity after passing through the sample, the AC-OUT is for measurement of the intensity variation after photolysis. With a 10 K ohm resistor and a digital voltmeter, the linearity of DC measurement is assured (at least up to 200 mV across the resistor at λ = 600 nm). The total substitution impedance of this detector was found to be 720 $\pm$10 K-ohms as measured by deleting the photodiode and feeding some known current into the amplifier by a power supply and a 10 M-ohm resistor (Figure 8a). Another method to measure the total substitution impedance is shown in Figure 8b. In addition to the 75 watt xenon lamp, a 5 mW He-Ne laser (Jodon Engineering Associates) was also used. This method is slightly less reliable because it takes a finite time to open up the shutters. Nevertheless, the value was found to be 690 $\pm$ 30 K-ohms, which is in good agreement with the number obtained by the first method.

The biasing of the operational amplifier in the detector should be checked occasionally by illuminating the detector over a period longer than its recovery time. If the two ac outputs corresponding to the starting and the ending of the light pulse have more or less same heights, one can be sure that the dc level of the output is set at the middle of the linear range.

Figure 8. (a) Circuit diagram for the measurement of total substitution impedance of fast transient detector in figure 5 with the photo-diode removed.

(b) Schematic diagram for the measurement of total substitution impedance with the photo-diode installed. Two probing light sources may be open or close separately.

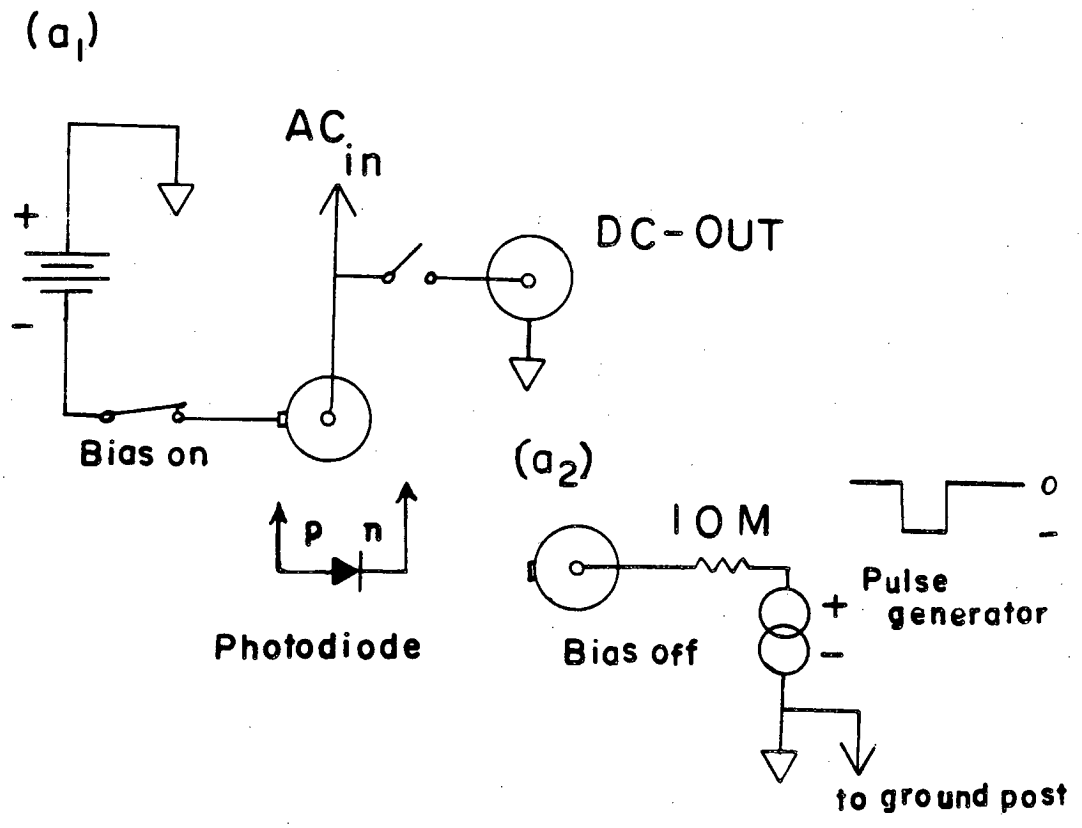
(a1)
AC in
DC-OUT
+
-
Bias on
p n
Photodiode
(a2)
10 M
Bias off
+
-
Pulse generator
0
-
to ground post

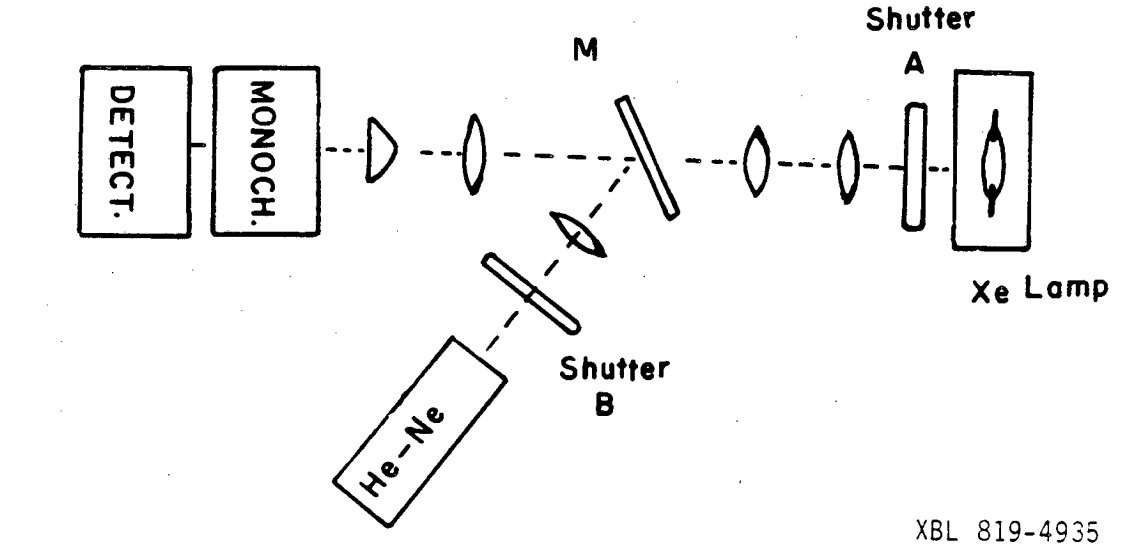
(b)
DETECT.
MONOCH.
M
Shutter A
Xe Lamp
Shutter B
He-Ne

XBL 819-4935

Triggering of the laser is provided by a home-built unit, which serves both as the main amplifier and the power supply for the aforementioned second detector (see apparatus section) and controls the duration of electronic shutter and the delay of laser triggering. Normally, the delay is set to at least half a second after the opening of the electronic controlled shutter because it takes that long to restore the first detector to within its linear range. It is not necessary to have such a long delay for the second detector.

Triggering of the digital scope can be best achieved by a separate photodiode which senses the lasing beam via a beam splitter. In most of our runs, however, the pulse generated in the laser trigger system is used.

Some notes for the flash photolysis study

(a) As long as the laser beam stays within the sample cuvette, the area where it hits the sample is not important. In the optimal condition, however, the beam should be expanded and homogenized to a circle with diameter b corresponding to the area of the sample cell illuminated.

(b) A spacer inside the cuvette sometimes helps to improve the signals. For example, if, before the flash, A = 0 at λ, the wavelength where the detector monitors, it makes no difference whether the spacer is installed or not. But, if A is not zero at λ, setting the thickness of a spacer equal to the width of laser beam improves the signals. However, if the quantum yield of the desired product is low and absorbance at λ is not zero, setting the steady-state absorbance to be around 0.4 would optimize the signals.

(c) A signal averager is still useful for the measurement of second-

order rate constants, because fluctuations in laser intensity within 30% will cause only a minor error in the derived constant.

References and notes

1. R. S. Nicholson and I. Shain, Anal. Chem., 36, 706 (1964).

2. R. S. Nicholson, Anal. Chem., 37, 1351 (1965).

3a. E. R. Brown and R. F. Large, "Techniques of Chemistry", A. Weissberger, ed., Vol. 1, Part IIA, Wiley-Interscience, New York, 1971.

3b. J. O'm Bockris and A. K. N. Reddy in "Modern Electrochemistry", Vol. II, p. 917, Plenum Press, New York, 1970.

4. J. D. Birks, "Photophysics of Aromatic Molecules", Wiley-Interscience, New York, 1970.

5. (a) J. N. Demas, G. A. Crosby, Anal. Chem., 42, 1010 (1970).
(b) J. N. Demas, J. Chem. Ed., 53, 657 (1976).
(c) J. N. Demas and C. M. Flynn, Jr., Anal. Chem., 48, 353 (1976).

6. T. B. Lucatorto, T. J. McIlrath, S. Mayo, and H. W. Furumoto, Appl. Optics, 19, 3178 (1980).

7. J. A. Van Best and P. Mathis, Photochem. and Photobiol., 31, 89 (1980).

8. As a useful reference, 1 A photocurrent would amount roughly to 2 watts at λ = 600 nm if this photodiode had 100% efficiency. Actually, it has only about 50% efficiency at λ = 600 nm.

9. This rated lifetime was given by the manufacturer.

Mr. Horace W. Furumoto (with Candela Corporation, Natick, Mass.) has been very helpful during the construction of this apparatus.

CHAPTER III

PHOTO-INDUCED ELECTRON TRANSFER REACTIONS IN HOMOGENEOUS SOLUTIONS

Some of the experiments in this chapter were carried out in collaboration with Professor Tetsuya Sakai.

Solar radiation falling on our planet consists mainly of two parts, visible and infrared. Either of these can be separately harvested. For example, radiation in the infrared region can be conserved by exciting the vibrations of molecules in the air or in the sea, and the absorbed energy may then contribute to our geothermal and hydro energies. While chemists are aware of the advances in the technology of thermal solar heating developed by engineers, we also try to apply photochemistry in aqueous solutions to tapping solar energy in the visible region via the familiar electronic excitation of dye molecules as an alternative to the existing solar cells. But, why after all are we interested in working with colored compounds instead of the well-studied semiconductors? It is true that physicists have almost perfected the use of semiconductors as solar cells to convert visible light into electricity. Nonetheless, the concentration of solar irradiation and expenses of the fabrication of solar cells still pose practical problems. If a dye molecule and some other chemicals in a solution can be managed to perform a task similar to that found in photosynthetic chloroplasts, i.e. converting light energy into chemical energy, those problems associated with semiconductors are alleviated since solutions can be spread into a larger area and costs may not be as high.

Typically, after a dye absorbs an impinging photon, its excited state returns rapidly to its ground state either by emitting a red-

shifted photon or by radiationless deactivation. In order to capture this absorbed light energy and convert it into chemical energy rather than the less useful thermal energy, the following photochemical processes are frequently pursued.

$$S + h\nu \longrightarrow {}^{*}S \qquad (1)$$

$${}^{*}S \xrightarrow{k_{nr}} S + \text{heat} \qquad (2)$$

$${}^{*}S \xrightarrow{k_{r}} S + h\nu' \qquad (3)$$

$${}^{*}S + A \xrightarrow{k_{q}} S^{+} + A^{-} \qquad (4)$$

$$S^{+} + A^{-} \xrightarrow{k_{2}} S + A \qquad (5)$$

$$D + S^{+} \xrightarrow{k_{4}} D^{+} + S \qquad (6)$$

where ${}^{*}S$ (S = sensitizer) is the excited dye, A an electron acceptor, and D an electron donor. S is called a sensitizer since it has to be recycled like a catalyst. Reactions 2 and 3 are the radiationless and the radiative decay of ${}^{*}S$, respectively. Reaction 4 is an electron-transfer reaction, in which an electron is transferred from the excited S to A. The overall photochemical reaction is

$$A + D \xrightarrow{h\nu} A^{-} + D^{+} \qquad (7)$$

In this way, a large fraction of the absorbed photon energy could be saved in terms of the higher total chemical energy of the photo-products, A^{-} and D^{+}. However, these photo-products usually react rapidly with each other and return to the starting reagents to cause the undoing of the efforts.

$$A^{-} + D^{+} \xrightarrow{k_{8}} A + D \qquad (8)$$

In the next chapter, some approaches to preventing this undesirable back reaction (Eq. 8) will be discussed. Before trying to store the temporarily saved chemical energy, we should first examine photochemical reactions (Eq. 1-4) and the ensuing dark thermal

reactions (Eq. 5, 6 and 8) carefully. Given enough detailed kinetic and mechanistic data, one may then optimize the reaction parameters and better design some system to convert solar energy into a preservable chemical form.

In this chapter, some photo-induced electron-transfer reactions in homogeneous solutions were examined with tris-(2,2'-bipyridine)-ruthenium(II) complex as the sensitizer, methyl-viologen (1,1'-dimethyl-4,4'-bipyridinium^{2+}, MV^{2+}) as the electron acceptor, and ethylene-diamine-N,N,N',N'-tetraacetate (EDTA) as the electron donor. The ruthenium complex has a high extinction coefficient (ε_{max} = 14300 $M^{-1}cm^{-1}$) peaked at 452 nm. While its oxidized complex, $Ru(bpy)_3^{3+}$, has been shown to oxidize water in the presence of oxygen catalysts (e.g. RuO_2), its excited complex is capable of reducing water since it is both a strong reducing agent and a moderate oxiding agent (Figure 1). Below pH 7, the excited ruthenium complex can first reduce MV^{2+}, and the resulting $MV^{+\cdot}$ radical in turn reduces water to form H_2, a fuel with the highest energy per unit weight using oxygen as the oxidant, in the presence of hydrogen catalyst (e.g. Pt). The high extinction coefficient (ε_{max}^{602} = 11300) of $MV^{+\cdot}$ enables us to follow its growth and decay easily. EDTA decomposes irreversibly after its oxidation and thus drives the reactions forward so that the photochemical reaction can be studied by a simple continuous photolysis. Eventually, a more available electron donor such as water should be substituted.

Figure 1. Formal reduction potentials of both the ground state and the excited state of $Ru(bpy)_3^{2+}$, and of MV^{2+} and water at pH 7 and at 25°C.

NHE: normal hydrogen electrode.

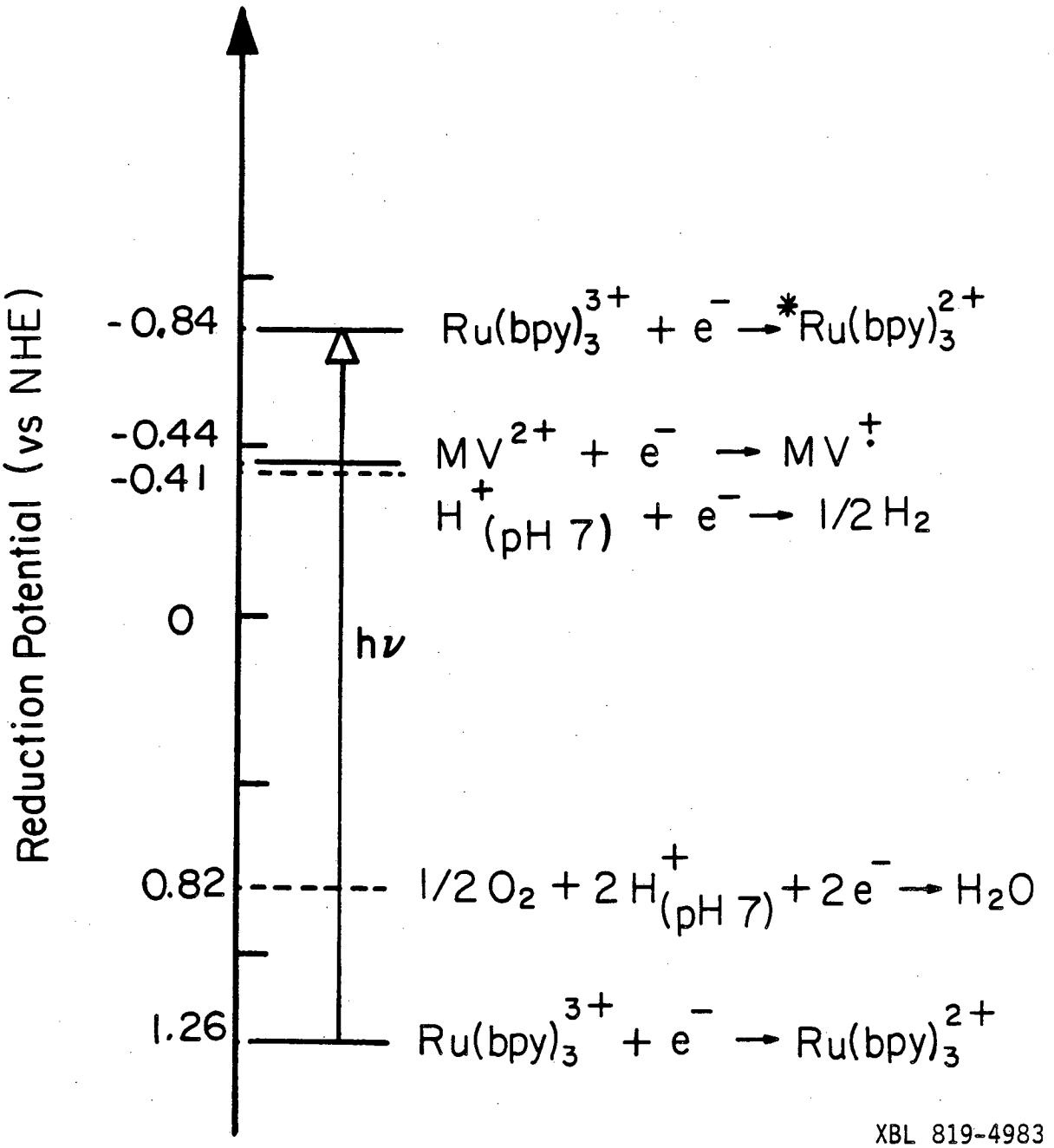
Reduction Potential (vs NHE)
-0.84
-0.44
-0.41
0
0.82
1.26
$Ru(bpy)_3^{3+} + e^- \rightarrow {}^*Ru(bpy)_3^{2+}$
$MV^{2+} + e^- \rightarrow MV^{+\cdot}$
$H^+_{(pH\ 7)} + e^- \rightarrow 1/2\ H_2$
$h\nu$
$1/2\ O_2 + 2\ H^+_{(pH\ 7)} + 2\ e^- \rightarrow H_2O$
$Ru(bpy)_3^{3+} + e^- \rightarrow Ru(bpy)_3^{2+}$

XBL 819-4983

EXPERIMENTAL

(1) Materials

Unless otherwise specified, materials were obtained from commercial supplies and were used without further purification. Water was deionized first, then was twice deionized by a Millipore, Milli.Q Water Purification System.

Tris-(bipyridine)ruthenium(II) chloride (G. F. Smith Co.) was crystallized from water by addition of saturated KCl solution. Methyl viologen was from Aldrich. EDTA solutions at different pHs were prepared by adjusting the pH of disodium (ethylenedinitrilo)tetra-acetate ('Baker Analyzed' reagent) solution.

(2) Experimental procedure

Absorption spectra were taken using a 1.0 cm optical path quartz cuvettes or glass cuvettes on a Cary 118 Spectrophotometer or on a Hewlett-Packard 8450A UV/VIS Spectrophotometer with a HP 7225A Graphics Plotter. Fluorescence spectra were recorded on a Hitachi Perkin-Elmer MPF-2A Spectrophotometer with a 150 W Xenon lamp and a red-sensitive, Type R-136 photomultiplier tube (Hamamatsu TV Co.).

Continuous photolysis was carried out with a collimated beam from either a 1000 watt or a 450 watt Xenon arc lamp (Oriel). Infrared was removed by passing the light through a 10-cm aqueous cupric sulfate solution and visible light was restricted to a narrow band from 400 to 540 nm by two glass filters; one had a sharp UV cut-off at 400 nm, the other was a Corning 5-57.

De-aerated sample solutions were first carefully evacuated and followed by bubbling Ar gas (which was purified by active copper at 150°C) several times and then purged for at least 20 minutes. All

experiments were performed at room temperature.

The flash photolysis apparatus is as described in the previous chapter. Dye solution used was Coumarin 450 in 1:1 methanol and water mixture, and it lased at around 450 nm when 21 KV, 60 joule electrical energy was dissipated in the Xe plasma.

RESULTS AND DISCUSSION

(1) Fluorescence quenching experiments

The metal-to-ligand charge transfer excited state of $Ru(bpy)_3^{2+}$ complex fluoresces strongly in the orange (Figure 2a). The excited state has some triplet character due to the nature of heavy element Ru. Consequently, it decays more slowly than a usual singlet state does. The lifetime (1/e time) was reported to be 0.6 microseconds [1], and was measured with our nanosecond spectral source to be 0.61 μs in a deaerated aqueous solution and 0.39 μs in an air-saturated solution. From the ratio of these two values, the quenching constant k_q of oxygen dissolved in aqueous solutions at room temperature (22±1°C) is estimated to be $3.5 \times 10^9\ M^{-1}s^{-1}$ by the following equation,

$$\tau_o/\tau = 1 + [k_q/k_o] \times [O_2]$$

where τ, τ_o are the excited state lifetimes with and without the quencher oxygen respectively, k_o is the intrinsic decay constant in the aqueous solution and is the inverse of the sum of k_{nr} and k_r. With MV^{2+} as the quencher, the quenching constant, k_q, is calculated to be $8.1 \times 10^8\ M^{-1}s^{-1}$ at 22°C from the Stern-Volmer plot (Figure 2b). It is slightly slower than diffusion-controlled due to the static repulsive interaction between the ruthenium complex and MV^{2+} (Figure 2b).

(2) Continuous photolysis studies

Figure 3 shows the accumulation of $MV^{+\cdot}$ radicals under continuous photolysis in the solutions at pH 7 containing 3.3×10^{-6} M of $Ru(bpy)_3^{2+}$, 1.2×10^{-2} M of MV^{2+}, and three different concentrations of EDTA, 0.1, 0.01, and 0.001 M. The overall mechanism was first proposed

Figure 2. (a) Fluorescence spectrum of $Ru(bpy)_3^{2+}$ in aqueous solution.

(b) Stern-Volmer plot of the excited $Ru(bpy)_3^{2+}$ by methyl viologen at 22°C in aqueous solution. I_0/I is the ratio of fluorescence intensities in the absence of quencher to that in the presence of quencher.

(a)

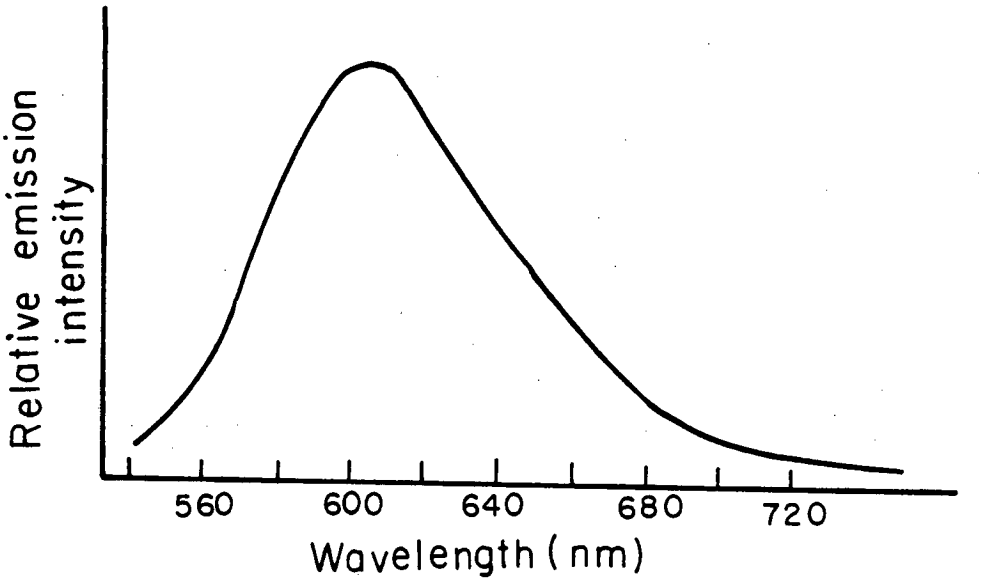

(b)

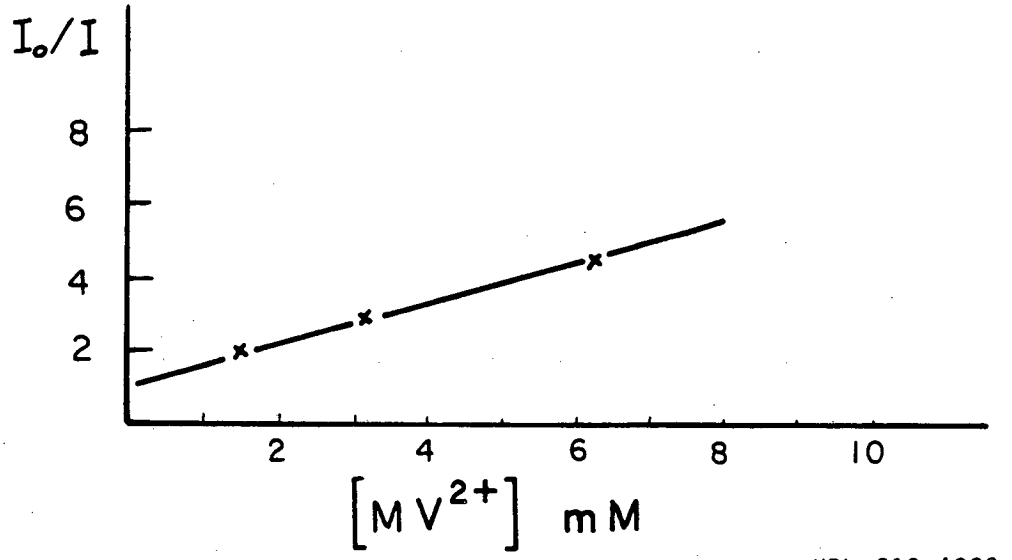

XBL 819-4982

Figure 3. Formation of $MV^{+\cdot}$ radicals under continuous photolysis in the solutions at pH 7 containing 3.3×10^{-6} M of $Ru(bpy)_3^{2+}$, 1.2×10^{-2} M of MV^{2+}, and three different concentrations of EDTA.

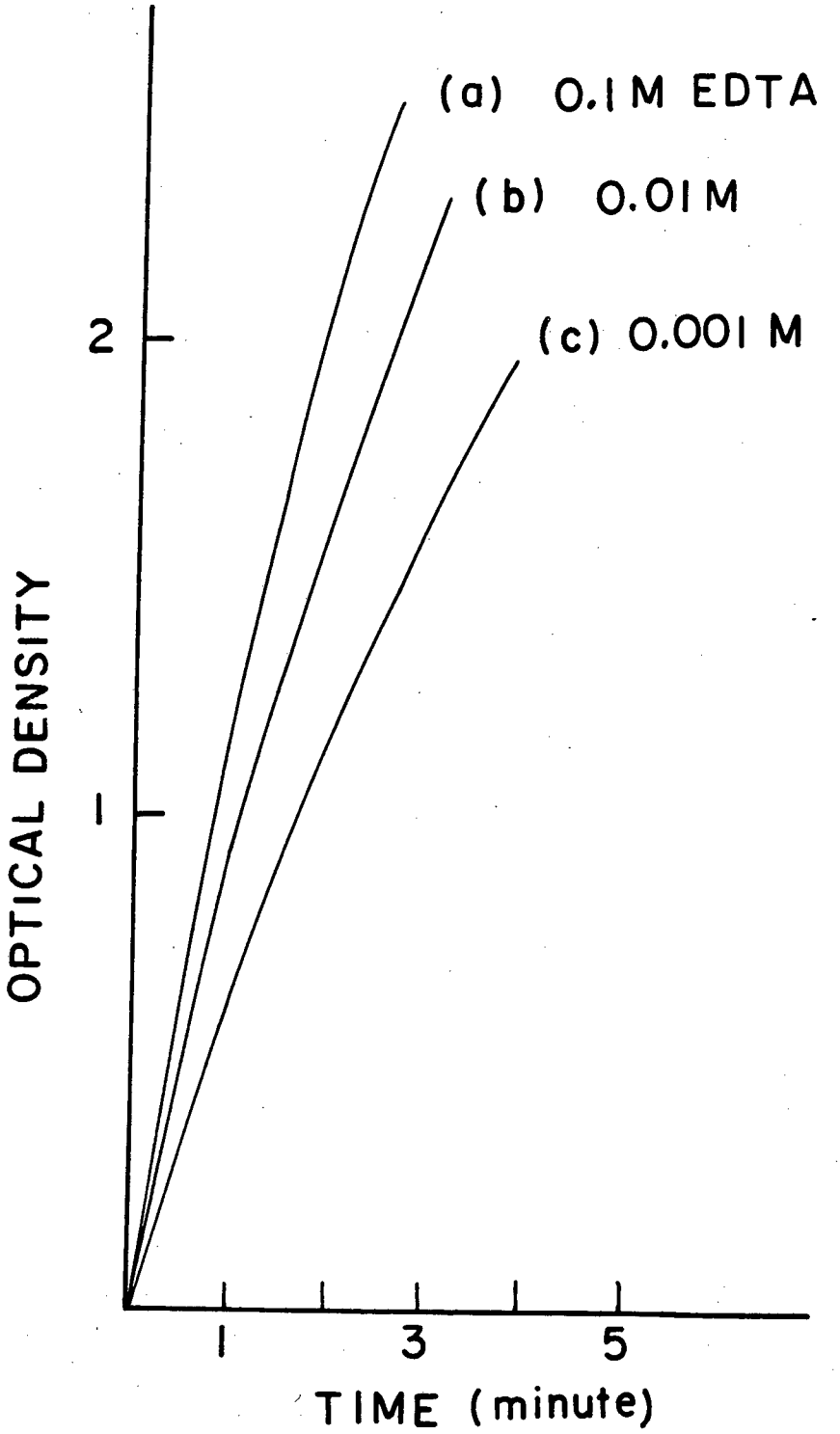

XBL 819-4981

as follows.

$$Ru(bpy)_3^{2+} \xrightarrow{I_{ab}} {}^*Ru(bpy)_3^{2+} \quad (10)$$

$${}^*Ru(bpy)_3^{2+} \xrightarrow{k_0} Ru(bpy)_3^{2+} \quad (11)$$

$${}^*Ru(bpy)_3^{2+} + MV^{2+} \xrightarrow{k_q} Ru(bpy)_3^{3+} + MV^{+\cdot} \quad (12)$$

$$Ru(bpy)_3^{3+} + MV^{+\cdot} \xrightarrow{k_2} Ru(bpy)_3^{2+} + MV^{2+} \quad (13)$$

$$Ru(bpy)_3^{3+} + EDTA \xrightarrow{k_4} Ru(bpy)_3^{2+} + EDTA_{ox} \quad (14)$$

From this mechanism, the variations of reactants, intermediates, and products are derived,

$$d[{}^*Ru^{2+}]/dt = I_{ab} - k_o \times [{}^*Ru^{2+}] - k_q \times [MV^{2+}] \times [{}^*Ru^{2+}] \quad (15)$$

$$d[MV^{+\cdot}]/dt = k_q \times [MV^{2+}] \times [{}^*Ru^{2+}] - k_2 \times [Ru^{3+}] \times [MV^{+\cdot}] \quad (16)$$

$$d[Ru^{3+}]/dt = k_q \times [MV^{2+}] \times [{}^*Ru^{2+}] - k_2 \times [Ru^{3+}] \times [MV^{+\cdot}] - k_4 \times [Ru^{3+}] \times [EDTA] \quad (17)$$

Assuming that $[{}^*Ru^{2+}]$ and $[Ru^{3+}]$ reach steady-state after a very short while, we have

$$d[MV^{+\cdot}]/dt = \frac{I_{ab}}{1 + \frac{k_o}{k_q[MV^{2+}]}} \cdot \frac{1}{1 + \frac{k_2}{k_4[EDTA]}[MV^{+\cdot}]} \quad (18)$$

It is obvious from Figure 3 that the initial slopes at three different concentrations of EDTA are different and thus the contribution from the second term in the above equation should not be neglected. Integrating the above equation, one has

$$K \cdot t = [MV^{+\cdot}] + \frac{1}{2} \cdot \left(\frac{k_2}{k_4[EDTA]}\right) [MV^{+\cdot}]^2 \quad (19)$$

where $K = I_{ab} \Big/ \left[1 + \frac{k_o}{k_q[MV^{2+}]}\right]$

In order to see the effect of the quadratic term on the initial slope, the following coordinate transformation is used.

$$T = t - t_o \quad (20)$$

$$X = [MV^{+\cdot}] - [MV^{+\cdot}]_o \quad (21)$$

Equation 19 becomes

$$K\ (T + t_0) = X\ (1 + \frac{k_2}{k_4[EDTA]} \cdot [MV^{+\cdot}]_0) + \frac{1}{2} \cdot (\frac{k_2}{k_4[EDTA]})\ X^2 \qquad (22)$$

In our experiments, small variations of $[MV^{+\cdot}]$ ($\leq 10^{-6}$ M) were not easy to record and also time interval less than one second could not be resolved. Equation 22 suggests that the initial slope should be

$$K\ /\ (1 + \frac{k_2}{k_4[EDTA]} \cdot [MV^{+}]_0) \qquad (23)$$

instead of K.

By substituting $k_2 = 10^9\ M^{-1}s^{-1}$, $k_4 = 10^6\ M^{-1}s^{-1}$, and $[MV^{+\cdot}] = 10^{-6}$ M into the apparent slope function and varying the concentration of EDTA, we find that the calculated slopes comform to our experimental results, as shown in Figure 4. However, if [EDTA] is smaller than 10^{-4} M, the steady-state assumption of $[Ru(bpy)_3^{3+}]$ cannot hold , and $[Ru(bpy)_3^{3+}]$ decreases rapidly as $MV^{+\cdot}$ radicals build up.

(3) Flash photolysis studies

To obtain the rate constant k_2 of the back reaction (equation 13) and k_4 of the reductive reaction of EDTA (equation 14) simultaneously, the following experiments were carried out. In a cuvette containing 3.3×10^{-5} M of $Ru(bpy)_3^{2+}$, 1.2×10^{-2} M of MV^{2+}, and 0.8 mM of EDTA aqueous solution at pH 7, the decay of $MV^{+\cdot}$ was first recorded without pre-illumination, and then after several exposures of this cuvette to sunlight a set of decay curves of $MV^{+\cdot}$ were acquired at different concentrations of pre-generated $MV^{+\cdot}$. By curve simulation with the following rate equations derived from the proposed mechanism,

$$d[MV^{+\cdot}]/dt = -k_2\ [MV^{+\cdot}]\ [Ru(bpy)_3^{3+}] \qquad (24)$$

$$d[Ru(bpy)_3^{3+}] = -k_2\ [MV^{+\cdot}]\ [Ru(bpy)_3^{3+}] - k_4\ [Ru(bpy)_3^{3+}]\ [EDTA] \qquad (25)$$

we have estimated k_2 to be $2.3 \times 10^9\ M^{-1}s^{-1}$ and k_4 to be $8 \times 10^6\ M^{-1}s^{-1}$ from Curve 1 in Figure 5. A general purpose program used is

Figure 4. Calculated slope as a function of EDTA concentraion.

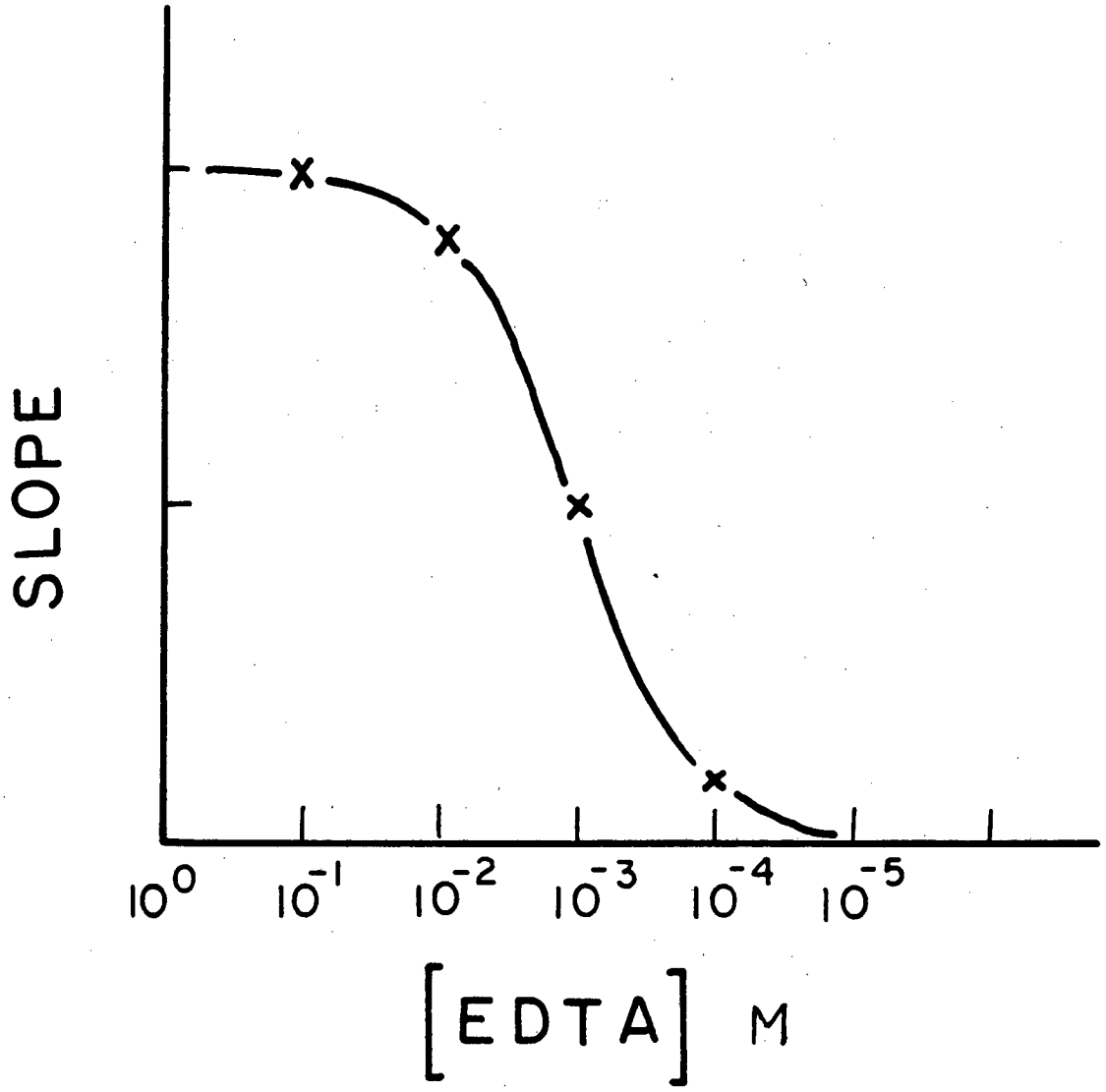

XBL 819-4995

Figure 5. Transient absorption changes of $MV^{+\cdot}$ radicals followed as 602 nm.

$[Ru(bpy)_3^{2+}] = 3.3 \times 10^{-5}$ M

$[MV^{2+}] = 1.2 \times 10^{-2}$ M

[EDTA] = 0.8 mM

The pre-generated $[MV^{+\cdot}]$ was

(1) ~0 M

(2) 2.4×10^{-5} M

(3) 3.94×10^{-5} M

(4) 6.5×10^{-5} M

(5) 8.85×10^{-5} M (OD = 1.00)

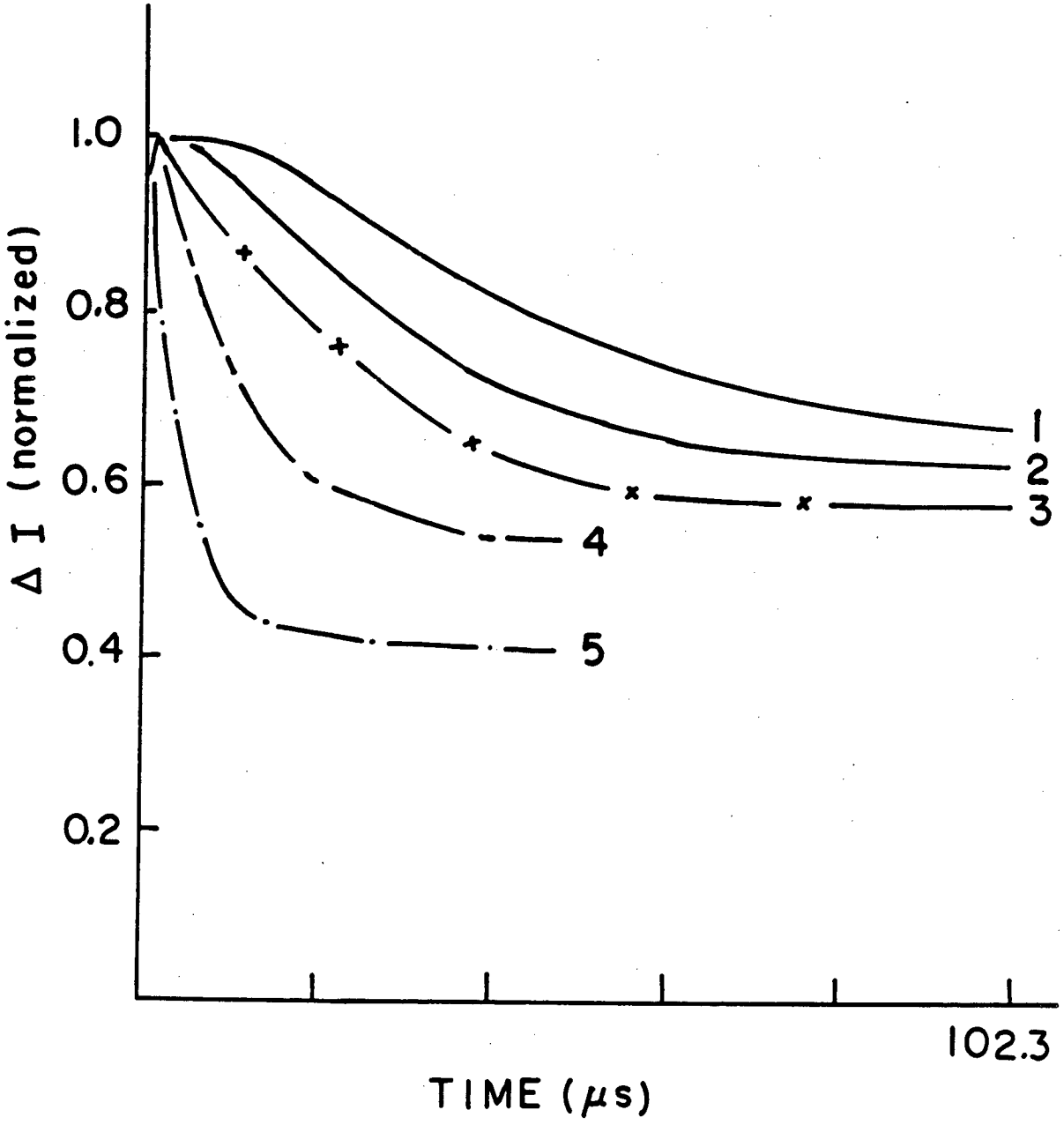

XBL 819-4994

attached in the appendix of this chapter. These values are very reasonable and in fairly good agreement with the data obtained from the experiment with a different electron donor, triethanol amine, reported in the literature [2]. But, we could not fit the other experimental data with these same two constants. The decay of $MV^{+\cdot}$ was too slow and the residual amount of $MV^{+\cdot}$ was too high. We concluded that the simple mechanism proposed above was not enough to represent the actual details.

a. Two-component system,---- $Ru(bpy)_3^{2+}$ and MV^{2+}

EDTA was first eliminated from the above solution so that the back reaction (equation 13) could be separately studied. Although the back reaction should be simply bimolecular, it might be complicated by the existing photo-generated $MV^{+\cdot}$; e.g., complexation or dimerization in the experimental conditions. To find out this, we introduced $MV^{+\cdot}$ on purpose into the solution without any added reducing agent. Usually, $MV^{+\cdot}$ was chemically reduced by dithionite, but the residual reductive agent might interfere the reaction. In our experiment, $MV^{+\cdot}$ was first produced on a gold electrode by electrochemical reduction and then added into Ar-purged solutions. Any possible interference of the oxidative product from the other electrode was avoided by separating the copper anode with a glass frit (PAR, Vycor tip) such that Cu ions were all confined to a separate compartment.

From the decay curves monitored at 602 nm, we found that the back reaction followed a simple bimolecular reaction kinectics up to 7.2×10^{-5} M of $MV^{+\cdot}$ (OD 0.8 at 602 nm). k_2 was estimated to be $1.3 \times 10^9\ M^{-1}s^{-1}$ (Figure 6a). With the introduction of 0.1 M salt NaCl, k_2 increased to $2.5 \times 10^9\ M^{-1}s^{-1}$. This increase is expected since the electrostatic repulsive interaction between $Ru(bpy)_3^{3+}$ and $MV^{+\cdot}$

is reduced by increasing the ionic strength (Figure 6b and 6c). The quantum yields in terms of the maximal $MV^{+\cdot}$ generated in the flash together with a summary of these experiments (#2-3) are tabulated in Table 1. The decrease of the initial photo-induced $MV^{+\cdot}$ in the presence of higher concentration of electrochemical generated $MV^{+\cdot}$ might be attributed to the statistical static reduction of $Ru(bpy)_3^{3+}$ by nearby thermalized $MV^{+\cdot}$ radicals. Also, increasing the ionic strength might decrease the probability of cage separation of Ru^{3+} and $MV^{+\cdot}$. However these suppositions cannot be resolved with our photolysis system.

b. Three-component system, ---- $Ru(bpy)_3^{2+}$, MV^{2+}, and EDTA

In the presence of 0.1 M of pH 7 EDTA, photo-induced $MV^{+\cdot}$ does not decay at all and the yield is about twice the amount produced in a solution without EDTA (Figure 7a and Table 1). This indicates that a second reduction might occur. Actually, a second growth of $MV^{+\cdot}$ could be clearly seen when the scan rate increased. It followed very closely the initial instantaneous jump of photochemically generated $MV^{+\cdot}$, as shown by comparing Figure 7b and 7c. In order to have a better look at this second non-photochemical production of $MV^{+\cdot}$, a smaller amount of EDTA (1mM) was added into Solution 1 of the previous experiment (see Table 1, Solution 1') so that the second growth could be slowed down. Also examined was a solution having 0.1 M of pH 5.15 EDTA (Solution 5) to confirm this possibility. Both showed a visible second growth of $MV^{+\cdot}$ within 10 μs after the laser flash (Figure 8).

The fact that a slower thermal growth of $MV^{+\cdot}$ at pH 5.15 can be observed (as compared to that in a pH 7 solution) is attributed to a decrease of the effective concentration of reductive EDTA, which should have at least one non-protonated N center to be a good reducing agent,

TABLE 3 - 1

QUANTUM YIELDS OF PHOTO-INDUCED $MV^{+\cdot}$ IN FLASH PHOTOLYSIS EXPERIMENTS[a]

#	$Ru(bpy)_3^{2+}$ [μM]	MV^{2+} [mM]	$MV^{+\cdot}$ [μM]	EDTA [M]	NaCl [M]	ΔMV^{+}_{max} [μM]	φ [%]
(A) TWO-COMPONENT SYSTEMS							
1	29.4	5.0	——	——	——	2.42	8.2
2	30.0	5.0	30.8	——	——	1.97	6.5
3	30.0	5.0	72.4	——	——	1.70	5.6
2'	28.5	4.6	27.0	——	0.1	1.64	5.8
(B) THREE-COMPONENT SYSTEMS							
$1'_a$	30.0	5.0	——	1 mM(7)	——	3.60	12.0
$1'_b$	30.0	5.0	82.0	1 mM(7)	——	2.00	6.7
4	32.5	5.0	——	0.1 M(7)	——	5.40	16.7
5	32.4	5.0	——	0.1 M(5.1)	——	2.80	9.2
3	30.6	5.0	24.5	——	——	2.10	7.0
$3'_a$	29.5	5.0	——	.83mM(7)	——	3.00	10.1
$3'_b$	29.5	5.0	29.3	0.8mM(7)	——	2.10	7.1
$3'_c$	29.5	5.0	45.1	.78mM(7)	——	1.84	6.2
$3''_a$	27.3	4.6	——	.75mM(7)	0.1	1.62	5.9
$3''_b$	27.3	4.6	30.2	.72mM(7)	0.1	1.40	5.1

a. In calculating the quantum yields, we assume that all $Ru(bpy)_3^{2+}$ are excited by laser flash. A = 0.43 at 450 nm, and the intensity of laser flash is high enough to saturate ruthenium complex in the solution.

Figure 6. Transient absorption changes of $MV^{+\cdot}$ followed at 602 nm. All solutions contained

$[Ru(bpy)_3^{2+}] = 2.94 \times 10^{-5}$ M

$[MV^{2+}] = 5$ mM

(a) simple two-component system: 0 M of $MV^{+\cdot}$

(b) with $MV^{+\cdot}$ generated by electrochemical method.

$[MV^{+\cdot}] = 3.08 \times 10^{-5}$ M

(c) $[MV^{+\cdot}] = 2.7 \times 10^{-5}$ M and

0.1 M of NaCl.

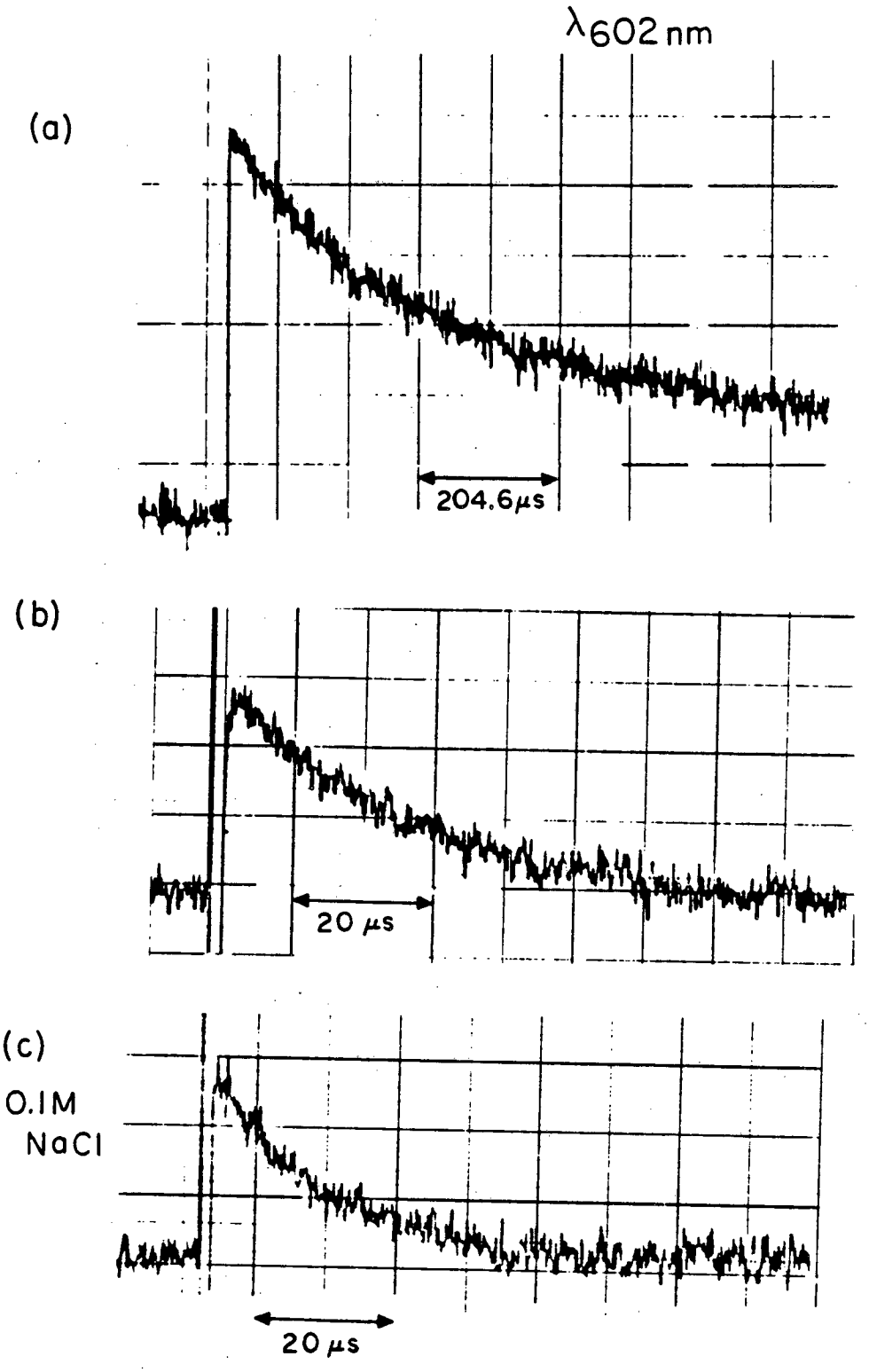

XBL 819-4992

Figure 7. Transient absorption changes of $MV^{+\cdot}$ followed at 602 nm. All solutions contain ca. 3×10^{-5} M of $Ru(bpy)_3^{2+}$ and 5 mM of MV^{2+}.

(a) with 0.1 M EDTA (pH 7.0),

(b) same as (a) except a higher digitizing rate.

(c) with 0 M of EDTA.

(a)

pH 7

0.1 M EDTA

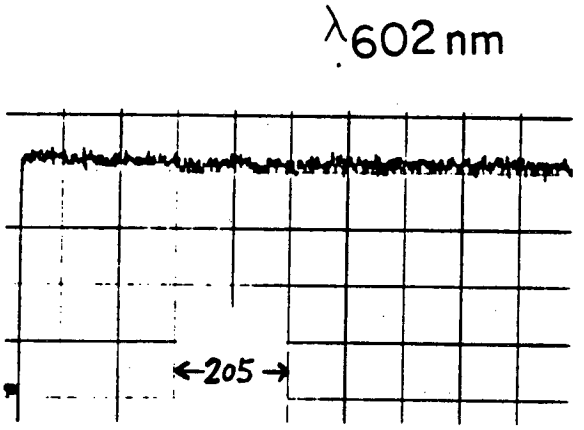

(b)

pH 7

0.1 M EDTA

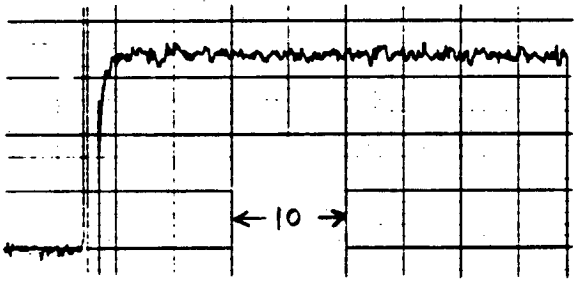

(c)

0 M EDTA

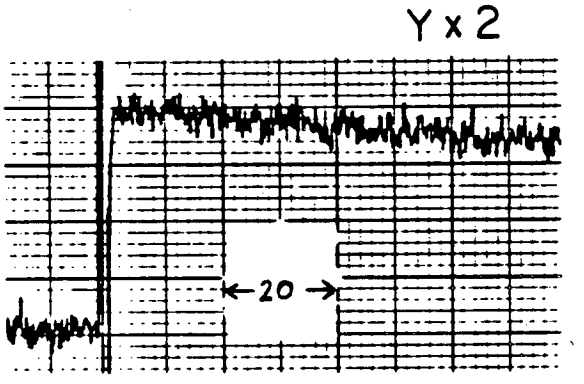

XBL 819-4990

Figure 8. Transient absorption changes of $MV^{+\cdot}$ followed at 602 nm.

(a) 1 and 2 were with a solution containing 3×10^{-5} M of $Ru(bpy)_3^{2+}$, 5 mM of MV^{2+}, and 1 mM of EDTA at pH 7. 3 was in the same solution as 1 and 2 except it contained pre-generated 8.2×10^{-5} M of $MV^{+\cdot}$.

(b) both 1 and 2 contained 3.25×10^{-5} M of $Ru(bpy)_3^{2+}$, 5 mM of MV^{2+}, and 0.1 M of EDTA at pH 5.1 except the digitizing rate of 2 was ten time faster.

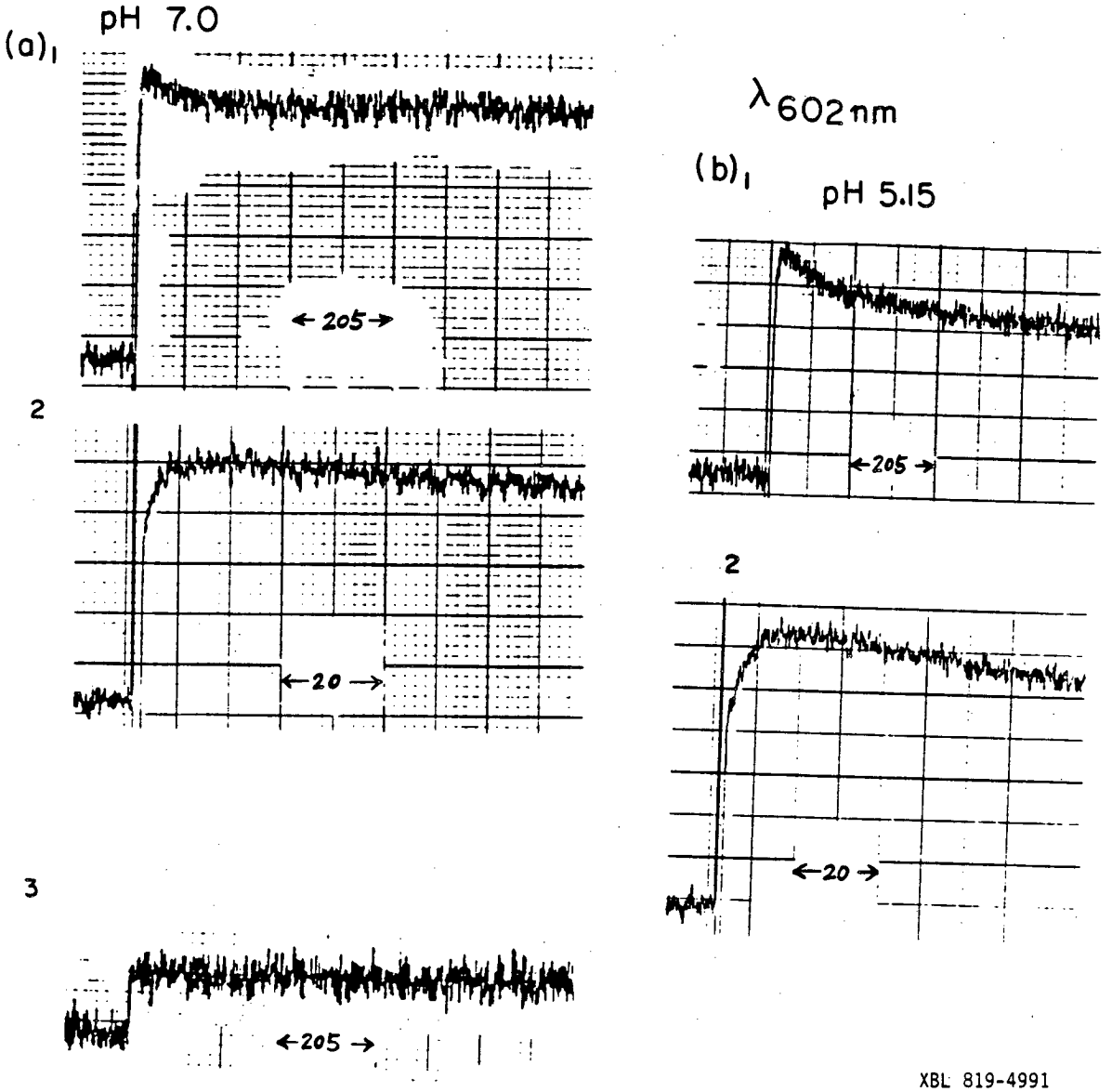

XBL 819-4991

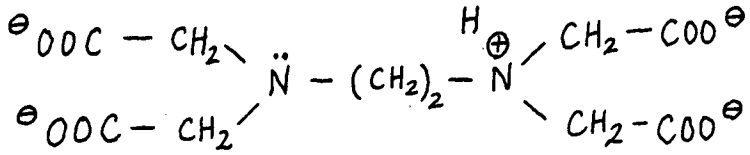

From the pKs of EDTA, the fraction of effective EDTA in a solution at 20°C and having an ionic strength of 0.1 is calculated to be 8.9% at pH 5.15 and 87.3% at pH 7 [3].

Keller et al. have proposed the following mechanism for the decomposition of EDTA after its first oxidation [4],

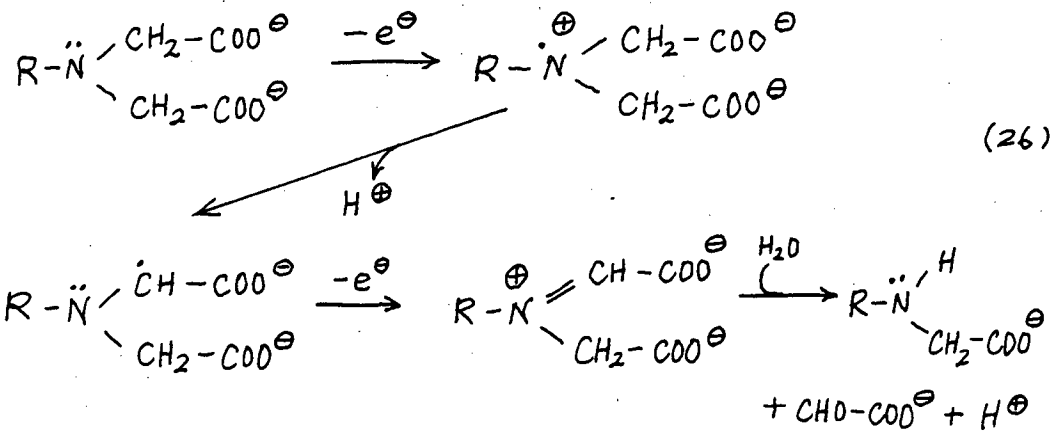

(26)

The net photo-chemical reaction thus can be described as

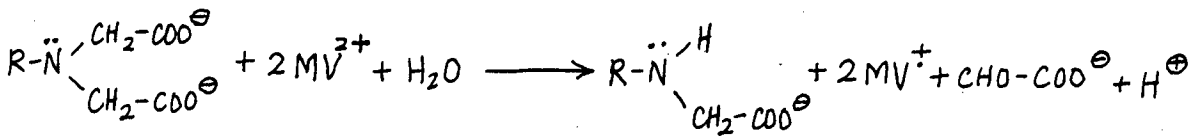

(27)

With this and also our observations, the reaction mechanism should be modified to be

$$Ru^{3+} + MV^{+\cdot} \xrightarrow{k_2} Ru^{2+} + MV^{2+} \quad (28)$$

$$Ru^{3+} + EDTA \xrightarrow{k_4} Ru^{2+} + EDTA_{ox} \quad (29)$$

$$EDTA_{ox} + MV^{+\cdot} \xrightarrow{k_5} EDTA + MV^{2+} \quad (30)$$

$$EDTA_{ox} \xrightarrow{k_6} (EDTA)^{-H} \quad (31)$$

$$(EDTA)^{-H} + MV^{2+} \xrightarrow{k_7} (EDTA)_p + MV^{+\cdot} \quad (32)$$

The inclusion of equations 30 and 31 was suggested by a similar oxidation mechanism found with triethanol amine [5].

Even with this modification of the reaction mechanism, we still were not able to explain some of the qualitative features observed in the decay curves of $MV^{+\cdot}$. For example, the fact that the second reduction (eq.32) takes place so fast, in the first 10 μs after the laser flash, implies that reactions 31 and 32 proceed much faster than reactions 28 and 30. Why can we observe the decaying section after $MV^{+\cdot}$ reaches its maximum (Figure 8a)? Why could not all $Ru(bpy)_3^{3+}$ react with EDTA to produce two equivalents of $MV^{+\cdot}$? (See Figure 8b and Solution 5 in Table 1.)

Apparently, following the decays at 602 nm only, where $MV^{+\cdot}$ absorbed, could not tell us the complete story. Simultaneous monitoring of the decaying behavior of $Ru(bpy)_3^{3+}$ at 452 nm was necessary and was carried out with Solutions 1', 4, 5, as well as Solution 3 without and with added EDTA (Solution 3'). The results are shown in Figure 9 and Figure 10b-10d. From the decays monitored at 452 nm, we first estimated k_4 to be $8\pm1 \times 10^7\ M^{-1}s^{-1}$, which was in good agreement with the reported value, $1.1 \times 10^8\ M^{-1}s^{-1}$ [4]. To obtain this result, probing light at around 452 nm had to be allowed to pass through the cuvette at least for half a second with our present detecting system, and it created 10^{-5} M of $MV^{+\cdot}$ within that small probed area at the time when laser was triggered. However, this will only speed up the recovery of $Ru(bpy)_3^{3+}$ slightly as proved by computer simulation, so k_4 remains valid.

By comparing the curves monitored at 452 nm and 602 nm, we can conclude that reactions 31 and 32 proceed very rapidly after the first oxidation of EDTA because the second growth of $MV^{+\cdot}$ follows very closely the recovery of $Ru(bpy)_3^{3+}$ in each case. Lower limits of these two rate

Figure 9. Transient absorption changes of $MV^{+\cdot}$ followed at 602 nm (shown on the left hand side of page) and $Ru(bpy)_3^{2+}$ at 452 nm (on the right hand side).

(a) $[Ru(bpy)_3^{2+}] = 3.06 \times 10^{-5}$ M

$[MV^{2+}] = 5$ mM

$[MV^{+\cdot}] = 2.45 \times 10^{-5}$ M.

(b) $[Ru(bpy)_3^{2+}] = 2.95 \times 10^{-5}$ M

$[MV^{2+}] = 5$ mM

$[EDTA] = 8.3 \times 10^{-4}$ M at pH 7

(c) (b) plus 2.93×10^{-5} M of $MV^{+\cdot}$

(d) $[Ru(bpy)_3^{2+}] = 2.73 \times 10^{-5}$ M

$[MV^{2+}] = 5$ mM

$[EDTA] = 7.5 \times 10^{-4}$ M at pH 7

$[NaCl] = 0.1$ M

(e) (d) plus 3.02×10^{-5} M of $MV^{+\cdot}$

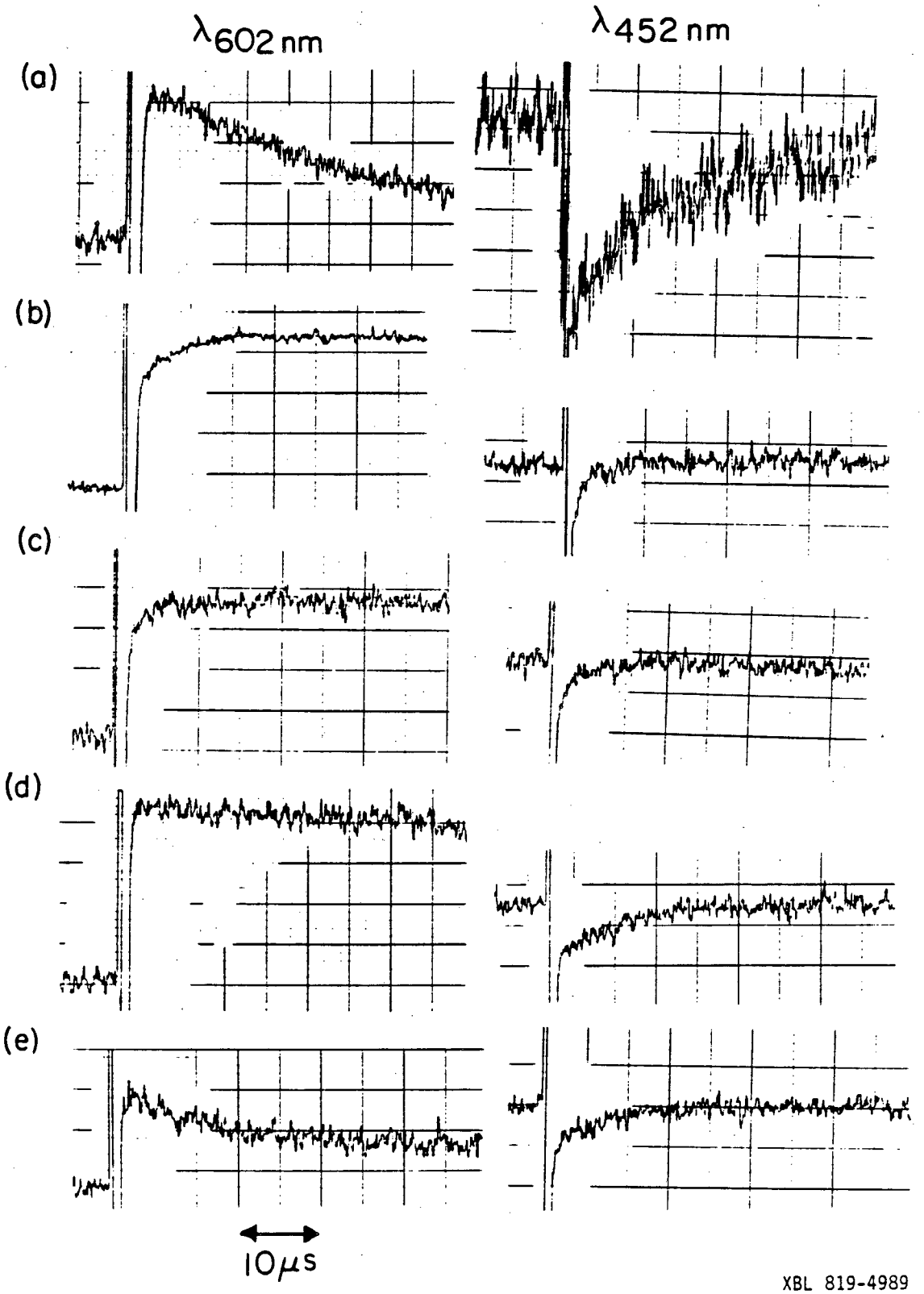

XBL 819-4989

Figure 10. Transient absorption changes of $Ru(bpy)_3^{2+}$ followed at 452 nm.

(a) noise due to light scattering and other electronic artifacts from flashlamp.

All the following solutions contained ca. 3×10^{-5}M of $Ru(bpy)_3^{2+}$, 5 mM of MV^{2+} and

(b) with 0.1 M of EDTA at pH 7.0,

(c) with 0.1 M of EDTA at pH 5.0, and

(d) with 0.7 mM of EDTA at pH 7.0.

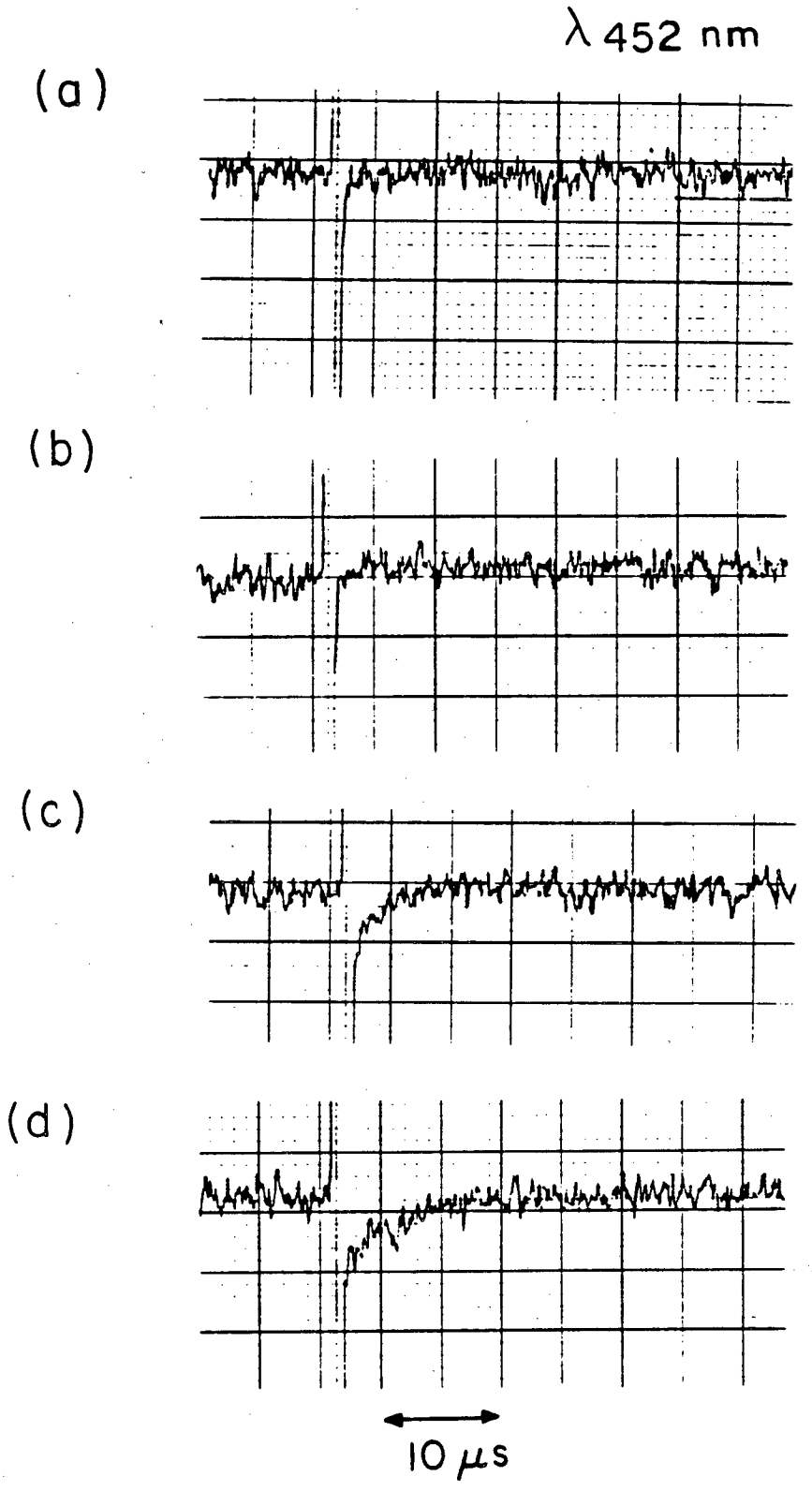

XBL 819-4988

constants, k_5 and k_6, are estimated to be 8×10^6 s^{-1} and 1.6×10^9 $M^{-1}s^{-1}$ respectively.

In order to account for the slow decay of $MV^{+\cdot}$ after $MV^{+\cdot}$ reaches its maximum in solution 5 and other solutions with lower concentration of EDTA, we have tried to add some reactions into the above proposed mechanism, but we found none of our trials could fit the data well. Finally, we had to conclude that a secondary reaction between $MV^{+\cdot}$ and an oxidized intermediate of EDTA might take place after EDTA donated its second electron and before the oxidized EDTA was hydrolyzed. Such a secondary back reaction might be prevented in a solution having right pH and with a large excess of EDTA. One more point we noticed in experiments with Solution 3 (Figure 9) was that by increasing the concentration of inert salt, NaCl, the initial second growth of $MV^{+\cdot}$ was largely suppressed and the recovery of Ru^{3+} was slowed down. This might be due to the decreased interaction between Ru^{3+} and $EDTA^{2-}$ in the present of a large excess of chloride ions. With a rate constant much smaller than a diffusion-controlled, the encountering molecules ($Ru(bpy)_3^{3+}$ and $EDTA^{3-}$) in reaction 29 must be in a right geometry and in a close distance in order to effect the desired reaction.

Although we have left several un-resolved reactions in this chapter, we feel that enough information has been collected to pursue our further experiments in heterogeneous solutions. In this chapter, the fluorescence lifetime and some quenching constants of excited $Ru(bpy)_3^{2+}$ have been measured, and the mechanism as well as the kinetics of the reductive reactions of EDTA have been studied to certain extent. That unknown secondary reaction decreases the overall quantum yield in terms of the amount of $MV^{+\cdot}$ radicals generated, but

the nature of the intermediate involved is certainly not of our primary concern at this moment.

APPENDIX

```
 PROGRAM CURSIM4
C THIS IS USED TO SIMULATE THE DATA OBTAINED FROM FLASH PHOTOLYSIS
C THE EQUATIONS ARE    -dX/dt = k2*X*Y - K5*Z + K7*X*Z
C         -dY/dt = k2*X*Y + K4*Y
C                      -dZ/dt = -k4*Y  + k5*Z + K7*X*Z
C
 REAL XINIT,YINIT,K2,K4,K5,K7,DT,K2XY,QXEXT,QYEXT,QOPTLEN
 REAL XTEMP,YTEMP,P,Q,R,XSCALE,YSCALE,XORIG,XO,YO
 INTEGER N, NSTEP,NMORE,XEXT,YEXT,OPTLEN,NGAP,NWRONG
 DIMENSION X(4001),Y(4001),Z(4001),TIME(4001)
 CHARACTER*1 ANSWER1,ANSWER2,ANSWER3,ANSWER4,ANSWER5,XPN,YPN
 CHARACTER*1 ANSWERO
C
C READ IN SOME PARAMETERS FOR THE ABOVE EQUATIONS.
 WRITE (6,13)
13 FORMAT(/,' INPUT THE EXTINCTION COEFS OF X,Y,AND THE OPTICAL
 1 LENGTH OF CURVETT.',/,'$XEXT,YEXT,OPTLEN(mm)   [2I6,I2] : ')
 READ (5,16) XEXT,YEXT,OPTLEN
16 FORMAT(2I6,I2)
C
 WRITE (6,402)
402 FORMAT(/,' TELL ME WHETHER X & Y ARE POSITIVE OR NEGATIVE?',/,
 1 ' TYPE IN N IF ABSORPTION INCREASES,P IF ABS DECREASES.',/,
 2 '$X[P/N],Y[P/N] ARE  [2A1] (Type in PN, NP, PP, or NN)  : ')
   READ (5,403) XPN,YPN
403   FORMAT(A1,A1)
C
1 CONTINUE
 WRITE (6,100)
100 FORMAT(//,'$XINIT & YINIT, AND ZINIT  [3E12.0]  :  ')
 READ (5,101) XINIT,YINIT,ZINIT
101 FORMAT(3E12.0)
 WRITE (6,104)
104 FORMAT(/,'$TIME INCREMENT  DT,   [E12.0]  :  ')
 READ (5,105) DT
105 FORMAT(E12.0)
```

```
C TO CALCULATE THE DELTA X ONLY
 XORIG=XINIT-YINIT-ZINIT
C
2 WRITE (6,102)
102 FORMAT(/,'$K2, K4, K5, AND K7 [4E12.0]  :  ')
 READ (5,103) K2,K4,K5,K7
103 FORMAT(4E12.0)
1030 WRITE (6,106)
106 FORMAT(/,' THE DIMENSIONS OF BOTH X,Y,AND Z ARE 4001 !',/,
 1'$HOW MANY STEPS TO COMPUTE? [I4]  : ')
 READ (5,107) NSTEP
107 FORMAT(I4)
 WRITE (6,1071) NSTEP
1071  FORMAT(' THE NUMBER OF STEP IS : ', I4)
 IF (NSTEP.EQ.0) GOTO 3001
C
 WRITE (6,108)
108 FORMAT('$DO YOU HAVE ANY MISTAKE IN THE INPUT DATA?[Y/N] :  ')
 READ (5,109) ANSWER1
109 FORMAT(A1)
 IF (ANSWER1.EQ.'Y') GOTO 1
C
C STORE THE INITIAL PARAMETERS IN FILE FOR003.DAT
 WRITE (3,199)
199 FORMAT(' ******   PROGRAM CURVE-SIMULATION   ******')
 WRITE (3,200) XINIT,YINIT,K2,K4,DT
200 FORMAT(//,' XINIT =',E12.5,/,' YINIT =',E12.5,//,' K2 =',E12.5,
 1/,' K4 =',E12.5,//,' TIME INTERVAL DT =',E12.5)
 WRITE (3,2011) ZINIT, K5,K7
2011 FORMAT(/' ZINIT =',E12.5/' K5 =',E12.5/' K7 =',E12.5)
 WRITE (3, 18) XEXT,YEXT,OPTLEN
18 FORMAT(/,' EXT COEF OF X IS: ',I6,/,' EXT COEF OF Y IS: ',I6,
 1/,' OPTICAL LENGTH IS: ',I2,'MILLIMETERS')
C
C MODIFIED EULER METHOD IS USED TO DO THE NUMERICAL ANALYSIS.
 X(1)=XINIT
```

```
 Y(1)=YINIT
 Z(1)=ZINIT
 TIME(1)=0
 N=2
 GOTO 299
C
280 CONTINUE
 WRITE (6,281)
281 FORMAT(/,'$HOW MANY MORE STEPS DO YOU WANT? [I4]  : ')
 READ (5,282) NMORE
282 FORMAT(I4)
 NSTEP=NSTEP+NMORE
 WRITE (6,648) NSTEP
 WRITE (6,8544) DT
C STARTS COMPUTATION
299 CONTINUE
 DO 300 I=N,NSTEP+1
     K2XY=K2*X(I-1)*Y(I-1)
     P=X(I-1)-DT*(K2XY-K5*Z(I-1)+K7*X(I-1)*Z(I-1))
     Q=Y(I-1)-DT*(K2XY+K4*Y(I-1))
     R=Z(I-1)+DT*(K4*Y(I-1)-K5*Z(I-1)-K7*X(I-1)*Z(I-1))
     IF ((P.LE.0.0).OR.(Q.LE.0.0).OR.(R.LT.0.0))  GOTO 999
       X(I)=X(I-1)-0.5*DT*(K2XY+K2*P*Q-K5*Z(I-1)-K5*R+K7*P*R
 1          +K7*X(I-1)*Z(I-1))
       Y(I)=Y(I-1)-0.5*DT*(K2XY+K4*Y(I-1)+K2*P*Q+K4*Q)
       Z(I)=Z(I-1)+0.5*DT*(K4*Y(I-1)-K5*Z(I-1)+K4*Q-K5*R-
 1          K7*X(I-1)*Z(I-1)-K7*P*R)
          TIME(I)=TIME(I-1)+DT
300 CONTINUE
3001 N=NSTEP+2
 WRITE (6,301)
301 FORMAT('$MORE STEPS? [Y/N]  : ')
 READ (5,302) ANSWER2
302 FORMAT(A1)
 IF (ANSWER2.EQ.'Y')  GOTO 280
C
```

```
 WRITE (6,400)
400 FORMAT(/,' NOW YOUR DATA ARE IN MOLAR! DO YOU WANT TO CONVERT
 1THEM INTO RESULTS',/,'$IN TERMS OF THE INTENSITY OF SIGNAL?
 2 [Y/N]  : ')
 READ (5,401) ANSWER3
401 FORMAT(A1)
 IF (ANSWER3.EQ.'Y') THEN
C CHANGE X INTO DELTA X
C
 DO 4030 I=1,NSTEP+1
   X(I)=X(I)-XORIG
          IF (X(I).LT.0.0) GOTO 999
4030 CONTINUE
C
 IF (XPN.EQ.'N') THEN
          DO 4031 I=1,NSTEP+1
             X(I)=-1.0*X(I)
4031          CONTINUE
 ENDIF
 IF (YPN.EQ.'N') THEN
          DO 4032 I=1,NSTEP+1
      Y(I)=-1.0*Y(I)
4032          CONTINUE
 ENDIF
 WRITE(3,4051)
4051 FORMAT(/,' $$$ THIS SECTION USE A SIGNAL INTENSITY UNIT !!')
 WRITE (3,4052) XORIG
4052 FORMAT(/,' [X] BEFORE FLASH  = ',E12.5)
   QXEXT=FLOAT(XEXT)
   QYEXT=FLOAT(YEXT)
   QOPTLEN=FLOAT(OPTLEN)/10.0
C
 DO 500 I=1,NSTEP+1
      XTEMP=X(I)*QXEXT*QOPTLEN
      YTEMP=Y(I)*QYEXT*QOPTLEN
  X(I)=-1.0+10**XTEMP
```

```
        Y(I)=-1.0+10**YTEMP
500 CONTINUE
 ENDIF
C
 IF (ANSWER3.NE.'Y') THEN
 DO 5990 I=1,NSTEP+1
 X(I)=X(I)-XORIG
 IF (X(I).LT.0.0) GOTO 999
5990 CONTINUE
 ENDIF
C
C COMPARE YOUR DATA WITH THE ACTUAL EXP DATA AND DETERMINE WHAT
C CONVERSION FACTOR YOU NEED FOR THE CURVE SIMULATON.
 WRITE (6,599)
599 FORMAT(/,'$DO YOU NEED SCALING FACTORS? [Y/N]  : ')
 READ (5,5991) ANSWER4
5991 FORMAT(A1)
 IF (ANSWER4.EQ.'Y') THEN
 WRITE (6,600)
600 FORMAT(//,' THE FOLLOWING DATA ARE FOR THE DETERMINATION OF
 1 SCALING',/,' FACTORS YOU NEED TO SIMULATE DATA !',/,6X,'XXXX'
 2,15X,'   YYYY')
  WRITE (6,601) (X(I),Y(I),I=1,4)
601  FORMAT(1X,E12.5,10X,E12.5)
 WRITE (6,6011)
6011 FORMAT(' WHAT IS THE X(0) AND Y(0) YOU LIKE TO SCALE UP ?
 1[2F12.0]',/,'$X(0) , Y(0)   : ')
 READ (5,6012) X0,Y0
6012 FORMAT(2F12.0)
 XSCALE=X0/X(1)
 YSCALE=Y0/Y(1)
 WRITE(3,6031) XSCALE,YSCALE
6031 FORMAT(/, ' THE SCALING FACTORS CHOSEN ARE ',/,' XSCALE : ',
 1E12.5,/,' YSCALE : ',E12.5)
    DO 6030 I=1,NSTEP+1
  X(I)=XSCALE*X(I)
```

```
  Y(I)=YSCALE*Y(I)
6030    CONTINUE
 ENDIF
C
C STORE THE RECORD IN FILE FOR003.DAT.
 WRITE (6,648) NSTEP
648 FORMAT(' TOTAL # OF STEPS IS  : ',I4)
 NGAP=1
 WRITE (6,649)
649 FORMAT('$DO YOU WANT TO PRINT OUT THE COMPLETE FILE OR NOT ?
 1 [Y/N]  ')
 READ (5,6491) ANSWERO
6491 FORMAT(A1)
 IF (ANSWERO.NE.'Y') THEN
 WRITE(6,6492)
6492 FORMAT('$WHAT IS THE # OF STEPS BETWEEN THE DATA TO
 1RECORD ? [I4]  ')
  READ (5,6493) NGAP
6493  FORMAT(I4)
 ENDIF
 WRITE (6,650)
650 FORMAT(' YOUR DATA FILE IS FOR003.DAT !')
 WRITE (3,700) NSTEP
700  FORMAT(/,' TOTAL # OF STEPS IS : ',I4,//)
 WRITE (3,750)
750  FORMAT(5X,'TIME',16X,'XXXXXX',16X,'YYYYYY',16X,'ZZZZZZ',/)
 WRITE (3,800) (TIME(I),X(I),Y(I),Z(I),I=1,NSTEP+1,NGAP)
800 FORMAT(1X,E12.3,10X,E12.5,10X,E12.5,10X,E12.5)
C
 WRITE (3,801)
801 FORMAT(//,' ******** END OF A SECTION *********')
 WRITE (6,802)
802 FORMAT('$DO YOU WANT TO TAKE A LOOK AT YOUR DATA? [Y/N] ')
 READ (5,803) ANSWER5
 IF (ANSWER5.EQ.'Y') THEN
 WRITE (6,750)
```

```
 WRITE (6,800) (TIME(I),X(I),Y(I),Z(I),I=1,NSTEP+1,NGAP)
 ENDIF
 GOTO 9991
C DT MUST BE TOO LONG TO BE ACURATE !
999 CONTINUE
 NWRONG=I
 WRITE (6,9990)
9990 FORMAT(//,' *** I AM AFRAID THAT THE TIME INTERVAL IS NOT
 1ADEQUATE !!',/,' TRY A SHORTER DT !')
 WRITE (6,8544) DT
 WRITE (6,802)
 READ (5,803) ANSWER5
 IF (ANSWER5.EQ.'Y') THEN
 WRITE (6,750)
 WRITE (6,800) (TIME(I),X(I),Y(I),I=1,NWRONG)
 ENDIF
C
9991 CONTINUE
 WRITE (6,845)
845 FORMAT(' DO YOU LIKE TO CHANGE THE TIME INTERVAL DT ONLY AND
 1',/,'$COMPUTE THE WHOLE SET OF DATA AGAIN ?[Y/N] : ')
 READ (5,803) ANSWER5
 IF (ANSWER5.EQ.'Y') THEN
 WRITE (6,104)
 READ (5,105) DT
 WRITE (6,8544) DT
8544  FORMAT (' DT IS : ' ,E12.5)
 GOTO 1030
 ENDIF
 WRITE (6,849) K2,K4,K5,K7
849 FORMAT(/' K2 =',E12.5/' K4 =',E12.5/' K5=',E12.5/' K7 =',E12.5)
 WRITE (6,850)
850 FORMAT(/,'$DO YOU LIKE TO TRY THE OTHER SET OF K2,K4,
 1 K5, AND K7  ?[Y/N] : ')
 READ (5,803) ANSWER5
 IF (ANSWER5.EQ.'Y') GOTO 2
```

```
 WRITE (6,900)
900 FORMAT(/,'$DO YOU WANT TO START THE COMPUTATION AGAIN ?
        1 [Y/N] : ')
 READ (5,803) ANSWER5
803 FORMAT(A1)
 IF (ANSWER5.EQ.'Y') GOTO 1
 STOP
 END
```

References

1. (a) J. N. Demas and C. M. Flynn, Jr., Anal. Chem. 48, 353 (1976).
(b) J. N. Demas, J. Chem. Ed. 53, 657 (1976).

2. K. Kalyanasundaram, J. Kiwi, and M. Grätzel, Helv. Chim. Acta. 61, 2720 (1978).

3. H. Laitinen and W. Harris, "Chemical Analysis", McGraw-Hill 1975.

4. P. Keller, A. Moradpour, E. Amouyal, and H. B. Kagan, Nouv. J. Chim. 4, 377 (1980).

5. S.-F. Chan, M. Chou, C. Creutz, T. Matsubara, and N. Sutin, J. Am. Chem. Soc. 103, 369 (1981).

CHAPTER IV

PHOTO-INDUCED ELECTRON-TRANSFER REACTIONS IN HETEROGENEOUS MEDIA

While studying photochemistry in homogeneous solutions, one appreciates that if solar energy is to be conserved efficiently via electron-transfer reactions in an artificial photosynthetic system, the reactants used must satisfy the following requirements:

(a) The sensitizer should be reasonably stable and have strong absorptivity within the solar spectrum. Its excited state should be energetic enough to carry out the desired reactions.

(b) An appropriate excited-state quencher should be added to intercept the intrinsically decaying pathways, and the products of this quenching reaction should retain most of the light energy gained. In other words, thermal energy released during the quenching reaction must be minimized.

(c) The photoproducts should effectively escape from the solvent cage where they encounter each other, and their subsequent recombination reaction should be retarded.

(d) Catalysts, which interact with those unstable, energetic photoproducts to provide more stable ones, should be carefully designed to maximize the rates of desired reactions.

Apparently, the performance of each component critically influences the overall yield of an artificial photosynthetic system, as is illustrated in Figure 1 using solar decomposition of water as an example.

It is clear that Figure 1 shows only those productive reactions which lead to water splitting. Actually, when a photochemical reaction is carried out in a homogeneous solution, several back reactions and side reactions can take place simultaneously so as to severely hamper

Figure 1. General scheme for water photodecomposition. S represents a sensitizer, A an electron acceptor, D an electron donor, and C_1, C_2 are catalysts for water splitting.
Two possible mechanisms are shown. One starts from an oxidative quenching, the other from a reductive quenching.

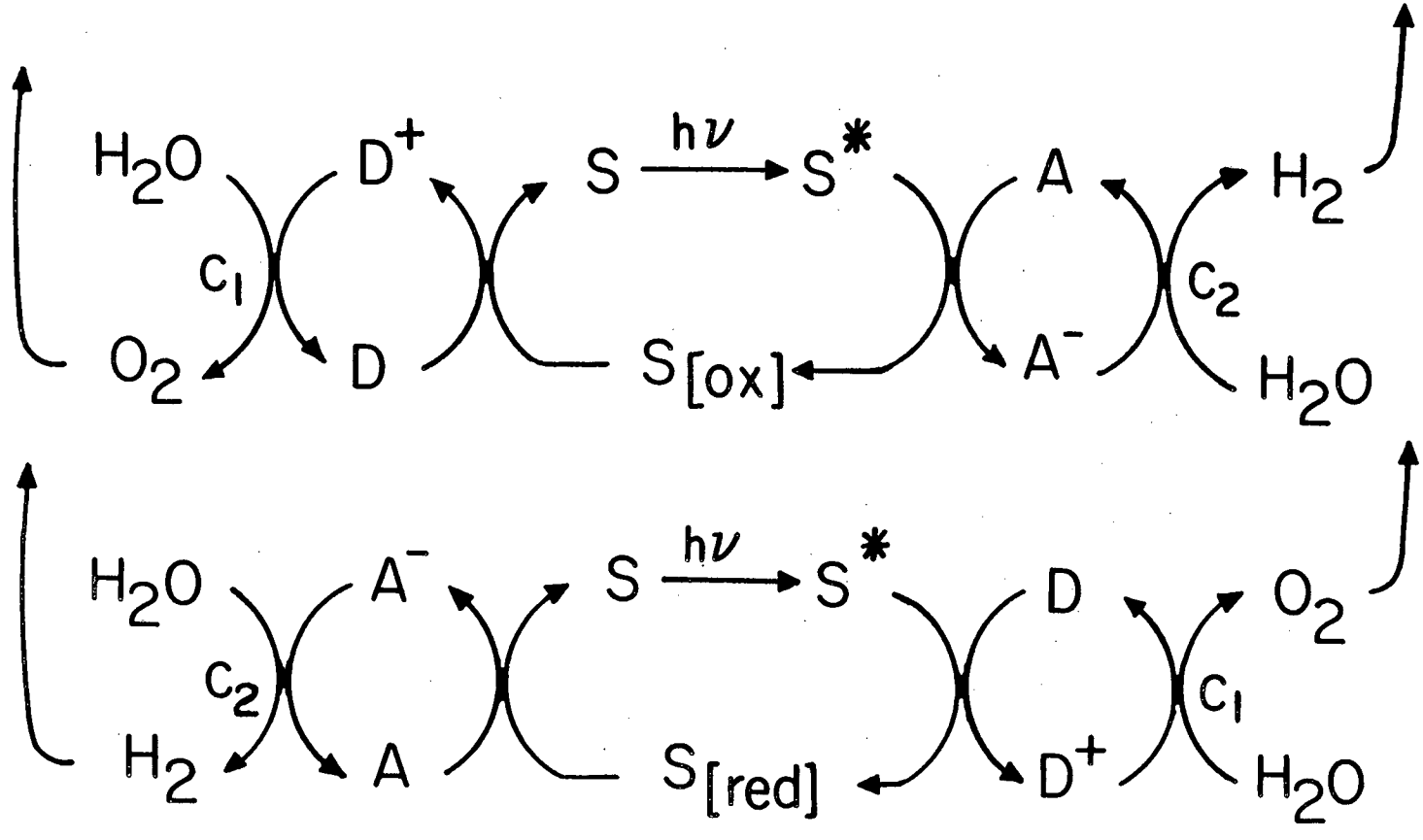
H2O
D+
S
hν
S*
A
H2
C1
C2
O2
D
S[ox]
A−
H2O
H2O
A−
S
hν
S*
D
O2
C2
C1
H2
A
S[red]
D+
H2O

XBL 819-4987

the completion of a desired process. For instance, unless there exists a high energy barrier, most photo-products will recombine exothermally. Also, most of the intermediates created in electron-transfer reactions either react without selectivity or decompose by reacting with solvent. In order to have better control of the reaction pathway, one frequently resorts to heterogeneous solutions which generally consist of two sub-phases and a charged interface. In these solutions, one or more of the reactants and products can be manipulated to make selective interactions possible. In fact, photo-induced electron-transfer reactions in many such solutions have been explored, e.g. micelles, reverse micelles, microemulsions, and polyelectrolytes [1]. In addition to the concentration effect, these heterogeneous solutions have also been found to influence the course of reaction through the electrostatic interactions between reactants and the surface charge, if any, on dispersed colloids or on polymers. Following the initial charge separation, charged radicals or ions thermalize in the electric field according to the Boltzmann law. If reactants are properly chosen, back reaction can be considerably slowed down by this kind of spatial distribution.

In this chapter, photochemical reactions with ionic reactants in heterogeneous media with colloidal silica or the polyelectrolyte polyacrylate will be studied. The effects of the charged interface on fluorescence quenching, charge separation, and product recombination are individually examined, and ways to optimize the conversion of solar energy into chemical energy will be suggested.

Experimental

(1) Materials

Colloidal silica dispersion with a trade name of Nalcoag was from Nalco (Oak Brook, Illinois). Particle size ranging from 4 nm to 1 micron was available. Nalcoag 1115 with 15%, 40 Å colloidal silica in aqueous solution was chosen for all experiments.

N,N'-dipropyl-4,4'-bipyridium sulfonate (PVS°) was synthesized from 4,4'-bipyridine and 1,3-propane sultone by Ford in our group [2].

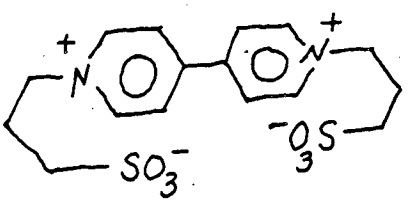

Zinc meso-tetra(4-pyridyl) porphyrin ($ZnTPyP^{4+}$) was synthesized by first refluxing zinc acetate and tetrapyridylporphyrin (Strem product) in dimethylformamide. Methylation was achieved by stirring the precipitated product in an excess of methyl iodide overnight [3]. Zinc tetra(N-methyl-4-pyridyl)porphyrin chloride was obtained by exchanging its iodide complex in AG 2-X8 anion exchange resin (chloride form). Its perchlorate and tetrafluoroborate salts were obtained by precipitating the iodide salt with silver perchlorate or $AgBF_4$ and then recrystallizing from saturated $NaClO_4$ or $NaBF_4$ aqueous solutions.

All other chemicals have been described in the previous chapter.

(2) Experimental procedures

Typically, 20 μl concentrated 15% silica solution was added into a 3 ml solution containing all other necessary chemicals. The pH of the solution was then measured by a Corning pH meter and was adjusted by adding concentrated NaOH or HCl.

Spectra of oxidized compounds were taken using a thin-layer, optically transparent electrode (OTE) under potentiostatic condition. Details of OTE have been described in Chapter 2. The excited-state lifetime of $Ru(bpy)_3^{2+}$ was measured using a nanosecond spectral source. The time profile of fluorescence intensity was recorded on a storage oscilloscope and analyzed by the method described in Chapter 2.

Flash photolysis studies as well as the recording of absorption and fluorescence spectra were carried out in the same way as described in the previous chapter. In continuous photolysis experiments, a 450 W xenon lamp was used, and the excitation light was limited to between 400 and 550 nm by a 10-cm $CuSO_4$ solution (100 g/l), a Corning 5-57 filter, and a UV filter with cutoff at 400 nm.

(3) Chemical actinometry

Actinometry with Reinecke salt ($K[Cr(NH_3)_2(NCS)_4]$) was chosen for the measurement of light intensity [4]. 0.15 g of Reinecke salt was dissolved in 10 ml deionized water, and the solution (0.045M) was filtered right before use. Its pH was then adjusted to about 3.5 by adding H_2SO_4 against a pH paper. Since this salt underwent slow but noticeable thermal dissociation, a portion of the solution was kept in the dark to be used as a reference. After a certain period of illumination, an aliquot of 0.1 ml was withdrawn from both the illuminated and the dark solutions and each added into a 2.9 ml solution of 0.1 M $Fe(NO_3)_3$ in 0.5 M H_2SO_4. The absorption spectrum was taken using the dark solution as the reference. Throughout the illumination, stirring must be provided to prevent any excess accumulation of products in the illuminated area. With the present 450 W

xenon lamp, the total flux of photons impinging on the solution was measured to be 2.9×10^{-7} einstein/s and the light intensity was about 2.4×10^{-7} einstein/$cm^2 \cdot$sec. The spectral data provided by the lamp manufacturer aided in assigning the number of photons in every 10 nm interval. Finally, the number of photons actually absorbed by the sensitizer could thus be calculated from its own absorption spectrum combined with the above two quantities.

Results and Discussion

PART A. Photochemistry in colloidal silica

Since colloidal silica has not been used frequently in the past, its characteristics will be discussed first. This brief shall help understand the role it plays in the subsequent photochemical studies.

(1) Characteristics of colloidal silica

Nalco uses an ion exchange method in preparing colloidal silica, whereby silicic acid is fed at a controlled rate into a sodium silicate solution. Growth and concentration are accomplished simultaneously. Details of this and other methods of colloidal silica manufacturing can be found in Ralph Iler's "The Chemistry of Silica" [5]. The stability of these solutions can be explained as a function of Brownian movement and electrical properties. While the Brownian motion of these 40 Å particles helps keep them from settling out, it also affords an opportunity for the particles to collide and agglomerate. It is their surface charges which prevent the agglomeration from occurring. At pH above 7, some surface silanol groups become ionized and, thus, colloidal silica particles are charged. This negatively charged surface attracts positive ions and repels those ions of the same charge. As a result, an electrical double layer responsible for the stability of the colloidal dispersion is induced. Figure 2a displays the stability of silica particles as a function of pH [6]. At lower pH, particles are metastable because there are fewer hydroxyl ions present to catalyze the reaction which leads to gel formation, as shown in Figure 2b.

In this study, I am particularly interested in utilizing the high surface potential of colloidal silica in electron-transfer

Figure 2. (a) Effect of pH on the gelling of colloidal silica.

(b) Formation of siloxane bonds between two colloids. Hydroxide ion is a catalyst for this gelling process.

(a)

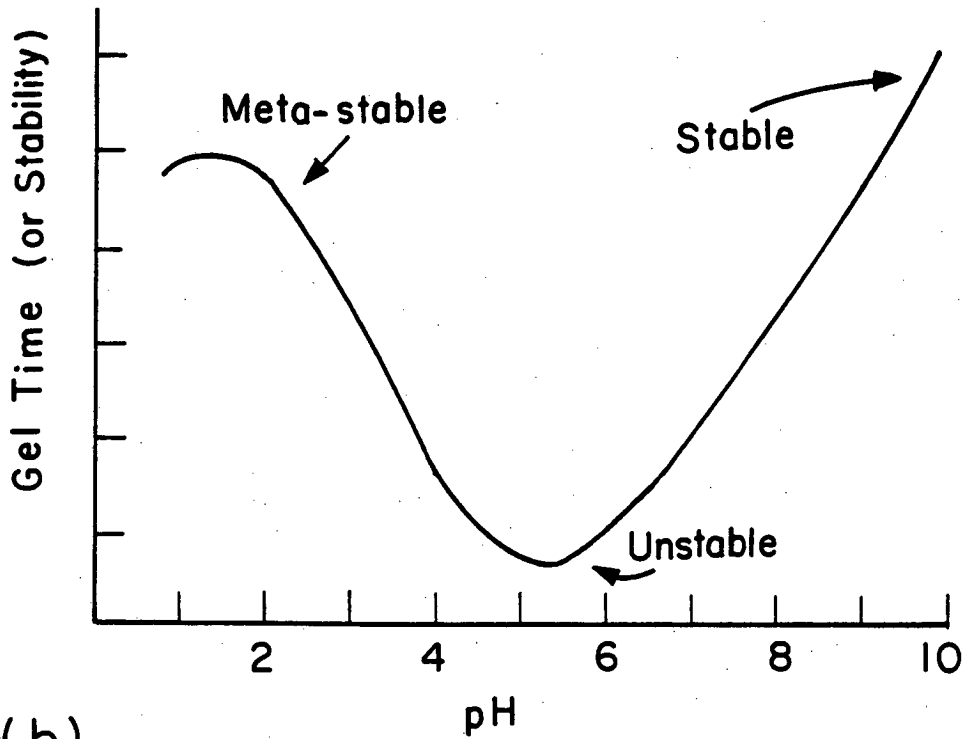

(b)

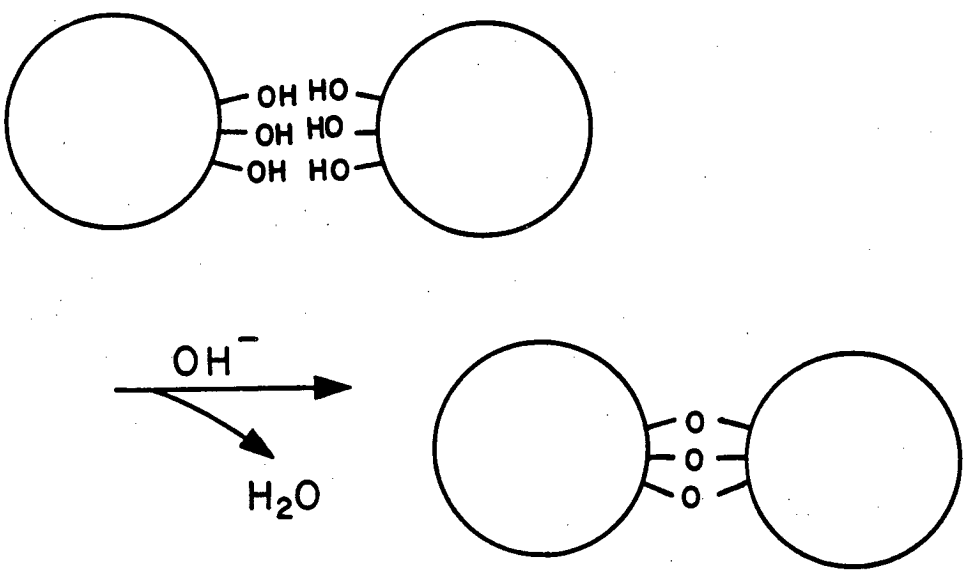

XBL 819-4986

reactions to separate photoproducts by virtue of coulombic interactions. Since the number of ionized sites on a 40 Å silica particle has been determined to be ~60 [7], the surface potential can be estimated by the Gouy-Chapmann relation [8],

$$\sigma_s = 2.66 \times 10^{-4} [DRT]^{1/2} C^{1/2} \sinh\left(\frac{F\psi_s}{2RT}\right) \qquad (1)$$

where σ_s is the surface charge density ($C \cdot m^{-2}$), ψ_s the surface potential (volt), D the dielectric constant, R the universal gas constant (8.3 $J \cdot mole^{-1} \cdot deg^{-1}$), F the Faraday constant (96500 Coulombs·$mole^{-1}$), T the absolute temperature (°K), and C the concentration of 1-1 electrolyte. ψ_s is calculated to be about -170 mV at a salt concentration of 0.01 M. This number compares favorably with those found in micelles of similar size [9]. In micellar aggregates, because the binding force between surfactants consists of weak hydrophobic interactions, most of the charged head groups must bind counter ions closely in the Stern layer so that the repulsive interaction between head groups can be largely diminished. Thus, the number of ionized sites found in micellar aggregates is usually small, e.g., only 1/6 of the head groups. On the contrary, the binding force in colloidal silica is the much stronger covalent force, and the number of the apparent ionized sites is almost equal to the total surface silanol groups.

In order to show the existence of such high surface potential and demonstrate that the back reaction may be retarded by the charge interface, positively charged $Ru(bpy)_3^{2+}$ or porphyrins are chosen as the sensitizer and a neutral propylviologen sulfonate as the electron acceptor. Before we continue to discuss their photochemistry in colloidal silica, the redox properties of these compounds should be

examined first.

(2) Electrochemistry

The reduction potential of propylviologen sulfonate was measured with a hanging mercury electrode in unbuffered aqueous solution with 1 M KCl. From the cyclic voltammogram shown in Figure 3a, the half-wave potential, $E_{1/2}$, was calculated to be -0.652 V vs SCE or -0.410 vs NHE. $E_{1/2}$ for the second reduction was at -0.751 V vs NHE. The cyclic voltammogram of methyl viologen was also recorded and shown in Figure 3b. $E_{1/2}$ of $MV^{2+}/MV^{+\cdot}$ was measured to be -0.44 V vs NHE, which was exactly the same as that reported by Krasnovskii and Brin [10]. Pre-waves were noted and were attributed to some adsorbed viologen on the mercury electrode. The introduction of two sulfonate groups shifts the reduction potential only slightly upwards.

The optical spectrum of $PVS^{\cdot-}$ radical was taken by reducing a freshly prepared PVS° of 5 x 10^{-5} M with 20-50 μl of 0.1 M $Na_2S_2O_4$ in 0.1 M Tris(hydroxymethyl)aminomethane buffered at pH 8.06 (Figure 4). The extinction coefficient at 602 nm, ε_{max}, was measured to be 1.41 x 10^4 $M^{-1}cm^{-1}$. Similarly, the ε_{max} of $MV^{+\cdot}$ at 602 nm was measured in an aqueous solution containing the same buffer to be 1.18 ± 0.04 x 10^4 $M^{-1}cm^{-1}$, which was the same as that reported by Trudinger [11]. Care was taken not to irreversibly reduce viologen further to a colorless compound, MV°.

(3) Excited-state lifetime measurements

In the presence of 3.8 x 10^{-5} M silica particles, the excited-state lifetime of $Ru(bpy)_3^{2+}$ was found to increase both in a de-aerated solution and in an air-saturated solution. They are 0.71 and 0.49 μs,

Figure 3. (a) Upper curve: Cyclic voltammogram of PVS° in aqueous solution with 1 M KCl as the supporting electrolyte (scan rate 100 mV/s).

WE: hanging mercury electrode

CE: Pt wire

RE: SCE

Lower curve was taken under the same conditions as the upper curve except it was driven toward slightly lower potential so that the second reduction can be observed.

(b) Cyclic voltammogram of MV^{2+}.

Experimental conditons are the same as that in figure 3(a).

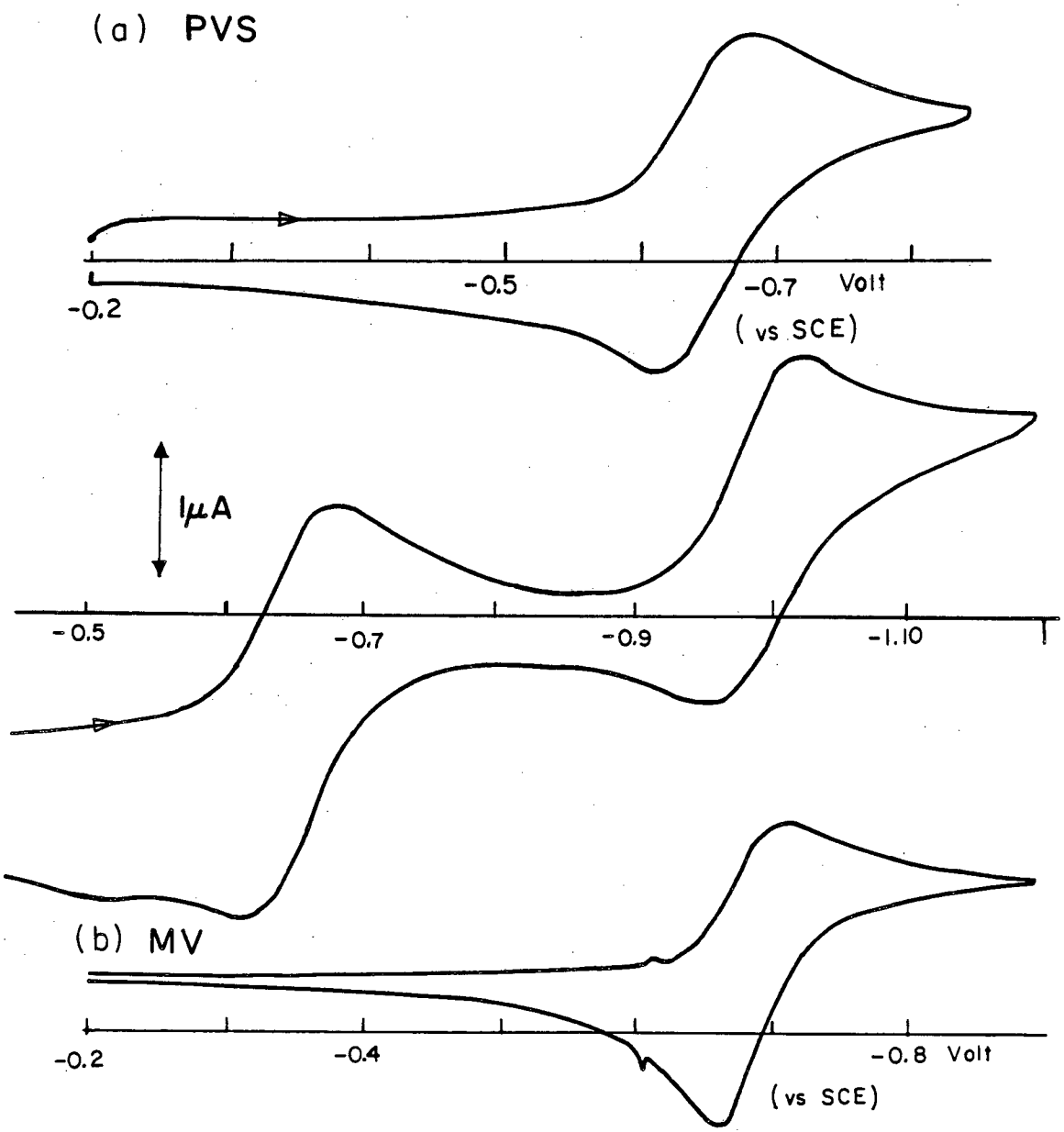

XBL 819-4985

Figure 4. Absorption spectrum of $PVS^{\cdot-}$ radical.
[PVS°] = 5×10^{-5} M in 0.1 M of Tris buffer at pH 8.06.
Reducing agent was 0.1 M $Na_2S_2O_4$.

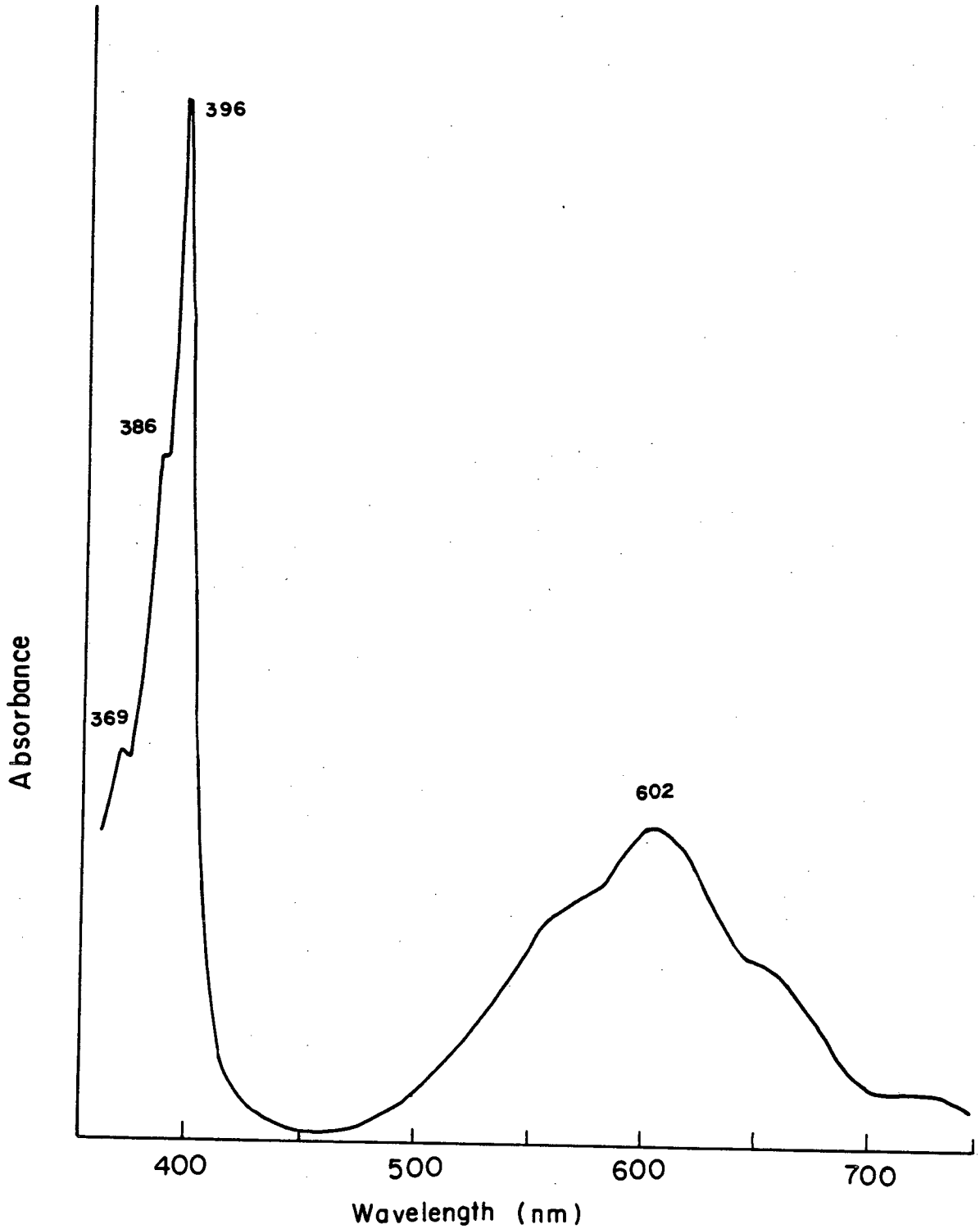

XBL 819-4984

respectively, in the presence of silica particles, compared to 0.61 and 0.39 μs found in my previous experiments in homogeneous solutions. By increasing the concentration of silica particles to 1.1×10^{-4} M, the lifetime τ in an aerated solution was further lengthened to 0.52 μs. But, adding 0.1 M NaCl into the solution containing 3.8×10^{-5} M colloidal silica decreased τ to 0.42 μs in aerated solution. One cannot attribute the variation of τ to differences in ionic strength or pH, because τ is almost the same in a 0.5 M ammonium acetate solution as in a pH 12 aqueous solution. Although it should be possible to tell whether there are two different values for the excited-state lifetime by analyzing the decay curves, the bad condition of our fluorescence detecting system prevented us from doing so. Since τ is the inverse of the sum of k_{nr}, k_r, and $\sum_i k_q^i[Q_i]$, one of these factors must decrease in the presence of silica particles to account for the results obtained.

In addition to these excited-state lifetime measurements, I also compared the fluorescent intensities with and without colloidal silica under the steady-state condition. The emission intensity was found to increase in parallel to the trend observed above in silica solutions, as shown in Figure 5. Even though there were no discernible differences in the wavelength dependence of the absorption and fluorescence spectra, these experiments made me speculate that k_{nr} might decrease in silica solution due to the adsorption of $Ru(bpy)_3^{2+}$ on silica particles. In the future, constructing a new system using a simple ns N_2 pulse laser for fluorescence lifetime measurement [12] should help resolving this point.

Figure 5. Variation of fluorescent intensity at different concentrations of silica particles.

All three solutions have 3.3×10^{-5} M of $Ru(bpy)_3^{2+}$.

A. [silica particle] = 0 M

B. [silica particle] = 3.8×10^{-5} M

C. [silica particle] = 1.1×10^{-4} M

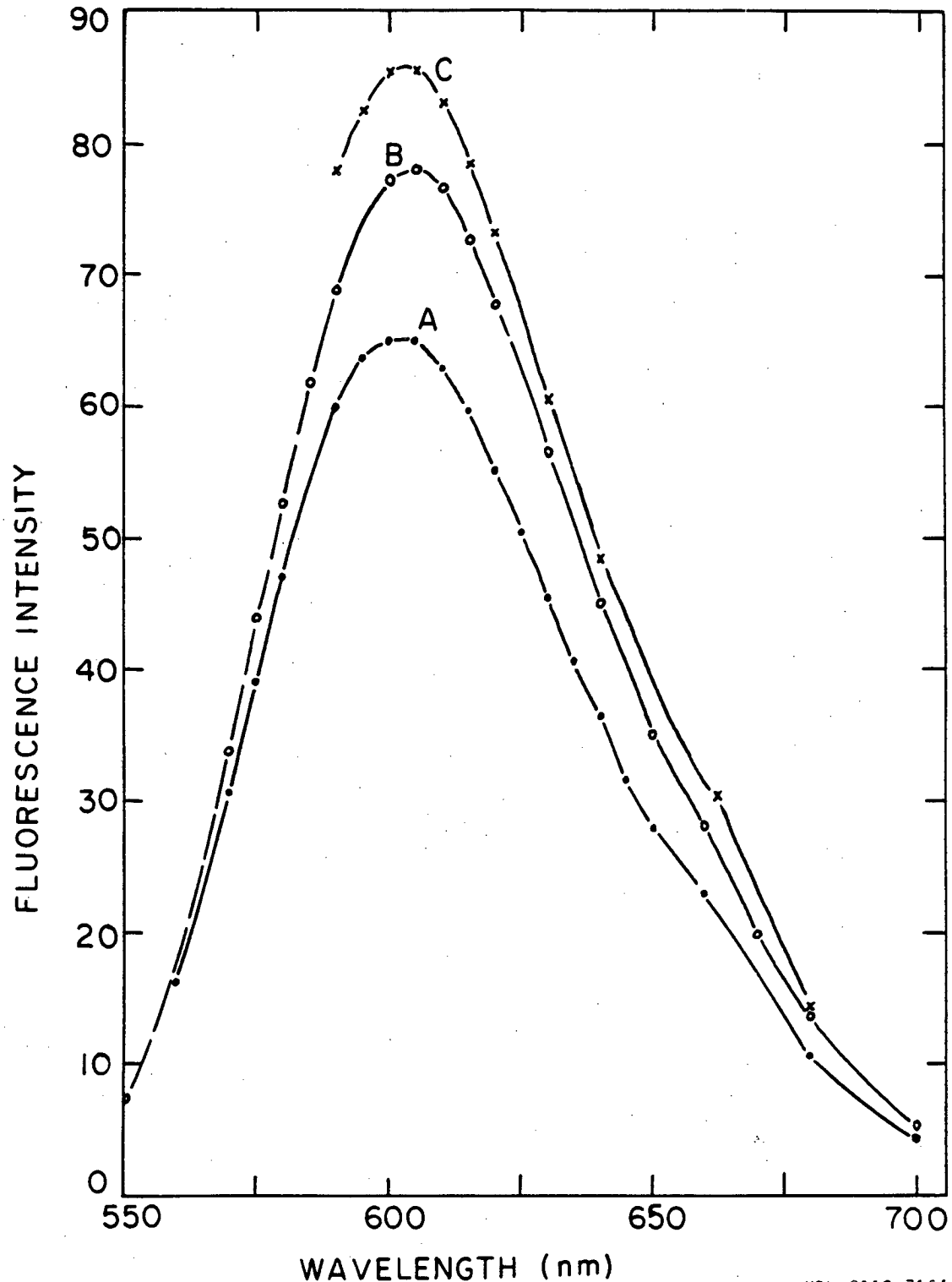

XBL 8110-7164

(4) Fluorescence quenching studies

A. With methyl viologen as the quencher

In order to illustrate the concentration effect caused by the electrostatic potential near the surface of silica particles, the excited-state quenching of $Ru(bpy)_3^{2+}$ by MV^{2+} was studied.

$$Ru(bpy)_3^{2+} + MV^{2+} \xrightarrow{k_q} Ru(bpy)_3^{3+} + MV^{+\cdot} \qquad (2)$$

The quenching constant k_q in a homogeneous solution was found to be $8.1 \times 10^8\ M^{-1}s^{-1}$ in the previous chapter. Since both reactants are positively charged, one would expect that the quenching rate constant should be increased by increasing the ionic strength of the media. This is attributed to the decrease of coulombic repulsive force between the reactants. Recently, I have repeated this reaction again very carefully and the results are shown in Figures 6 and 7. Indeed, k_q increases from $5 \times 10^8\ M^{-1}s^{-1}$ at low ionic strength to $1.3 \times 10^9\ M^{-1}s^{-1}$ in the presence of 0.5 M ammonium acetate.

In the presence of 3.8×10^{-5} M silica particles (or 2.5 mM in terms of surface sites), the Stern-Volmer plot (Figure 8) was drastically modified as compared to that in a homogeneous solution. With over 1 mM MV^{2+}, colloidal silica started to gel as the result of a decrease in surface potential and an increase in gelling process. This was expected since only 2.5 mM surface sites were available in the solution and each MV^{2+} might associate with two surface sites. However, to account for the peculiar shape of the curve found in Figure 8, one must include the process of 'quenching reversal' into the quenching mechanism [14]. At a low concentration of MV^{2+}, the local concentrations of reactants near the surface of a particle are very high because they are attracted and confined onto small particles.

Figure 6. Stern-Volmer plots of the quenching of excited $Ru(bpy)_3^{2+}$ by MV^{2+} in homogeneous aqueous solutions. $[Ru(bpy)_3^{2+}] = 3.3 \times 10^{-5}$ M in

(A) 0.5 M of ammonium acetate

(B) 0.4 M of ammonium acetate

(C) 0.25 M of ammonium acetate

(D) without added ammonium acetate.

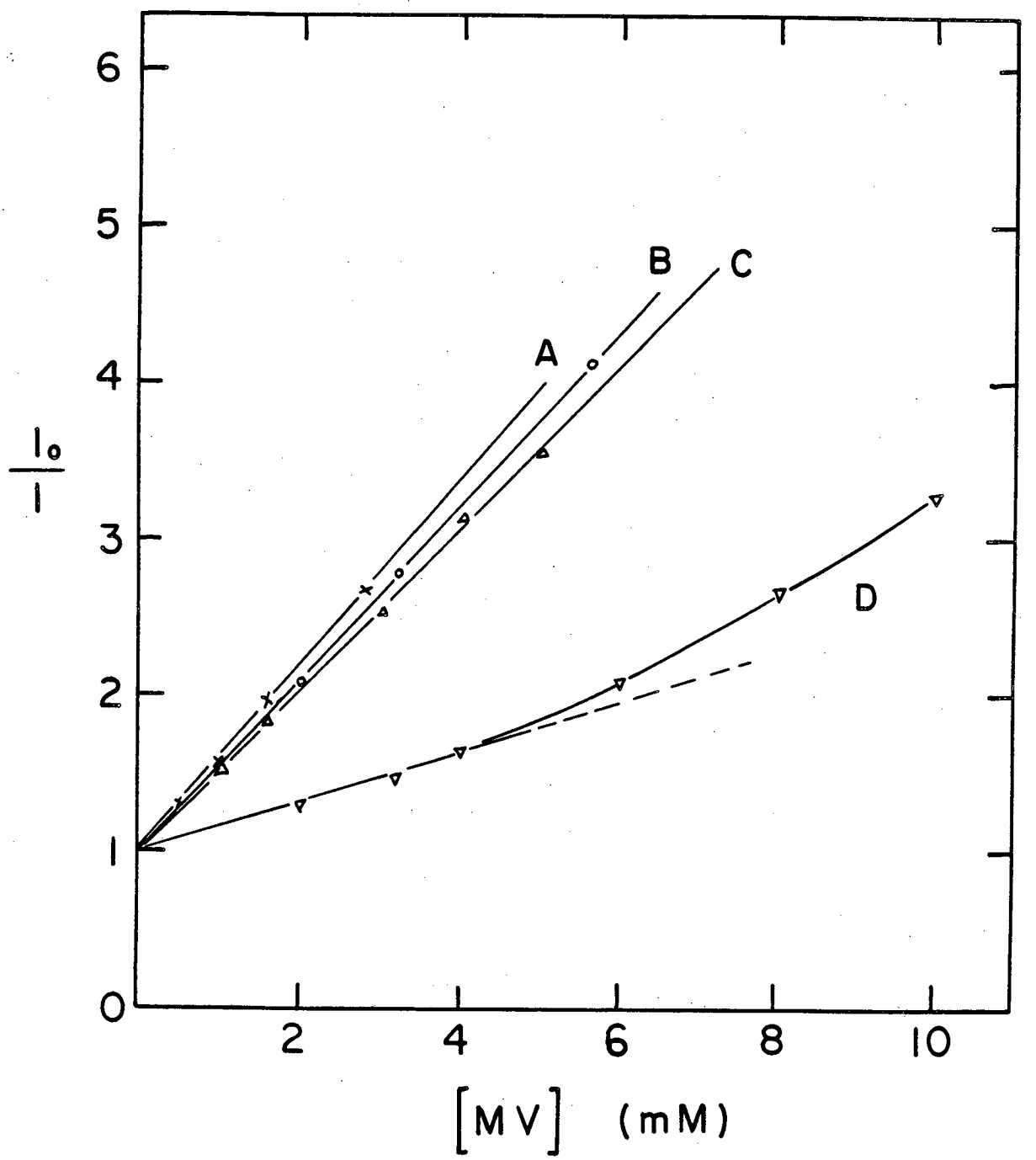

XBL 8110-7082

Figure 7. Stern-Volmer constant as a function of salt concentration.

$[Ru(bpy)_3^{2+}] = 3.3 \times 10^{-5}$ M

$k_{sv} = k_q \tau$

$= k_q \times (0.4 \times 10^{-6})$

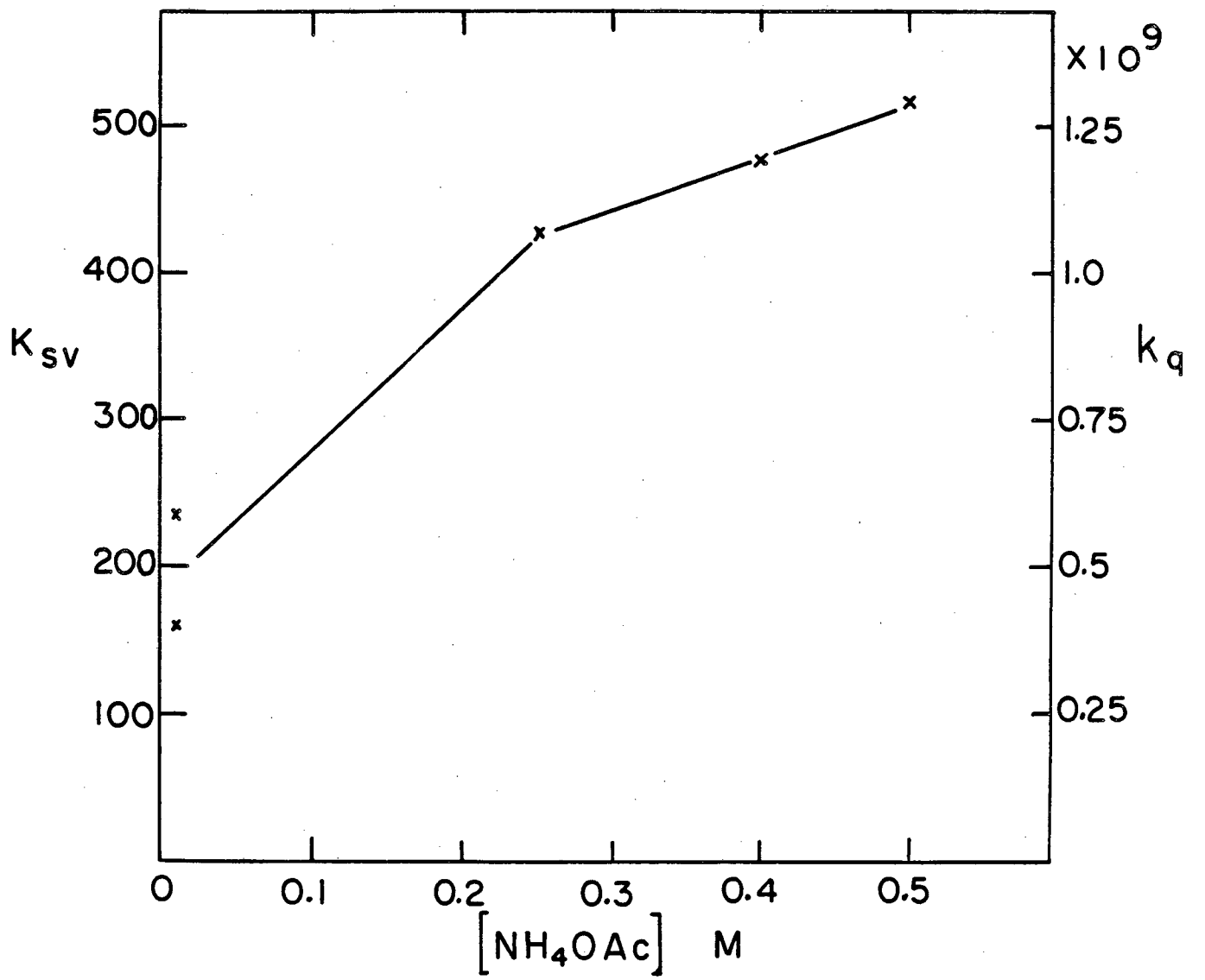

XBL 8110-7083

Figure 8. Stern-Volmer plots of the quenching of excited $Ru(bpy)_3^{2+}$ by MV^{2+} in the presence of 3.8×10^{-5} M of silica particles (pH=9.8). $[Ru(bpy)_3^{2+}] = 3.4 \times 10^{-5}$ M in

(A) 0. M of NaCl

(B) 0.02 M of NaCl

(C) 0.1 M of NaCl

(D) 0.5 M of NaCl

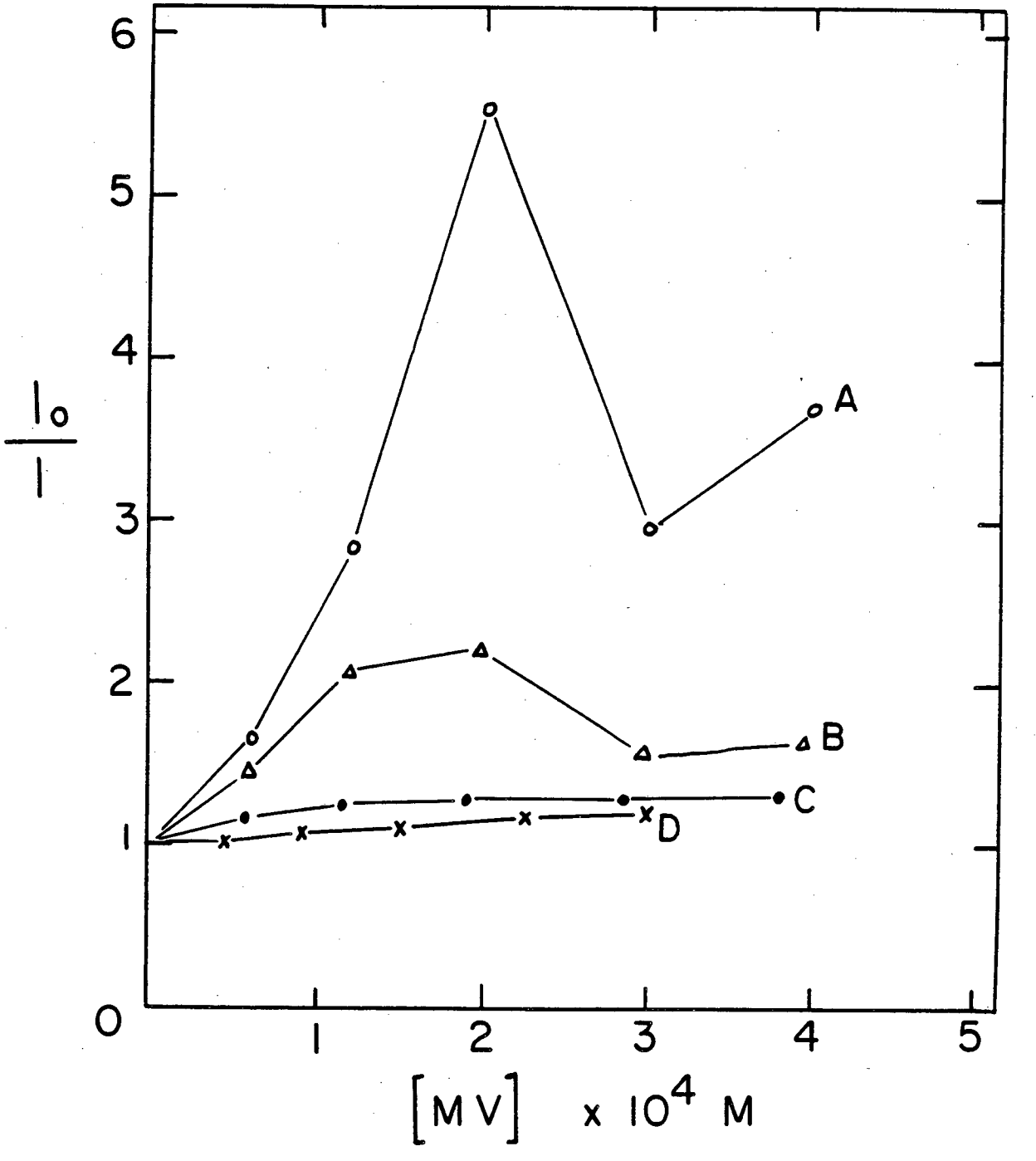

XBL 8110-7081

The apparent quenching constant k_q was estimated to be 4.7×10^{10} $M^{-1}s^{-1}$, which was about 100 times higher than that in homogeneous solutions. As $[MV^{2+}]$ increased, more and more $Ru(bpy)_3^{2+}$ were displaced from the silica surface to the bulk solution and then the quenching took place mostly in the bulk instead of near the interface. Upon further increase of $[MV^{2+}]$, the curve in Stern-Volmer plot went downward first and then curved up again and behaved as in a normal quenching process found in homogeneous solutions (Figure 8A). Comparing the hundredfold increase of quenching rate constant with the small percentage of volume occupied by the particles in the solution (ca. 1/2000 assuming the density of colloidal silical was 2.2 gram/cc), one may qualitatively conclude that at a low $[MV^{2+}]$ most of these two reactants are confined within 54 Å from the center of a silica particle, or 34 Å from the surface if MV^{2+} is not adsorbed on the surface. The radius of this reaction zone is comparable to the thickness of the Stern layer for such charged particles (~22 Å estimated by Gouy-Chapman treatment) [8a]. Certainly, one may as well attribute the difference between 1/100 (apparent quenching constant/ quenching constant in a homogeneous solution) and 1/2000 (volume occupied by colloidal silica/total volume) to a decrease in the mobility of those ions adsorbed on silica surface. We have a good reason to suspect that $Ru(bpy)_3^{2+}$ is bound on the surface since the presence of colloidal silica actually lengthens its fluorescent lifetime (vide supra). In addition, the gelling of particles in only 1 mM MV^{2+} suggests that MV^{2+} is also bound on the surface. Shown also in Figure 8 is the effect of the salt concentrations on quenching constant. The apparent quenching constant reverts to that

found in a homogeneous solution by increasing the ionic strength to swamp the reactants out of the surface and possibly to decrease the surface potential. With 0.1 M NaCl, k_q was measured to be 1.7×10^9 $M^{-1}s^{-1}$. In the future, a calculation of k_q for two dimensional quenching process on the surface of silica particles should be carried out. The results can be compared with the experimental data obtained from the fluorescence quenching studies at different concentrations of MV^{2+} and on various sizes of silica particles with a nanosecond laser photolysis setup.

B. With propylviologen sulfonate (PVS°) as the quencher

To utilize the property of highly negative surface potential of colloidal silica to retard the undesired back reactions, PVS° was chosen because of its zero net charge and its high solubility in water. Once PVS° is reduced, it bears a negative charge and will be expelled away from the area where $Ru(bpy)_3^{3+}$ resides. This allows both photoproducts to interact at leisure with catalysts.

Figure 9b and 9a show the results of quenching experiments with and without 3.8×10^{-5} M silica particles. k_q was calculated as $1.2 \pm 0.1 \times 10^9$ $M^{-1}s^{-1}$ in the presence of colloidal silica and 1.4×10^9 $M^{-1}s^{-1}$ in homogeneous solutions without any added salt. Adding 0.25 M ammonium acetate caused only a slight increase in k_q to 1.5×10^9 $M^{-1}s^{-1}$ in homogeneous solutions. As compared to methyl viologen, PVS° may be regarded as a neutral acceptor in electron-transfer reactions.

(5) Flash photolysis studies in solutions containing colloidal silica

With PVS° as the electron acceptor, several flash photolysis

Figure 9. (A) Quenching constants of excited $Ru(bpy)_3^{2+}$ by PVS° as a function of added salt, ammonium acetate. $[Ru(bpy)_3^{2+}] = 3.3 \times 10^{-5}$ M

(B) Stern-Volmer plot of the quenching of excited $Ru(bpy)_3^{2+}$ by PVS° in the presence of 3.8×10^{-5} M of silica particles (pH=9.8). $[Ru(bpy)_3^{2+}] = 3.3 \times 10^{-5}$ M

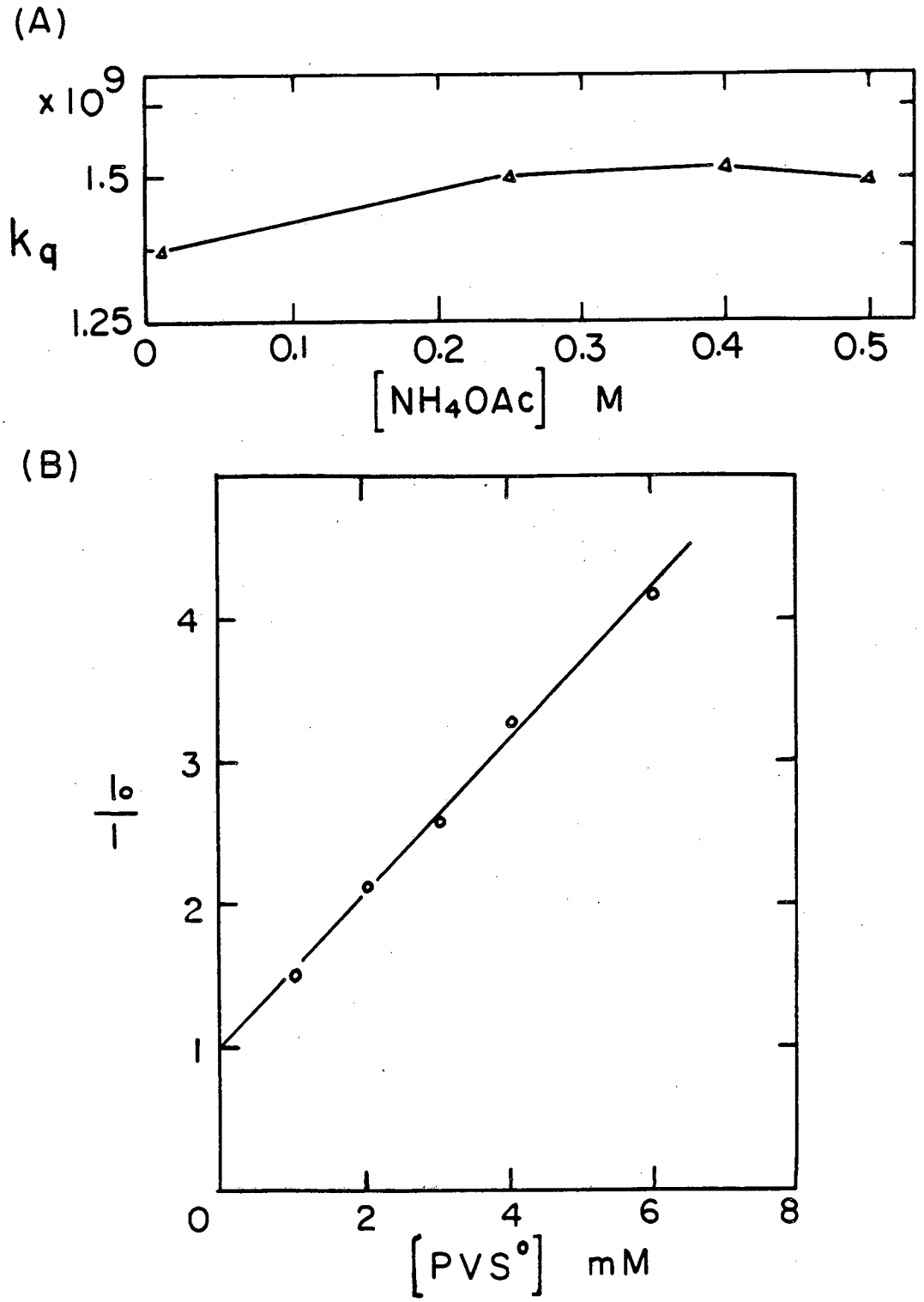

XBL 8110-7080

experiments were carried out in solutions with and without silica particles. Figure 10 summarizes the results. In a homogeneous solution, the back reaction

$$Ru(bpy)_3^{3+} + PVS^{\cdot-} \xrightarrow{k_b} Ru(bpy)_3^{2+} + PVS^{\circ} \qquad (3)$$

followed a second-order kinetics, and the rate constant k_b was calculated to be 7.9×10^9 $M^{-1}s^{-1}$ (Figure 10A). This is ten times faster than that of $Ru(bpy)_3^{3+}$ and $MV^{+\cdot}$. Obviously, the back reaction is greatly facilitated by the electrostatic interaction between the oppositely charged reactants. However, in the presence of 3.8×10^{-5} M silica particles (pH 9.8), the undesired back reaction was drastically retarded (Figure 10B). k_b was estimated to be 5.7×10^7 $M^{-1}s^{-1}$. It is reasonable to use a second-order kinetics for all the calculations of the rate constant between $Ru(bpy)_3^{3+}$ and $PVS^{\cdot-}$ in heterogeneous media in this chapter as long as the number of ruthenium complex per particle is less than one and the mean diffusion distance ($\sqrt{2Dt} = \bar{x}$) is much larger than the average center-to-center distance between silica particles. Experimentally, it was found that most of the $PVS^{\cdot-}$ survived over 1 ms. The mean diffusion distance in 1 ms is two orders of magnitude larger than the average distance between particles in the experimental conditions. In any case, whether the treatment of such a reaction to be second order is valid can be easily justified by using the other detector which is specifically designed to record slow reactions (see Chapter 2). According to the result from the fluorescence lifetime measurements and quenching studies with MV^{2+}, we favor that almost all $Ru(bpy)_3^{2+}$ are adsorbed on the surface. (The spatial distribution should obey the Boltzman distribution, $n_+ = n \exp(-2e\Psi/kT)$) Thus, it is reasonable to further

Figure 10. Transient absorption changes of $PVS^{\bar{\cdot}}$ followed at 602 nm. Arrow indicates the laser flash.

$[Ru(bpy)_3^{2+}] = 3.6 \times 10^{-5}$ M

$[PVS^{\circ}] = 4 \times 10^{-3}$ M

(A) In a homogeneous aqueous solution, pH = 9.8.

(B) In a 3.8×10^{-5} M (or 0.2%) silica colloid, pH = 9.8.

(C) In a 3.8×10^{-5} M silica colloid, pH = 9.8 with added 0.1 M NaCl.

(D) In a 3.8×10^{-5} M silica colloid at pH 4.5.

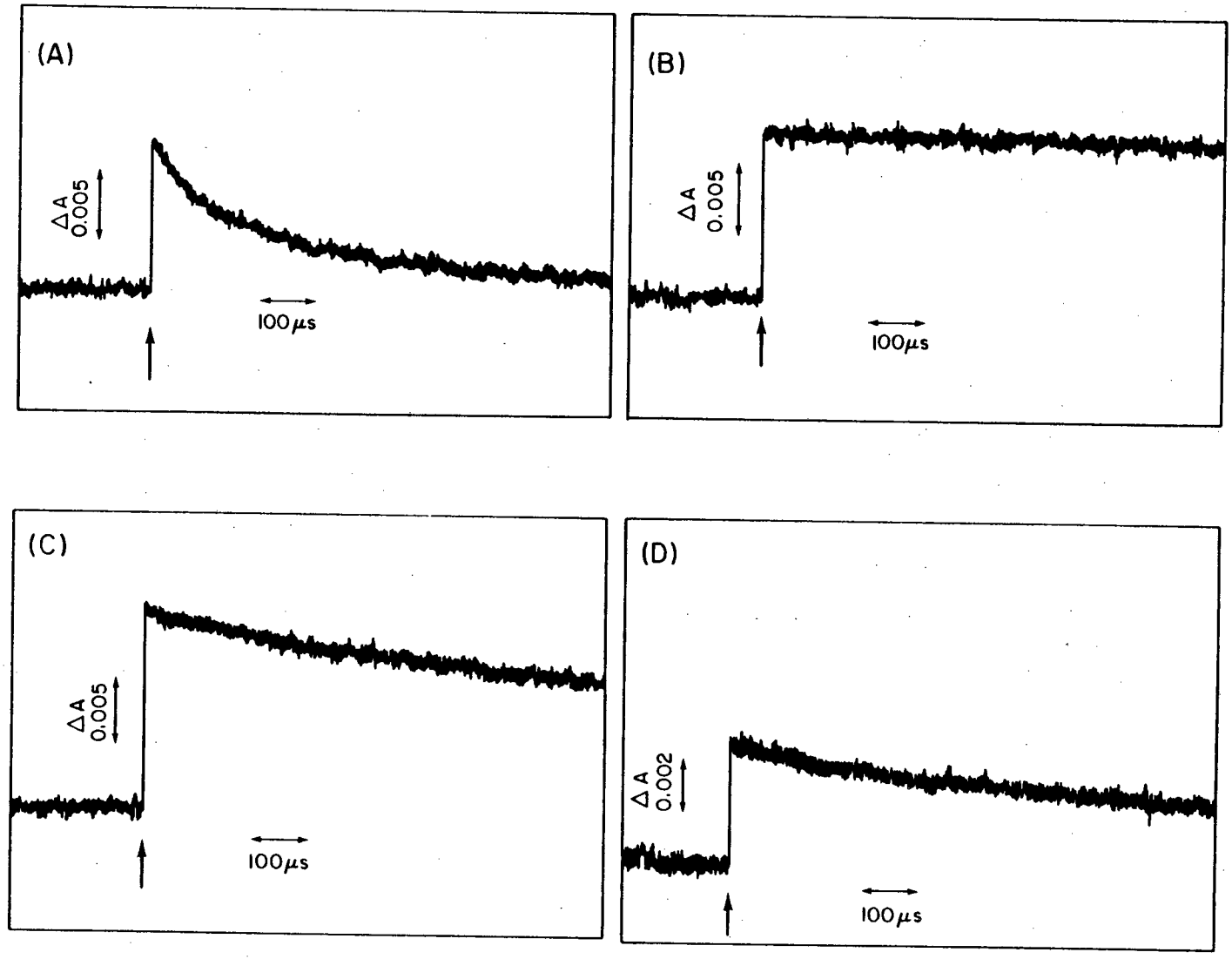

XBL 814-4561A

assume that $Ru(bpy)_3^{3+}$ is tightly bound on the surface and the slowness of the back reaction is due to the inability of PVS^- to surmount the potential barrier.

Similar experiments were also carried out with $ZnTMePyP^{4+}$ as the sensitizer. The decay curves were monitored at both 602 and 650 nm. Since the actual extinction coefficient of this porphyrin in aqueous solution is not yet available (see part B(1)), we can only approximate the rate constants by using the data of $ZnTPP^{+\cdot}$ for $ZnTMePyP^{5+}$. They are 4.5×10^7 $M^{-1}s^{-1}$ and (2.1-8.4) $\times 10^9$ $M^{-1}s^{-1}$ with and without silica solution. The actual values may be off by a factor of 2 at most. Again, the second-order kinetics should be applicable to the present experiment in heterogeneous media. In any case, the back reaction is about hundredfold retarded in the presence of silica particles. Figure 11 shows a difference spectrum for a 1.9×10^{-5} M $ZnTMePyP^{4+}$ solution with 1.0×10^{-5} M silica particles in the absence of a quencher, which was taken at 50 μs after the laser flash. The peak at 460 nm and the broad band in the red can be assigned to the triplet-triplet absorption spectrum because similar triplet-triplet absorption spectra have been found in several metalloporphyrins [23].

In the past, micelles have been widely used in the studies of heterogeneous solutions to effect the course of reaction by a combined hydrophobic and electrostatic interaction. k_b of reaction 3 was determined to be 2.4×10^9 $M^{-1}s^{-1}$ in 1.5×10^{-2} M sodium lauryl sulfate solution in this study. Since both reactants are hydrophilic and should stay in the aqueous side of the interface, the inefficiency in retarding this back reaction may be attributed to its low surface potential (~85 mV [15]) as compared to that on silica particles (vide

Figure 11. Difference spectrum taken at 50 μs after the flash. The solution contained 6.9×10^{-6} M of $ZnTMePyP^{4+}$ and 1×10^{-5} M of silica particles.

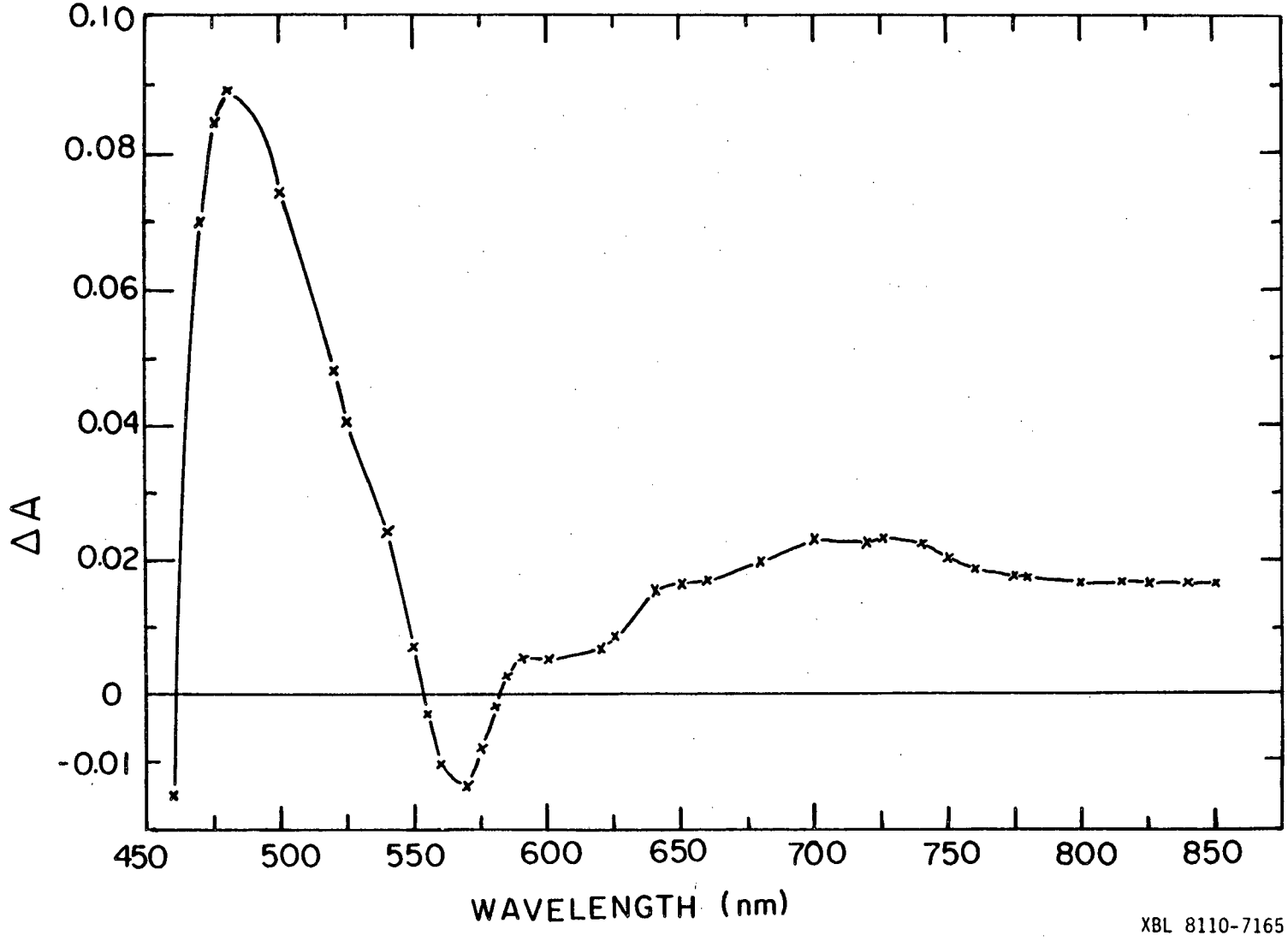

XBL 8110-7165

supra). Such a result is expected based on a simple kinetic argument assuming that the surface potential is the main energy barrier for the back reaction (see the summary at the end of this chapter).

Effect of ionic strength

With 0.1 M NaCl in the silica solution, the rate constant, k_b, of the back reaction of $Ru(bpy)_3^{3+}$ and PVS^- (reaction 3) was found to increase to $4.3 \times 10^8\ M^{-1}s^{-1}$ (Figure 10C). Since it is known that adding 0.1 M NaCl decreases the fluorescence lifetime of $Ru(bpy)_3^{2+}$ from 0.49 to 0.42 μs in silica solution, $Ru(bpy)_3^{2+}$ may be forced to stay mostly outside in the bulk. This suggests that ions with two or less positive charges are able to diffuse easily through the potential barrier at higher salt concentration. In fact, the potential barrier (or the Debye length, $L = \sqrt{\frac{\varepsilon kT}{8\pi e^2 C^\circ}}$, where C° is the concentration of the electrolyte in the bulk [16]) at 0.1 M NaCl is more than halved as compared to that in the solution containing only silica particles. This helps the back reaction to speed up by allowing either reactant to diffuse through the Stern layer more easily.

Effect of pH

As the pH of an alkaline colloidal solution is quickly lowered to 4.5, the gelling process is not fast enough to interfere with my experiments and the solution is in its metastable state. At this pH, since all surface silanol groups are protonated and the potential barrier is no longer there to retard the back reaction, k_b increases to $2.6 \times 10^9\ M^{-1}s^{-1}$ (Figure 10D). Rate constants at other pH values were similarly determined. The results are summarized in Figure 12. Let a smooth curve be drawn through the data points. k_b is found to increase to be almost diffusion-controlled at a pH around 5.5, which

Figure 12. Back reaction rate constant (k_b) as a function of pH in a 3.8×10^{-5} M colloidal silica solution

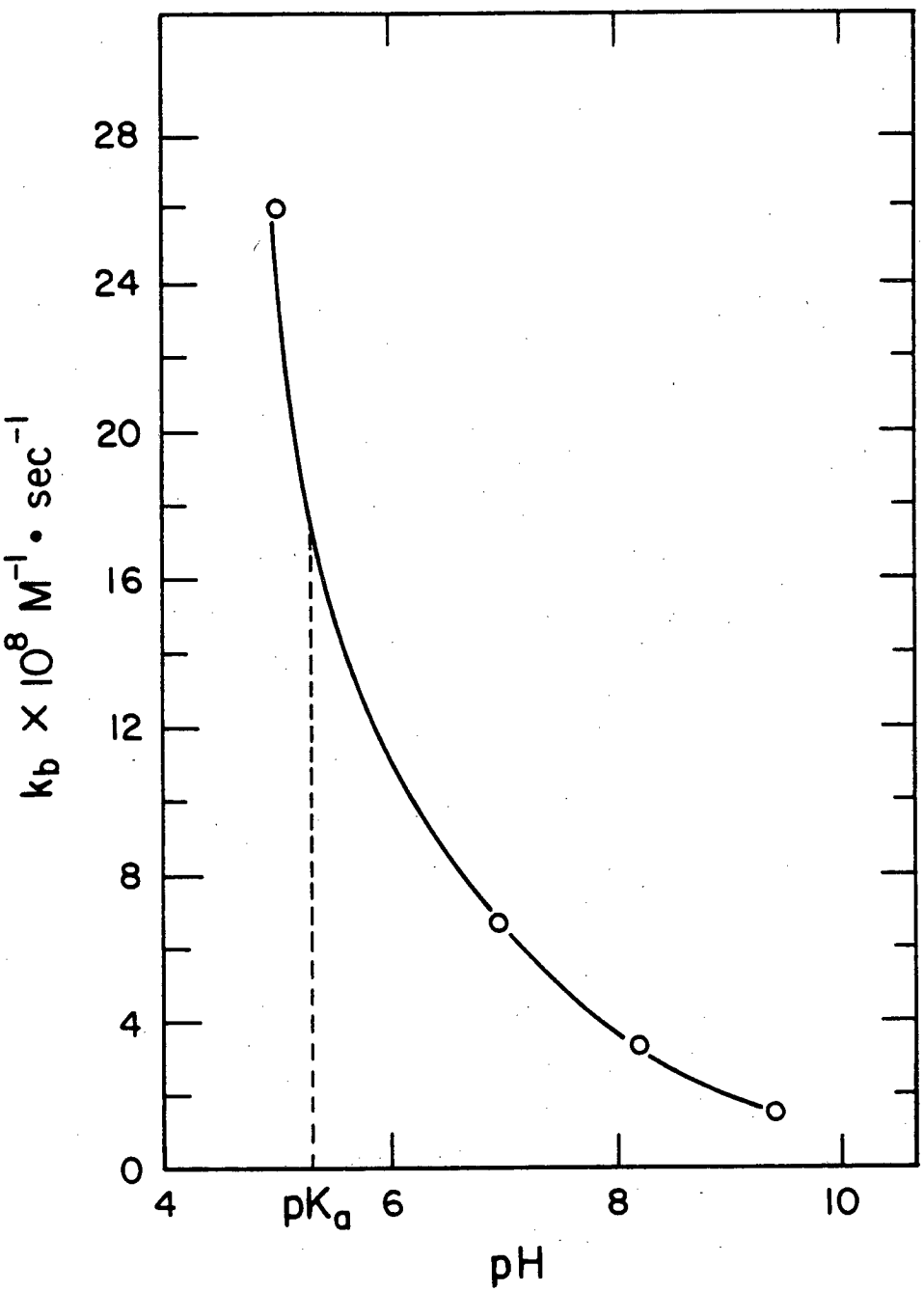

XBL 814-4562

corresponds to the pK_a of the silanol groups on colloidal silica [5].

Effect of Temperature

In order to further prove that surface potential keeps the reduced $PVS^{\cdot-}$ radicals away from the surface, reaction 3 was studied at several different temperatures. Experimental results are summarized in Table 1 and two of them are shown in Figure 13. Apparently, raising temperature increases the thermal energy of $PVS^{\cdot-}$ to better overcome the potential barrier. When these data are fitted by the Arrhenius equation,

$$k_b = A \exp(-E_a/RT) \qquad (5)$$

E_a is estimated to be 4.2 ± 0.3 kcal $mole^{-1}$ (Figure 14). This corresponds to 180 ± 20 mV for a singly charged reactant, which is in good agreement with the value estimated from Gouy-Chapmann equation. From this result, we may conclude that the surface potential contributes predominantly to the retardation of the back reaction between oppositely charged reactants.

Separation of products from solvent cage

Up to now, almost all factors which affect the reactions leading to the separated products have been detailed. Combining all these individual reactions together, we may express the quantum efficiency of the reduction of viologen by excited $Ru(bpy)_3^{2+}$ as

$$\phi_{V^{\cdot-}} = \phi_{CT} \cdot \phi_q \cdot \phi_s \qquad (6)$$

where ϕ_{CT} is the quantum yield for the formation of charge-transfer excited $Ru(bpy)_3^{2+}$, ϕ_q is the probability of quenching, and ϕ_s is the probability of the formation of separated photoproducts from the quenching encounter. ϕ_{CT} has been determined to be practically unity by the measurements of absolute luminescence quantum yield and excited-

TABLE 4-1

THE RATE CONSTANTS OF RECOMBINATION REACTIONS IN THE PRESENCE OF COLLOIDAL SILICA[a]

$$Ru(bpy)_3^{3+} + PVS^{\cdot-} \xrightarrow{k_b} Ru(bpy)_3^{2+} + PVS^{\circ}$$

pH[b]	NaCl added [M]	T (°K)	k_b ($M^{-1}sec^{-1}$)
9.8	0.025	295	2.7×10^8
9.8	0.1	295	4.3×10^8
9.8	0.2	295	5.2×10^8
8.2	----	295	3.9×10^8
6.5	----	295	6.9×10^8
4.5	----	295	2.6×10^9
9.8	----	295	5.6×10^7
9.8	----	301	6.5×10^7
9.8	----	321	9.0×10^7
9.8	----	334	1.5×10^8

a. Calculated from the decay curve of $PVS^{\cdot-}$ measured at λ = 602 nm. All decay curves are assumed to follow second order kinetics (see text).

b. Adjusted after all components are included in the system.

Figure 13. Transient absorption changes of $PVS^{\cdot-}$ followed at 602 nm at different temperatures with a constant intensity laser flash. (A) 293°K, (B) 333°K.

$[Ru(bpy)_3^{2+}] = 3.6 \times 10^{-5}$ M

$[PVS^{\circ}] = 4$ mM

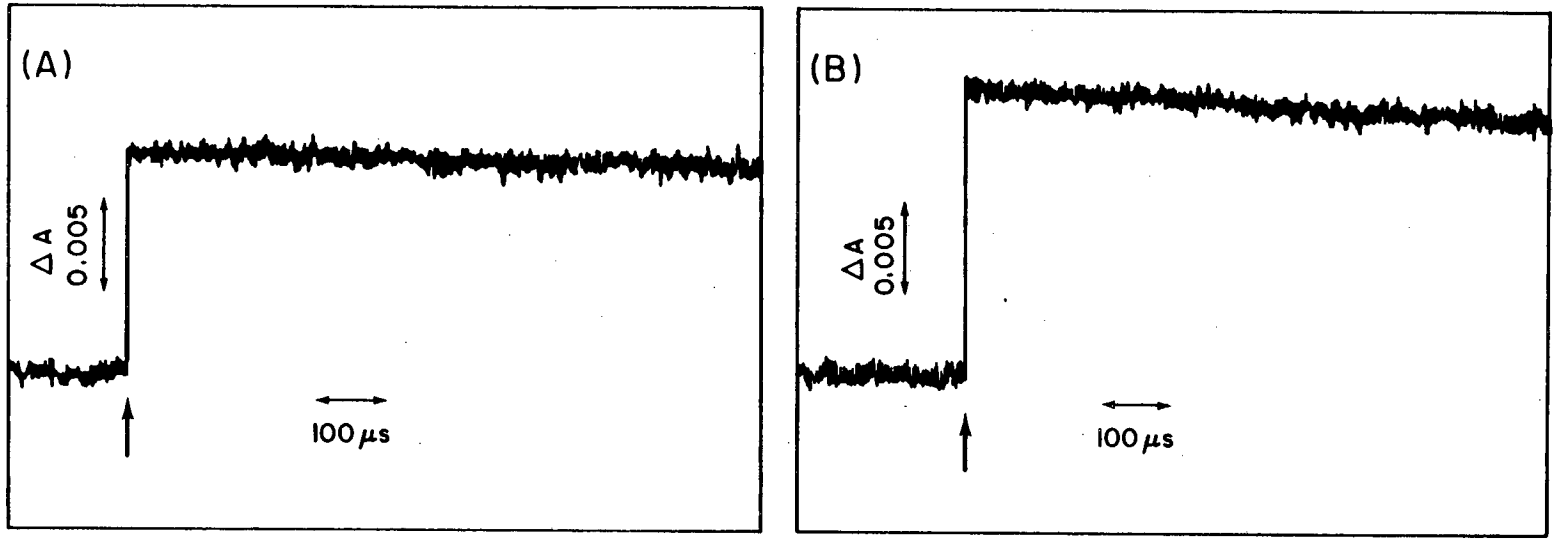

XBL 814-4558A

Figure 14. Arrhenius plot of log k_b vs 1/T, where k_b is the rate constant of back electron transfer reaction.

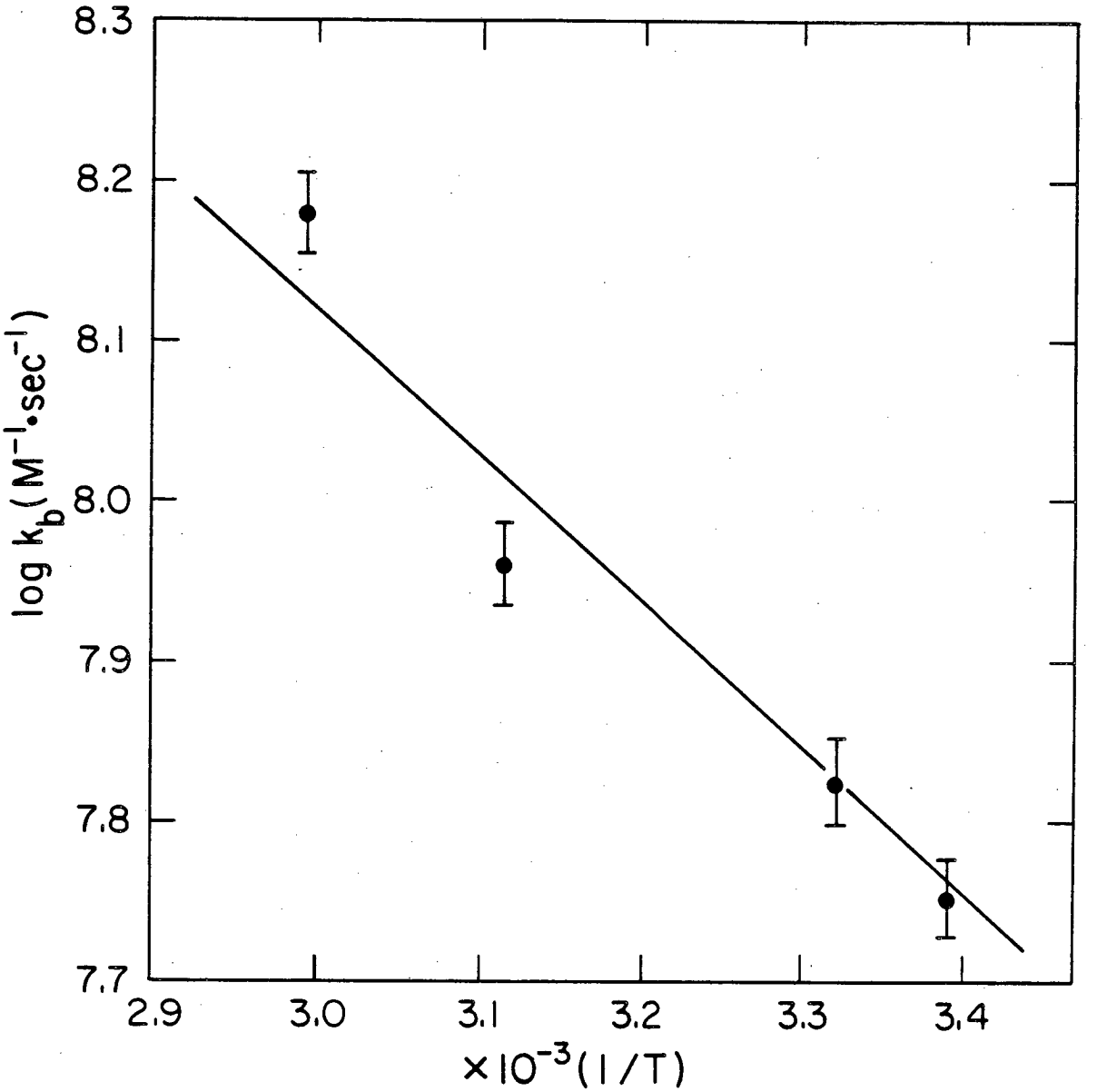
8.3
8.2
8.1
8.0
7.9
7.8
7.7
log k_b ($M^{-1}\cdot sec^{-1}$)
2.9
3.0
3.1
3.2
3.3
3.4
$\times 10^{-3}$ (1/T)

XBL 814-4566

state lifetime [17, 24]. This indicates that almost all excited $Ru(bpy)_3^{2+}$ complexes relax to their metal-to-ligand charge transfer excited states. Under my experimental conditions, the quenching probability of excited $Ru(bpy)_3^{2+}$ by PVS° in the presence of silica particles can be calculated as follows.

$$\phi_q = \frac{k_q[PVS^\circ]}{k_q[PVS^\circ] + k_o} \qquad (7)$$

$$= \frac{(1.2\times10^9)(4\times10^{-3})}{(1.2\times10^9)(4\times10^{-3}) + (1/(0.71\times10^{-6}))} = 0.77$$

where $k_o = 1.41 \times 10^6\ sec^{-1}$ is the decay rate constant of excited $Ru(bpy)_3^{2+}$ in the presence of silica particles, but in the absence of the quencher. From my flash photolysis experiments, $\phi_{PVS^{\cdot-}}$ was estimated by taking the ratio of the maximal amount of $PVS^{\cdot-}$ produced after the laser flash over the concentration of the ruthenium complex present in the solution to be about 0.04 ~ 0.05. Thus $\phi_s^{PVS^\circ}$ is estimated by eq. (6) to be 0.05 ~ 0.065, while that of $\phi_s^{MV^{2+}}$ was ~ 0.13. These results are expected because electrostatic attraction between oppositely charged ions promotes geminate recombination, whereas electrostatic repulsion between two positively charged products helps them separating from the surrounding solvent cage.

To further study the nature of the cage effect, I have measured the quantum yield of viologen reduction in silica solutions at several different temperatures. Using constant laser flash intensity, $\phi_{PVS^{\cdot-}}$ was found to be 0.06 at 60°C and 0.04 at 22°C. This suggests that thermal energy helps with the separation of photoproducts from the solvent cage. In other word, $\phi_s^{PVS^\circ}$ increases with increasing temperature. This 50% increase can not be due to the variation of ϕ_q, because ϕ_q is close

to unity and k_o decreases with increasing temperature.

At present, there is no evidence that the surface potential contributes to the separation of photoproducts from the cage. In the future, these experiments have to be repeated in a homogeneous solution so that any possible interference of silica particles can be avoided and the cage effect can be better characterized.

C. With PVS° as the primary electron acceptor and $Fe(CN)_6^{3-}$ as the secondary electron acceptor

Since the potential energy barrier on the silica surface is equal to the product of the charges on the incoming ions and the electric potential near the surface, the higher the number of negative charges on the ion, the more difficult it is for the ion to approach the surface. With the single negative charge on PVS^-, the surface potential has already retarded its reaction with $Ru(bpy)_3^{3+}$ by at least a hundredfold relative to that in homogeneous solutions. If further retardation is desired, one must use a multiply charged ion such that it can rarely reach the surface. However, having multiple charges implies that its oxidized form must have at least one negative charge. Based on our experimental results in this chapter, such a quencher cannot be expected to quench excited sensitizer efficiently when the Stern layer is thick and the surface potential is high. In order to get around this dilemma, an overall neutral electron acceptor such as PVS° should be used as an electron carrier to shuttle between the excited sensitizer and the anion with multiple charges. In this way, the electron from the excited sensitizer is uni-directionally transported to a multiply charged ion located only in the bulk. Thus the back reaction is further slowed down.

Indeed, with 0.1 mM $Fe(CN)_6^{3-}$ as the secondary electron acceptor and 4 mM PVS° as the primary acceptor and electron carrier, the results of flash photolysis experiment showed no obvious decay of $Ru(bpy)_3^{3+}$ at 470 nm over 1 ms interval and a rapid disappearance of $PVS^{\bar{\cdot}}$ ($t \leq 5$ μs) at 602 nm (Figure 15). This indicates that within the first 5 μs the reduced $PVS^{\bar{\cdot}}$ radical was first ejected into the bulk by the surface potential and then its extra electron was quickly picked up by some $Fe(CN)_6^{3-}$. Thus, through the coupling of two electron acceptors, an otherwise diffusion-controlled exothermic reaction between $Ru(bpy)_3^{3+}$ and $Fe(CN)_6^{4-}$ was drastically slowed down [18]. Without PVS° as the primary acceptor, $Ru(bpy)_3^{3+}$ was not observed using $Fe(CN)_6^{3-}$ as the quencher in the time scale of our experiment.

A schematic diagram representing these coupled electron-transfer reations is shown in Figure 16. This experiment not only demonstrates the principle but also provides a guideline for future design of electon acceptors. Also, since $Fe(CN)_6^{4-}$ is not sensitive to oxygen oxidation, using the $Fe(CN)_6^{3-}/Fe(CN)_6^{4-}$ couple as electron carriers between two photo reaction centers might prove useful.

Figure 15. Transient absorption changes of the intermediate photoproducts formed by flashing a solution containing $Ru(bpy)_3^{2+}$ (4.2×10^{-5} M), PVS° (4 mM), and 0.1 mM of $Fe(CN)_6^{3-}$. Decay of $PVS^{\cdot-}$ produced is followed at 602 nm. Bleaching of $Ru(bpy)_3^{2+}$ is followed at 470 nm.

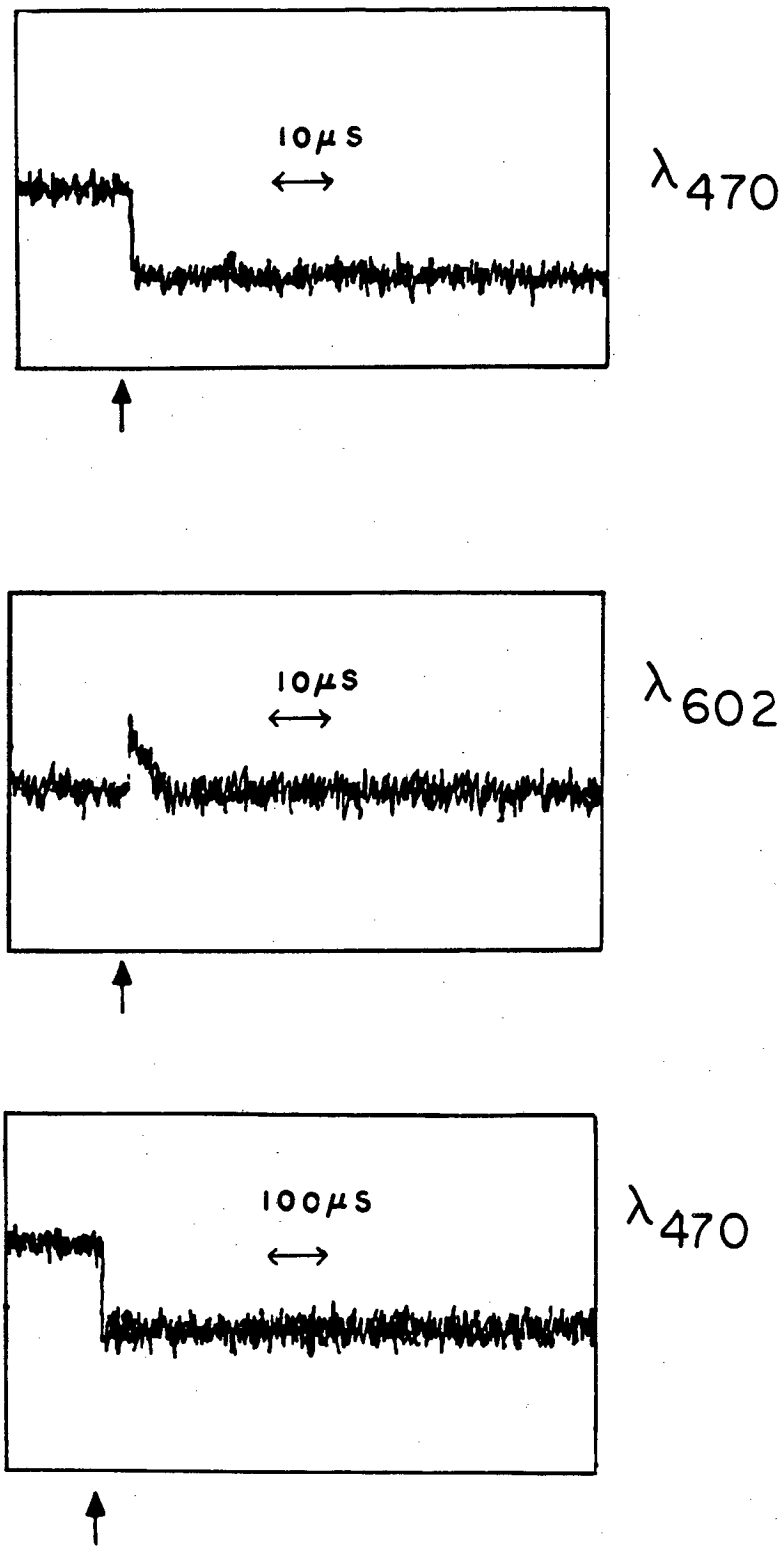

XBL 8110-7073

Figure 16. Schematic presentation of the function of colloidal silica in the separation of photoproducts with coupled electron acceptors.

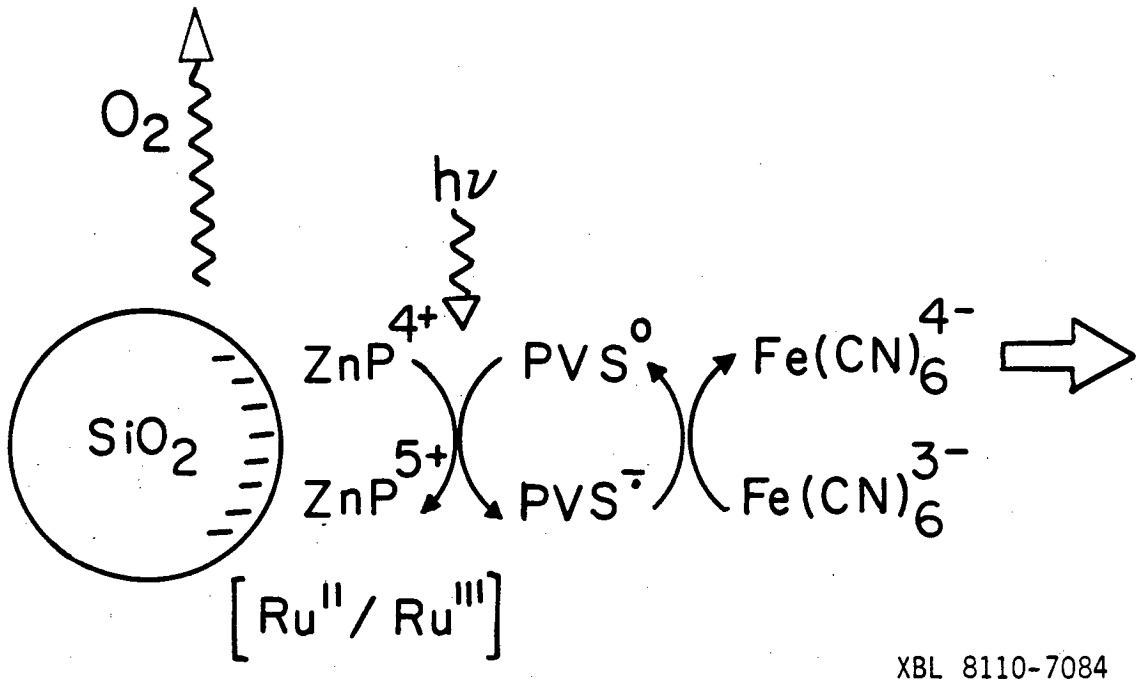

XBL 8110-7084

(6) Summary

In the previous sections, heterogeneous solutions with colloidal silica have been shown to exert both concentration and electrostatic effects on each step of electron-transfer reactions. By concentrating ionic reactants on the charged surface, the reaction rates can be increased by a hundredfold, as in the quenching reaction of excited $Ru(bpy)_3^{2+}$ by MV^{2+}. Also, by proper selection of reactants, the same electric field on charged particles substantially retards an undesired reaction. But, electrostatic interaction itself cannot enhance the forward reaction and slow down the backward reaction simultaneously. In order to optimize both, one component may be chosen to bind onto surface by forces other than electrostatic, e.g. hydrophobic or specific adsorption, whereas the other is concentrated on the surface by electrostatic attraction. This will increase the rate of the forward reaction. After electron-transfer reaction takes place, the oxidized or reduced former compound may then move out of the reaction center by virtue of its changed polarity and the repulsive interaction between it and the charged interface.

Recently, Willner in our group has carried out the continuous photolysis experiment with $Ru(bpy)_3^{2+}$ and PVS° using triethanolamine (TEOA) as the sacrificial electron donor. His results showed that the rate of $PVS^{\cdot-}$ formation in silica solution ($\phi = 0.04$) was eightfold higher than that in a homogeneous solution ($\phi = 0.005$) [19]. Putting all these results together, we may schematically represent the photochemical reactions in this heterogeneous silica solution in Figure 17. Currently, efforts are devoted to depositing RuO_2 as small islands on these particles so that the oxidized Ru(III) may quickly transfer its

Figure 17. Schematic function of colloidal silica in the separation of photoproducts formed in the photo-induced electron transfer reactions.

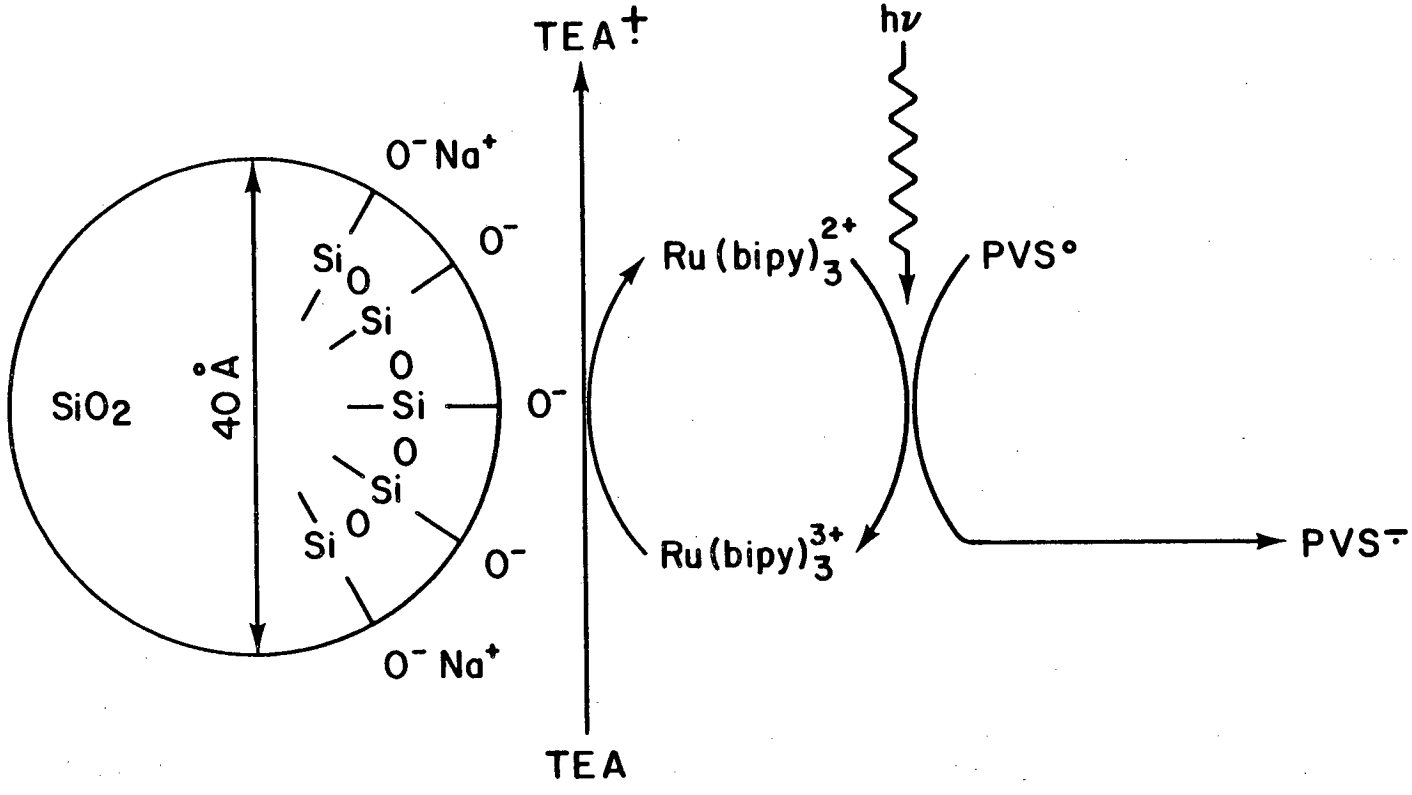
TEA+
hν
O⁻ Na+
O⁻
Si
O
Si
O
Si
O
Si
O
Si
O
SiO2
40 Å
O⁻
O⁻
O⁻ Na+
Ru(bipy)3 2+
PVS°
Ru(bipy)3 3+
PVS⁻
TEA

XBL 811-4426

oxidizing power to this oxygen catalyst to oxidize water. Since silica particles are only stable in alkaline solutions and $PVS^{\bar{\cdot}}$ radicals cannot reduce water at pH above 7.0, some other electron acceptors with lower reduction potential should be designed to substitute for PVS°. In the presence of a hydrogen-formation catalyst, which may dissolve either homogeneously (e.g. hydrogenase and its model compounds) or heterogeneously (e.g. colloidal Pt), the solar splitting of water may then be accomplished in this colloidal solution.

Part B. Photochemistry in polyelectrolytes

As compared to homogeneous solutions, heterogeneous solutions have offered three additional features to chemists for the manipulation of solution chemistry. They are the charged interface between the dispersed phase and the bulk phase, two reaction media with different polarities, and a high surface-to-volume ratio. In part A, some of these features in colloidal silica have been explored. However, the instability of silica particles at lower pH and the absence of a hydrophobic phase have prompted us to search for better heterogeneous solutions. Since the contribution of surface potential to both charge separation and the concentration of reactants has been revealed, an ideal heterogeneous solution must not only show the aforementioned features but also be capable of sustaining a high surface potential near its interface. Micellar solutions can certainly satisfy the former, but their surface potentials are typically low. In order to hold a higher surface potential, the rigidity of these micelles must be strengthened (e.g. by polymerization). This suggests that a micro-sphere latex with most of its surface groups ionizable may be the best choice.

In this second part, some photo-induced electron-transfer reactions in poly-acrylate will be examined. Polyelectrolyte was chosen because it might serve as the prototype of charged micro-sphere latex particles. In addition, the electrochemistry of water soluble $ZnTMePyP^{4+}$ will be discussed.

(1) Electrochemistry of $ZnTMePyP^{4+}$

Cyclic voltammogram of $ZnTMePyP\cdot(ClO_4)_4$ was taken with a platinum inlay electrode in acetonitrile solution with 0.1 M tetraethylammonium

perchlorate (TEAP) as the supporting electrolyte (Figure 18). $E_{1/2}$ was measured as +1.22 volts vs SCE. This value is about 0.5 volts higher than that of zinc tetraphenylporphyrin (ZnTPP). It is not surprising to find such a high reduction potential for $ZnTMePyP^{4+}$ since the presence of its four positively charged pyridinium groups makes it very difficult to place an extra positive charge on the porphyrin ring. If this explanation is correct, then it may explain the point expressed recently by A. Harriman et al. [20]. From spectroscopically measured triplet energy, they estimated the ground state redox potential E_o of $ZnTMePyP^{5+/4+}$ couple to be in the range of +0.9 to 1.1 eV instead of the value +1.20 V (vs NHE ?) reported by Kalyanasundaram and Grätzel [21]. (Actually, Grätzel referred the value +1.2 V to Newmann-Spallart's unpublished result.) I expect that the first ring oxidation potential of $ZnTMePyP^{4+}$ should differ depending on which counter ion is used and also on which solvent it is dissolved in. In aqueous solution with a high ionic strength, this oxidation potential should be lower.

Efforts to obtain the optical spectrum of $ZnTMePyP^{5+}$ from total electrolysis were not successful due to the high reduction potential of this porphyrin and difficulties in removing trace water and impurities from the solvent. Thus, a thin-layer optically transparent electrode was used. Figure 19a shows the spectrum of $ZnTMePy^{5+}$ recorded in situ. As compared to the known spectrum of $ZnTPP^{+\cdot}$ (Figure 19b), it displays similar blue absorption bands and an extended visible and red absorption. It should be pointed out here that since all recent publications used the absorptivity of $ZnTPP^{+\cdot}$ [22] for $ZnTMePyP^{5+}$, their calculated rate constants should be viewed only as

Figure 18. Cyclic voltammogram of $ZnTMePyP\cdot(ClO_4)_4$ in acetonitrile solution containing 0.1 M TEAP as supporting electrolyte. Scan rate: 100 mV/s.

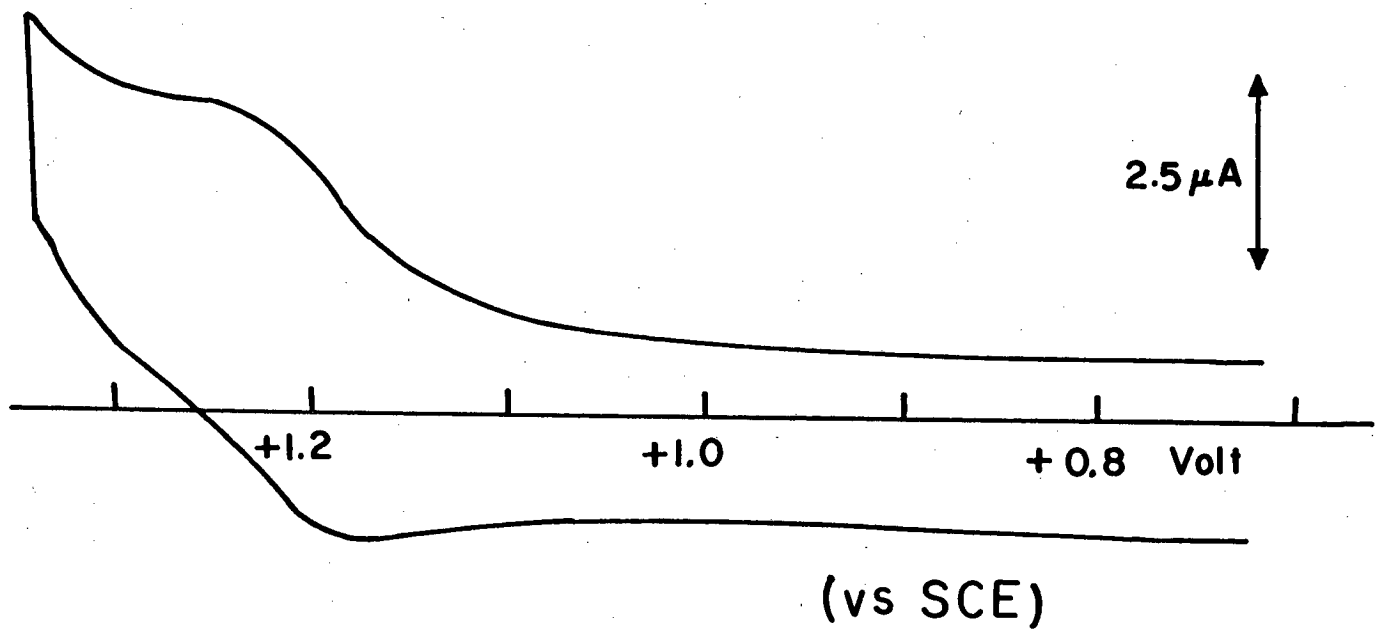

XBL 819-4993

Figure 19. Absorption spectra of (a) $ZnTMePyP\cdot(ClO_4)_4$ ——, and its oxidized product $ZnTMePyP^{5+}$ ------ in acetonitrile solution containing 0.1 M TEAP as supporting electrolyte; (b) $ZnTPP^{+\cdot}$ from reference 22.

ZnTPP ———— ,

$ZnTPP^{+\cdot}$ ------ in CH_2Cl_2.

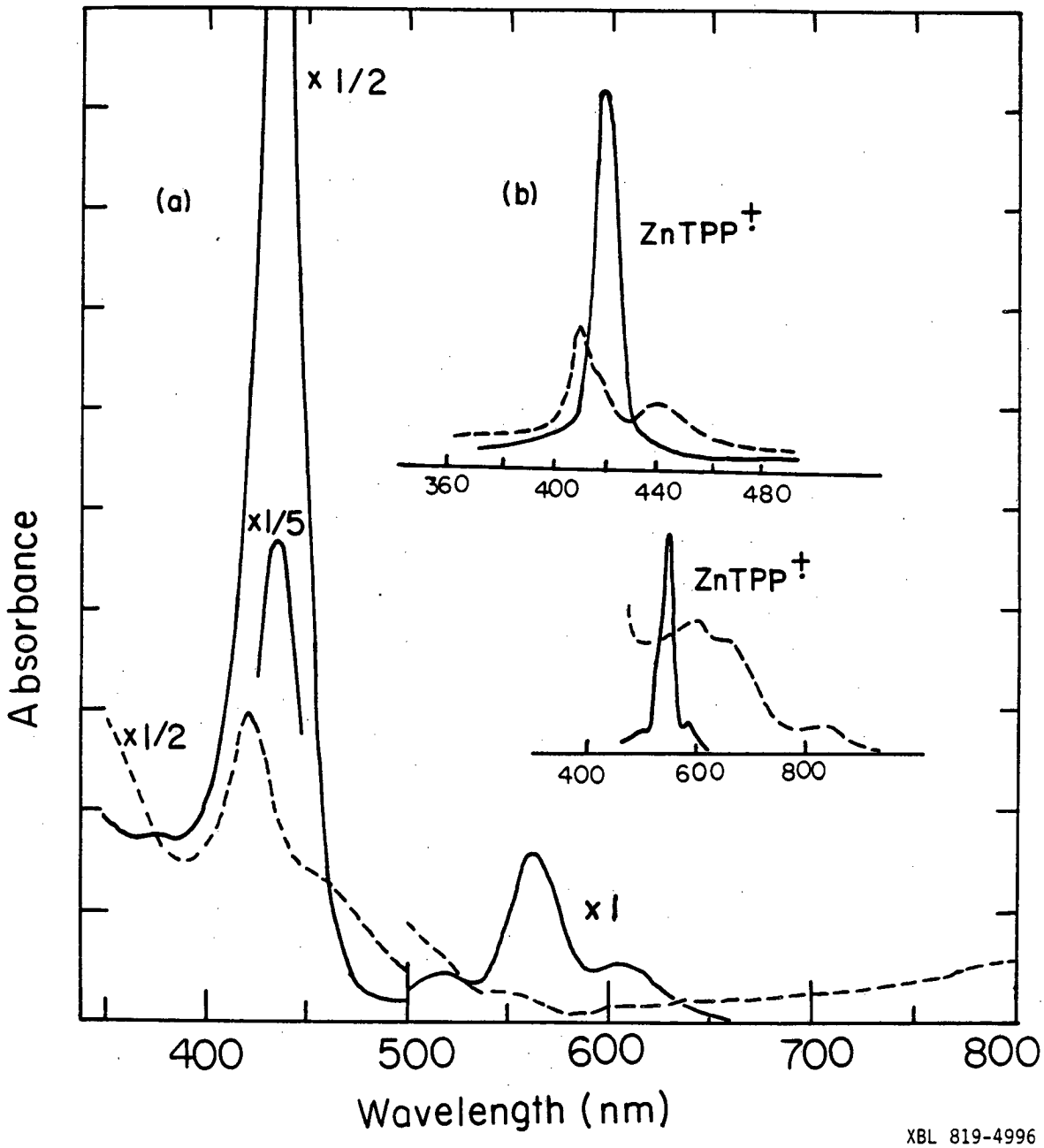
x 1/2
(a)
(b)
ZnTPP+
360
400
440
480
x1/5
ZnTPP+
400
600
800
x1/2
x1
Absorbance
400
500
600
700
800
Wavelength (nm)

XBL 819-4996

approximate values. One should also be aware that their referred spectrum was obtained in an organic medium in the same way as that acquired in my study and the actual spectrum might be different in an aqueous solution. In the future, the optical spectrum of $ZnTMePyP^{5+}$ should be taken using a flash photolysis setup and an excess europium nitrate as the quencher, because reduced europium ion is colorless in the spectral region of interest. Also, the variations of the redox potential of a charged sensitizer in different media deserve further exploration.

(2) With $Ru(bpy)_3^{2+}$ as the sensitizer

In a pH 9.8 aqueous solution containing 1.5×10^{-5} M polyacrylate (or 1.04×10^{-2} M in terms of monomer), the Stern-Volmer plot of the excited state quenching by MV^{2+} was found to behave abnormally (Figure 20). It first reached a maximum at about 1 mM MV^{2+}, and then it decreased upon further increase of $[MV^{2+}]$. Again, quenching reversal is recalled to explain this abnormality. At a low concentration of MV^{2+}, both MV^{2+} and $Ru(bpy)_3^{2+}$ are concentrated around the charged polymers by electrostatic interaction so that the rate of quenching reaction is greatly enhanced. The apparent quenching constant k_q was calculated to be 2.45×10^{10} $M^{-1}s^{-1}$ by assuming that the excited-state lifetime of the sensitizer is 0.4 μs. As the concentration of MV^{2+} increases, adsorbed $Ru(bpy)_3^{2+}$ complexes are gradually displaced from the surface of polymer chains into the bulk solution, where they resume a normal quenching as in homogeneous solutions.

With PVS° substituted as the quencher, a regular Stern-Volmer plot was observed and k_q was calculated to be 1.52×10^9 $M^{-1}s^{-1}$ (Figure 20). Addition of 0.38 M NaCl increased k_q only slightly to 1.85×10^9

Figure 20. Stern-Volmer plots of the quenching of excited $Ru(bpy)_3^{2+}$ by (a) —▲—▲, MV^{2+}; (b) —x—x, PVS°.

All solutions (pH 9.7) contained

$[Ru(bpy)_3^{2+}] = 3.4 \times 10^{-5}$ M

[Poly-acrylate] = 1.5×10^{-5} M polymer

= 1.04×10^{-2} M monomer.

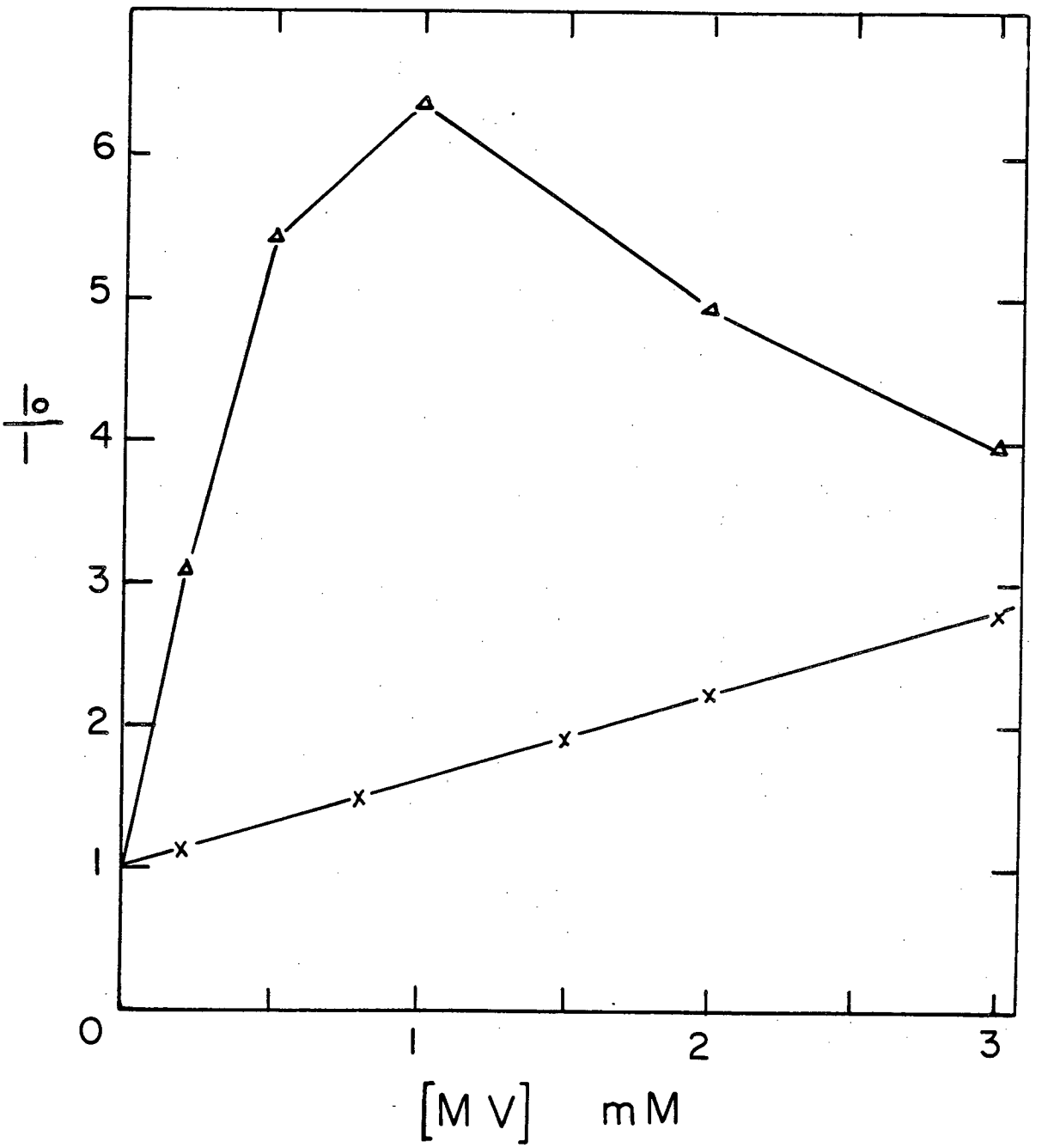

XBL 8110-7075

$M^{-1}s^{-1}$.

In the continuous photolysis experiments, 2.5×10^{-2} M triethanolamine and 1 mM MV^{2+} or PVS° were added as the sacrificial electron donor and electron acceptor, respectively. The results are summarized in Figure 21, and the quantum yields are tabulated in Table 2. As shown clearly in this figure, the results can be nicely explained by the concentration and electrostatic effects discussed in part A. The solution containing $Ru(bpy)_3^{2+}$ and PVS° in poly-acrylate has the highest yield because the back reaction ($k_q = 2.5 \times 10^9$ $M^{-1}s^{-1}$) is retarded by the surface potential, whereas the solution containing $Ru(bpy)_3^{2+}$ and MV^{2+} in poly-acrylate has the lowest yield because the reactants of the back reaction are unfavorably confined near the surface despite of the fact that the quenching reaction is enhanced. When comparing these data, however, one must be aware that the quantum yield ϕ_s of product separation from quenching encounter with MV^{2+} as the quencher is more than twice that with PVS° as the quencher (part A and Figures 21D and B) and that all these yields should depend on the ionic strength of their media because ionic reactants are involved in these reactions.

(3) With $ZnTMePyP^{4+}$ as the sensitizer

Water-soluble $ZnTMePyP^{4+}$ was investigated not only because porphyrins and their analogs play important roles in the respiratory chain and in photosynthesis but also because this particular porphyrin with its extended visible spectrum is potentially capable of splitting water. These characteristics render $ZnTMePyP^{4+}$ especially attractive as a sensitizer.

Continuous photolysis experiments were similarly carried out with

Figure 21. $PVS^{\cdot-}$ formation as a function of the total light absorbed under continuous illumination.

$[Ru(bpy)_3^{2+}] = 7 \times 10^{-5}$ M

[PVS°] or $[MV^{2+}] = 1$ mM

$[TEOA] = 2.5 \times 10^{-2}$ M

[poly-acrylate] = 1.1×10^{-2} M monomer

(A) with polymer, Ru(II), PVS°, TEOA;

(B) with 1.1×10^{-2} M sodium acetate, Ru(II), PVS°, TEOA;

(C) with polymer, Ru(II), MV^{2+}, TEOA;

(D) with 1.1×10^{-2} M sodium acetate, Ru(II), MV^{2+}, TEOA.

All experiments at pH 9.8 and at 22°C.

The number of photons actually absorbed by the sensitizer was 2.16×10^{-7} einstein/s and the illuminated area was about 1.2 cm^2. The abscissa shows the total amount of photons absorbed by the ruthenium complex.

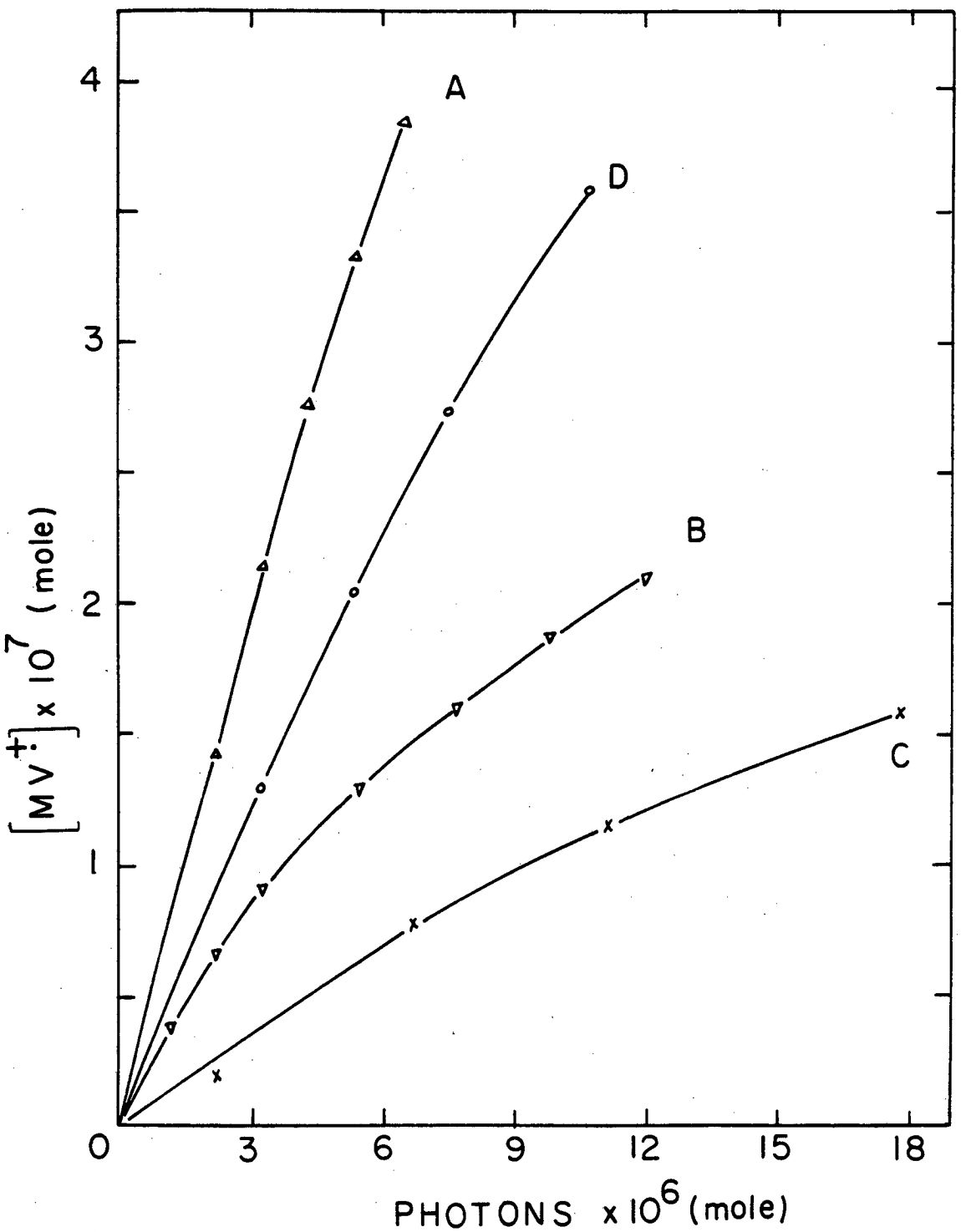

XBL 8110-7077

TABLE 4 - 2

QUANTUM YIELDS OF VIOLOGEN FORMATION UNDER CONTINUOUS ILLUMINATION*

A. WITH $Ru(bpy)_3^{2+}$ as the sensitizer [a]

$[Ru(bpy)_3^{2+}] = 7 \times 10^{-5}$ M; [TEOA] = 2.5×10^{-2} M

	PVS° [mM]	MV^{2+} [mM]	poly-acrylate [M]	NaOAc [M]	ϕ
(A)	1	——	1.1×10^{-2}	——	6.5%
(B)	1	——	——	1.1×10^{-2}	3.4%
(C)	——	1	1.1×10^{-2}	——	1.2%
(D)	——	1	——	1.1×10^{-2}	4.0%

B. WITH $ZnTMePyP^{4+}$ as the sensitizer [b]

$[ZnTMePyP^{4+}] = 6 \times 10^{-6}$ M; [TEOA] = 2.5×10^{-2} M

	PVS° [mM]	MV^{2+} [mM]	poly-acrylate [M]	NaOAc [M]	ϕ
(A)	1	——	1.2×10^{-2}	——	38%
(B)	1	——	——	1.2×10^{-2}	20%
(C)	——	1	1.2×10^{-2}	——	7.5%
(D)	——	1	——	1.2×10^{-2}	9.3%

a. Total absorbed photons = 2.16×10^{-7} moles/s.

b. Total absorbed photons = $1.3 \pm 0.2 \times 10^{-7}$ moles/s.

* These quantum yields are calculated from the results shown in Figure 21.

6×10^{-6} M $ZnTMePyP^{4+}$ as the sensitizer and 2.5×10^{-2}M triethanolamine as the electron donor. The results are shown in Figure 22, and the quantum yields are tabulated in Table 2. These results are qualitatively similar to those data obtained with $Ru(bpy)_3^{2+}$ as the sensitizer except that the quantum yields here are about 6 times higher and also in homogeneous solution the quantum yield of photo-induced viologen radicals with PVS° as the electron acceptor is higher than that with MV^{2+} as the acceptor. The latter may be ascribed to a small quenching constant k_q of excited $ZnTMePyP^{4+}$ by MV^{2+} [k_q = $1.8 \pm 0.2 \times 10^7$ $M^{-1}s^{-1}$ from ref. 20] and a higher quantum yield $\phi_s^{PVS°}$ of product separation from the cage with PVS° as the acceptor. Since the quenching efficiency ϕ_q in my experimental conditions with $Ru(bpy)_3^{2+}$ as the sensitizer was calculated to be 0.77 in part A, the higher overall yield with $ZnTMePyP^{4+}$ must be attributed to a higher ϕ_s for the product separation from the solvent cage. In fact, a lower limit for $\phi_s^{PVS°}$ is estimated to be 0.4 from my laser photolysis studies. Also, the quenching constant k_q of excited $ZnTMePyP^{4+}$ by PVS° is estimated from Stern-Volmer equation ($\tau_0/\tau = 1 + k_q\tau_0[PVS°]$) to be 3×10^7 $M^{-1}s^{-1}$ by monitoring the decay of the triplet state at 825 nm.

In order to find out whether the surface potential contributes to the retardation of back reaction between $ZnTMePyP^{5+}$ and $PVS^{\cdot-}$, the decay of both species after the laser flash was monitored at 650 nm with and without poly-acrylate (Figure 23). Although the real extinction coefficient of $ZnTMePyP^{5+}$ at 650 nm is not available for the time being, the comparison can still be made and the ratio of their rate constants in the solution with and without polyacrylate is calculated to be 1/4. The surface potential has slowed down the back

Figure 22. $PVS^{\bar{\cdot}}$ formation as a function of the total light absorbed under continuous illumination.

$[ZnTMePyP^{4+}] = 6 \times 10^{-6}$ M

[PVS°] or $[MV^{2+}] = 1$ mM

$[TEOA] = 2.5 \times 10^{-2}$ M

[poly-acrylate] = 1.2×10^{-2} M monomer or

= 1.7×10^{-5} M polymer

(A) with polymer, $ZnTMePyP^{4+}$, PVS°, and TEOA;

(B) with 1.2×10^{-2} M of sodium acetate, $ZnTMePyP^{4+}$, MV^{2+}, and TEOA;

(C) with polymer, $ZnTMePyP^{4+}$, MV^{2+}, and TEOA;

(D) with 1.2×10^{-2} M of sodium acetate, $ZnTMePyP^{4+}$, MV^{2+}, and TEOA.

All experiments at pH 9.8 and at 22°C.

The number of photons actually absorbed by the sensitizer was 1.3×10^{-7} einstein/s and the illuminated area was about 1.2 cm^2. The abscissa shows the total amount of photons absorbed by the zinc porphyrin.

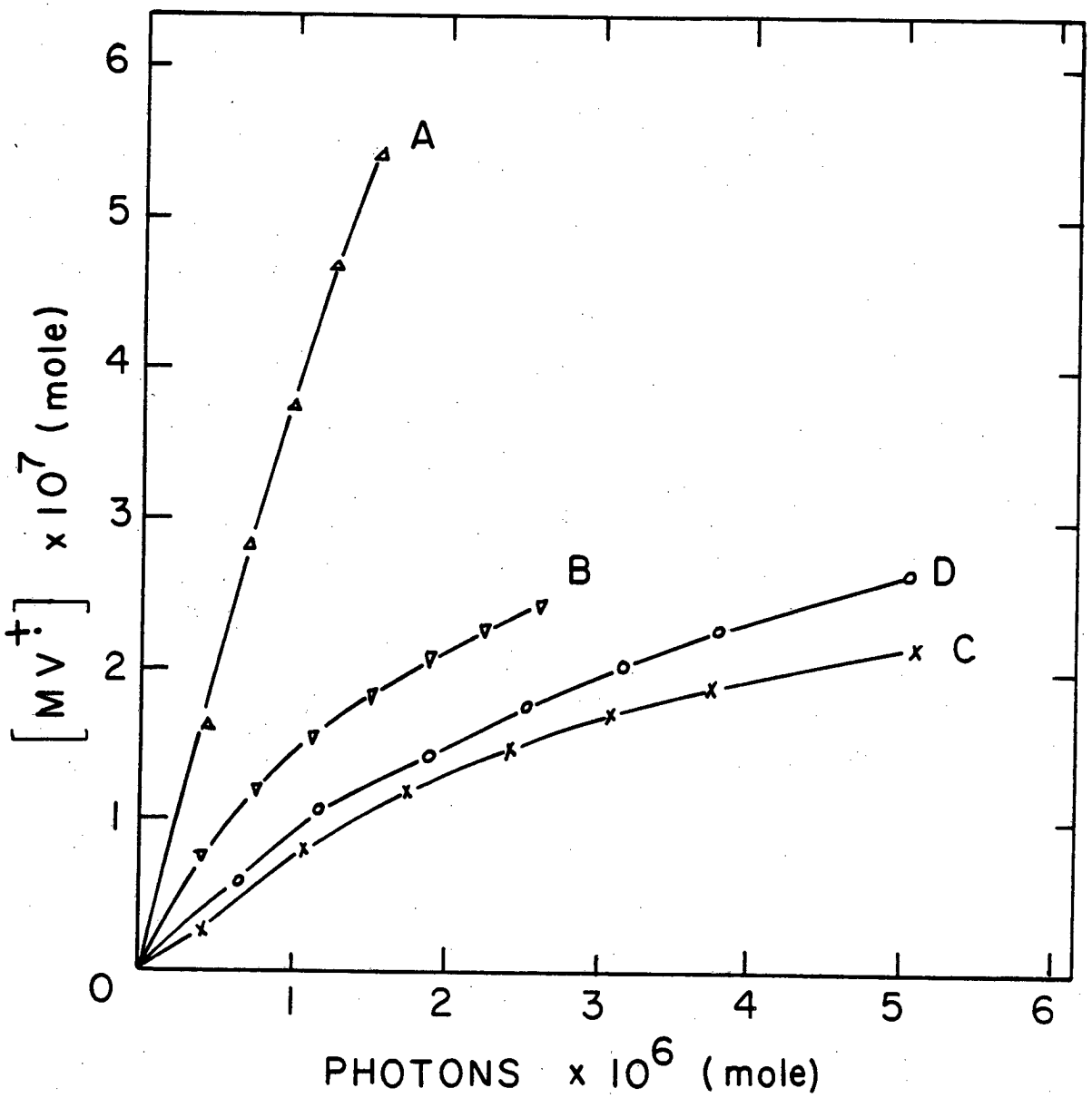

XBL 8110-7076

Figure 23. Decays of $PVS^{\bar{\cdot}}$ and $ZnTMePyP^{5+}$ monitored at 650 nm.

(A) with 1.2×10^{-2} M of poly-acrylate;

(B) without polymer.

Both have $[ZnTMePyP^{4+}] = 6.9 \times 10^{-6}$ M

and $[PVS^{\circ}] = 5$ mM in pH 9.6 solutions.

A

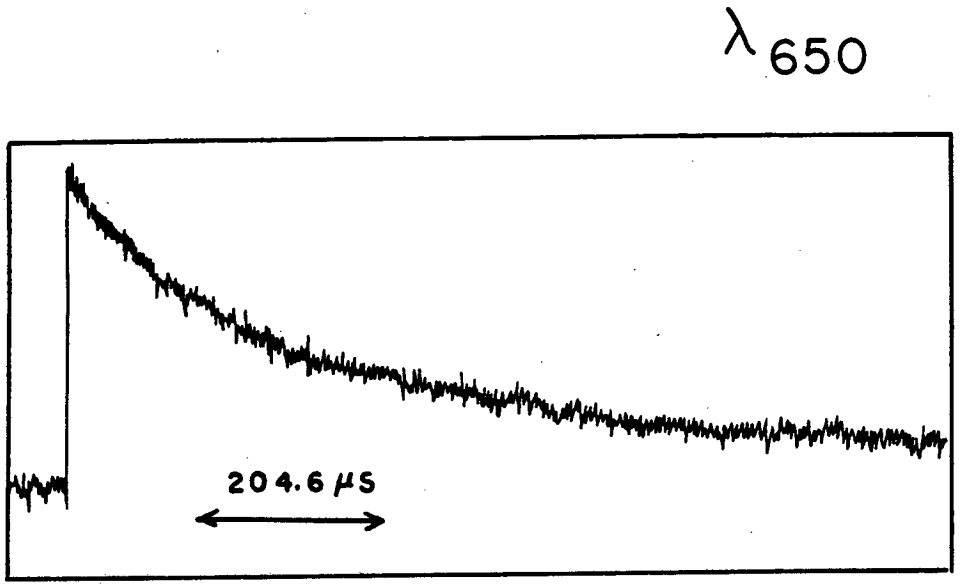

B

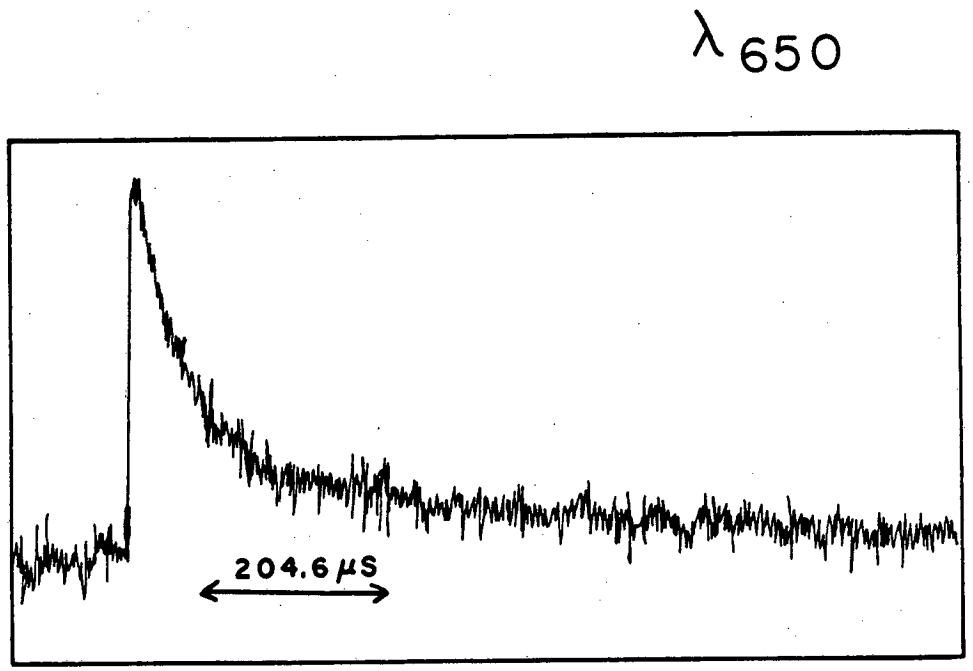

XBL 8110-7074

reaction only slightly as compared to the case in silica solutions (see part A(5)).

(4) Summary

I have shown that the effect of polyelectrolyte on photo-induced electron transfer reactions is similar to that of colloidal silica. However, the surface potential in poly-acrylate is not as high. If we assume that the rate constant is solely dependent on the surface potential, the rate constant k_b may be expressed as

$$k_b = A \cdot \exp[-eV/kT]$$

where A is the frequency factor, k is the Boltzmann constant, e is the electronic charge, and V is the surface potential. While the rate constant in colloidal silica is a hundredth of that in homogeneous solution, that in poly-acrylate is only one fourth. Substituting these ratios into equation 8, one has

$$\log_e [(1/100)/(1/4)] = [-170 + V]/kT$$

where V is the surface potential of poly-acrylate. V is calculated to be ~87 mV, which is a typical value found in micellar solutions.

As compared to $Ru(bpy)_3^{2+}$ as a sensitizer, $ZnTMePyP^{4+}$ not only extends the absorption spectrum to 600 nm but also has a higher overall quantum yield (Table 2). The latter may reflect the structural differences in these two encounter complexes. While Grätzel and Harriman preferred to interpret the slowness of the reaction between excited $ZnTMePyP^{4+}$ and MV^{2+} in terms of a modest thermodynamic driving force [20, 21], it might be better to explain this in terms of the difficulties in forming an effective encounter complex.

References

1. (a) N. J. Turro, M. Grätzel, and A. M. Brown, Angew. Chem., Internat. Ed., 19, 675 (1980).

(b) I. Willner, W. E. Ford, J. W. Otvos, and M. Calvin, Nature, 280, 823 (1980).

(c) D. Meisel and M. Matheson, J. Amer. Chem. Soc., 99, 6577 (1979).

(d) M. S. Tunuli and J. H. Fendler, J. Amer. Chem. Soc., 103, 2507 (1981).

2. W. E. Ford, Ph.D. thesis, University of California at Berkeley (1980).

3. A. Adler, F. R. Longo, F. Kampas, and J. Kim, J. Inorg. Nucl. Chem., 32 2443 (1970).

4. E. Wagner and A. W. Adamson, J. Amer. Chem. Soc., 88, 394 (1966).

5. Ralph K. Iler, "The Chemistry of Silica", John Wiley and Sons, New York (1979).

6. From Technifaxes 109 and 110 published by Nalco Chemical Company, 2901 Butterfield road, Oak Brook, Ill. 60521.

7. R. K. Iler, "The Colloid Chemistry of Silica and Silicates", Cornell University Press, Ithaca, New York (1955), p. 233.

8. (a) M. N. Jones, "Biological Interfaces", Elsevier Scientific Publishers, New York (1975), chapter 6, p. 135-162.

(b) M. J. Rosen, "Surfactants and Interfacial Phenomena", Wiley-Interscience, New York (1978), p. 28-55.

(c) A. M. James, Chem. Soc. Rev., 8, 289 (1979).

9. J. H. Fendler and E. J. Fendler, "Catalysis in Micellar and Macromolecular Systems", Academic Press, New York (1975), Chapter 2.

10. A. A. Krasnovskii and G. P. Brin, Dokl. Akad. Nauk, SSSR, 16, 761 (1965).

11. P. A. Trudinger, Analyt. Biochem., 36, 222 (1970).

12. J. N. Demas and C. M. Flynn, Jr., Anal. Chem., 48, 353 (1976).

13. G. Scatchard, Chem. Rev. 10, 229 (1932).

14. D. Meisel, J. Rabani, D. Meyerstein, and M. S. Matheson, J. Phys. Chem., 82, 985 (1978).

15. C. Laane, I. Willner, J. W. Otvos, and M. Calvin, Proc. Natl. Acad. Sci., 78, 0000 (1981)

16. V. A. Myamlin and Y. V. Pleskov, "Electrochemistry of semiconductors", Plenum Press, New York (1967).

17. F. Boletta, M. Maestri, and V. Balzani, J. Phys. Chem., 80, 2499 (1976).

18. E. Pellizetti and E. Pramauro, Inorg. Chem., 18, 882 (1979).

19. I. Willner, J. W. Otvos, and M. Calvin, J. Amer. Chem. Soc., 103, 3203 (1981).

20. A. Harriman, G. Porter and M.-C. Richoux, J. Chem. Soc., Faraday Trans., 2, 833 (1981).

21. K. Kalyanasundaram and M. Grätzel, Helv. Chim. Acta, 63, 478 (1980).

22. J. H. Fuhrhop and D. Mauzerall, J. Amer. Chem. Soc., 91, 4174 (1969).

23. A. Harriman, J. Chem. Soc., Faraday Trans. 2, 77, 1281 (1981).

24. J. N. Demas and G. A. Crosby, J. Amer. Chem. Soc., 93, 2841 (1971).

CHAPTER V

LIQUID-JUNCTION SOLAR CELL

5.1. INTRODUCTION

The conversion of solar energy into chemical energy with a semiconductor as the mediator has been shown to be promising as a result of the tremendous research efforts in the past decade. Since the work of Honda and coworkers in 1969 [1], many technical problems concerning the practical application of liquid-junction solar devices have been recognized. They are summarized as follows [2]:

1) The band-gap energy of a semiconductor chosen for such a purpose should be near that for the optimum utilization of solar radiant energy, which is about 1.1 to 1.3 ev.
2) The flat-band potential of a n-type semiconductor should be as negative as possible to increase its reducing power.
3) The semiconductor should be stable when in contact with the surrounding solution both in the dark and under illumination.
4) Polycrystalline materials with good efficiency should be used, so the high cost of the fabrication of single crystals can be avoided.
5) Doping level should be adjusted with respect to the absorption coefficient of a semiconductor so that most of the light is absorbed within the space-charge region.

Many of these requirements can be fulfilled by a careful selection of materials and by chemical conditioning processes, as was demonstrated by Parkinson et al. [3]. They achieved a 12% solar-to-electrical energy conversion efficiency with a

$$n\text{-GaAs} \ / \ Se^{2-}\text{-}Se_x^{2-}\text{-}OH^- \ / \ C$$

liquid junction solar cell [3]. However, the technology of a direct solar-to-chemical energy conversion is not yet well resolved, except with a few not very practical, wide band-gap semiconductors, e.g. $SrTiO_3$, which absorb only in the ultraviolet region. Almost all small band-gap semiconductors undergo surface decomposition under illumination [4].

Recently, McGregor in our group has reported that a thin chemisorbed Zinc-Phthalocyanine (ZnPc) film on ZnO polycrystalline electrode protects the electrode from photo-anodic dissolution (eq. 1)

$$(ZnO)_C + 2\ h^+ \longrightarrow Zn^{2+} + 1/2\ O_2 \qquad (1)$$

by providing a more favorable pathway by which the holes can reach the electrolyte [5]. The proposed mechanism is as follows.

$$(ZnO)_C \longrightarrow (ZnO)_C + h^+ + e^- \qquad (2)$$

$$2\ H_2O + 4\ h^+ \longrightarrow 4\ H^+ + O_2 \qquad (3)$$

$$ZnPc + h^+ \longrightarrow ZnPc^+ \qquad (4)$$

$$4\ ZnPc^+ + 2\ H_2O \longrightarrow O_2 + 4\ H^+ + 4\ ZnPc \qquad (5)$$

Later, Wrighton also showed that the surface derivatization by ferrocene could protect semiconductors from photo-destruction [6]. These results together indicate that a substantial improvement of the durability of semiconductors used in liquid-junction solar cells may be achieved, and redox processes on the interface may be directed.

In this chapter, the experiment which McGregor investigated briefly was followed up, and some further characterization of ZnPc-dyed ZnO will be discussed. ZnO was chosen because of the ease of fabrication and its well-studied photo-dissolution chemistry in aqueous solution under UV irradiation. In addition, electron-transfer

processes across the ZnO-electrolyte interface will be elaborated.

5.2.1 SOME BASIC NOTIONS ON SEMICONDUCTORS

As atoms condense to form a solid with a periodic lattice, atomic orbitals are perturbed and rearranged into energy bands of the solid as a whole. The schematic energy diagram of a model system consisting of a linear array of six atoms is shown in Figure 1A [7]. Depending on the bonding properties of its constituent atoms and lattice structure, every solid shows its characteristic resistivity towards an external applied electric field. At room temperature, the electric resistivities of metals are of the order of 10^{-4} to 10^{-6} ohm-cm, whereas those of insulators range from 10^{22} to 10^{10} ohm-cm. Semiconductors span between metals and insulators and generally have resistivities from 10^{9} to 10^{-3} ohm-cm.

In the solid, electrons fill up the allowable electronic orbitals in energy bands according to the Pauli exclusion principal and Fermi-Dirac distribution function,

$$f(E) = \frac{1}{1 + \exp[(E - E_F)/kT]}$$

f(E) expresses the probability of an orbital of energy E being occupied at temperature T and is independent of the physical nature of the system involved. E_F is the Fermi energy, or the chemical potential, at which f(E) is 1/2. At absolute zero temperature, all the levels up to the Fermi energy are occupied and all levels above are vacant. With a given density of energy states N(E), the concentration of electrons n(E) can be calculated by the following equation (see also Figure 1B):

$$n(E) = f(E) \cdot N(E) \cdot dE$$

Figure 1. (A) Energy diagram of a model system consisting of a linear array of six atoms. (Taken from W. Shockley, 'Electrons and Holes in Semiconductors', Princeton, D. Van Nostrand Co., Inc., 1950)

(B) Schematic band diagram, density of states, and Fermi-Dirac distribution function for an intrinsic semiconductor at thermal equilibrium.
At ordinary temperature, only very few electrons are excited into conduction band.

A.

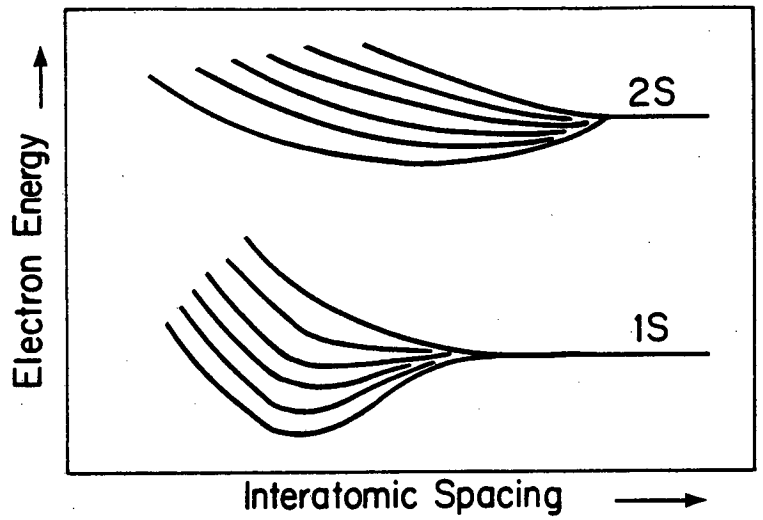

B.

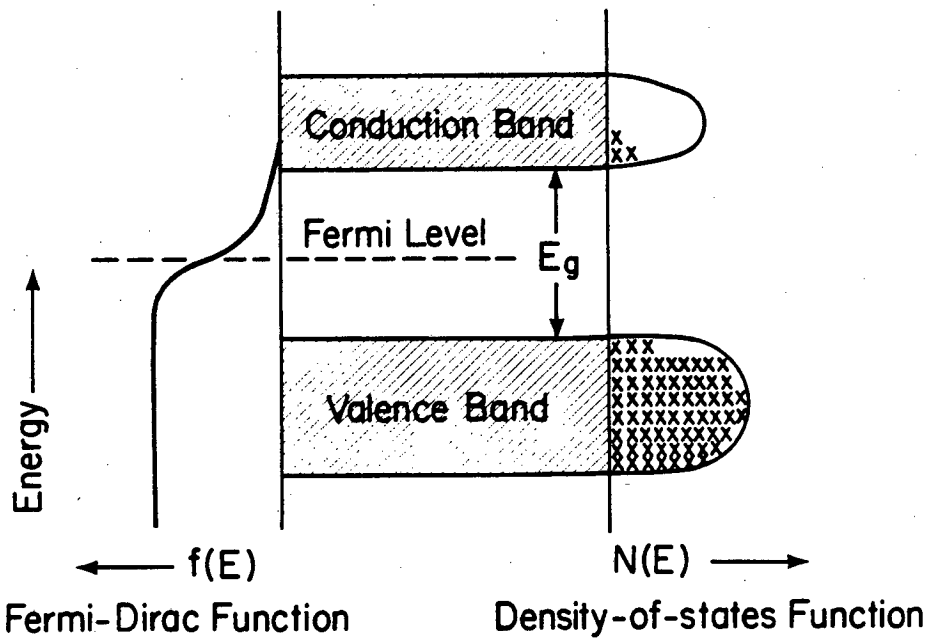

XBL 819-4686

In the case of a metal, because the highest occupied energy band is half empty, electrons are free to drift when they are subjected to an electric field. As for an insulator, the highest occupied energy band, usually called valence band, is filled with electrons and the next available empty band, called the conduction band, is well separated by a large band gap, Eg, so that only a negligible number of electrons can be thermally excited from the valence band into the conduction band at a normal temperature and, consequently, the conductivity is exceedingly small. In between these two types of solids, the semiconductor, with the valence bands filled but having a narrower band gap, possesses a noticeable number of electrons in its conduction band either excited by thermal energy or by photons in the infrared or in the visible region. Upon excitation, not only the electrons in the conduction band serve as charge carriers; the vacancies, or holes, left in the valence band may also function to conduct electricity. Generally, the mobilities of these two charge carriers are quite different from each other [8].

If a semiconductor has conductivity caused by only the two aforementioned modes of excitation, it is an intrinsic type. Several lattice defects contribute extrinsic conductive property to a semiconductor. The most common one is impurity doping produced by introducing electron acceptors or donors into the lattice, as the way n-type or p-type silicon is manufactured. Others are the Frenkel defect and Schottky defect. A Frenkel defect is caused by some atoms leaving their lattice sites and squeezing into positions which are not lattice points called interstitial sites. Schottky defect is caused by an excess or a deficiency of constituents.

Since the lattice defects are more-or-less isolated from each other, they add new energy levels but not continuous bands into a solid. Some energy levels, which are closer to the conduction band and whose dopants can be easily ionized to provide conductive electrons, are called donor levels. Some are acceptor levels, since they receive thermally excited electrons from valence band and thus generate the hole carriers. These levels modify the density-of-energy-state function N(E) and shift the Fermi level of an intrinsic semiconductor. Excess doping of a semiconductor with electron donors makes it n-type. The schematic band diagram, Fermi-Dirac distribution function, N(E) and carrier concentrations are shown in Figure 2 [9]. At thermal equilibrium, the filling of these dopant levels follows the Fermi-Dirac distribution function.

5.2.2. ELECTROCHEMISTRY OF ZINC OXIDE

Because polycrystalline Zinc Oxide was investigated in this study, some of its characteristics are discussed here. ZnO is a semiconductor with a band gap of 3.2 eV. Its photo-conductivity can be observed easily only in the ultra-violet region, $\lambda < 400$ nm. ZnO is crystallized in a hexagonal wurtzite lattice, in which the oxygen ions are arranged in closest hexagonal packing and the zinc ions occupy half of the tetrahedral interstitial positons and have the same relative arrangement as the oxygen ions (Figure 3A). As ZnO powder is prepared by vapor deposition without intentional doping, it is always a n-type semiconductor because of the interstitial Zinc atoms within the lattice [10]. The band diagram of non-stoichiometric ZnO is shown in Figure 3b. An allowed level, which is associated with the excess zinc, is located within the band gap approximately 0.05 eV below the bottom of

Figure 2. Schematic band diagram, density of states, Fermi-Dirac distribution function, and the carrier concentrations for a n-type semiconductor at thermal equilibrium.

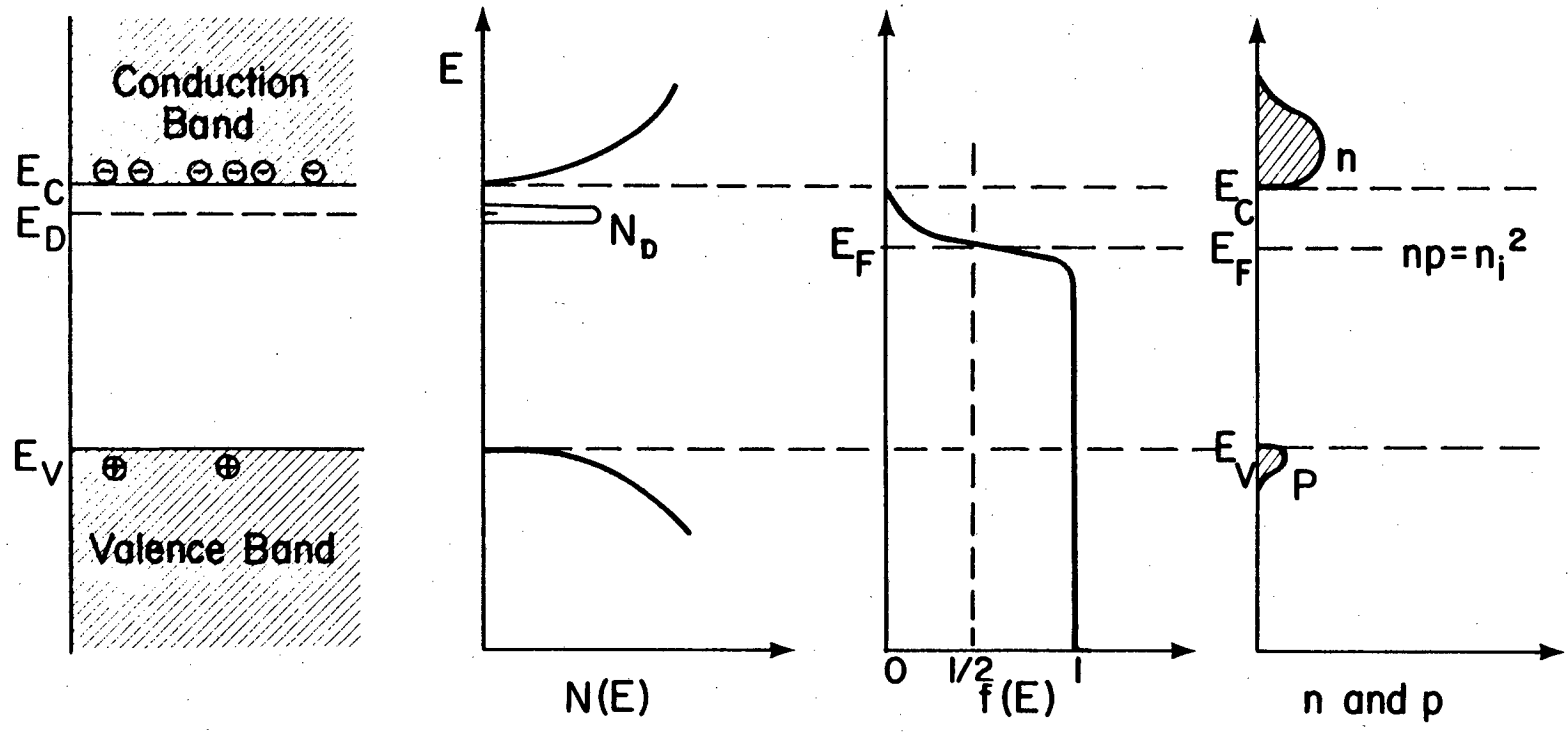

N-type Semiconductor

XBL 819-4685

Figure 3. (A) The hexagonal wurtzite lattice of ZnO.

Larger circle: O

Smaller circle: Zn

(B) Schematic energy diagram of ZnO near the solid surface. Some electrons are trapped on the surface either by surface states or adsorbed molecules at thermal equilibrium.

Zn_i represents the interstitial zinc atom.

E_g is the band-gap energy.

A.

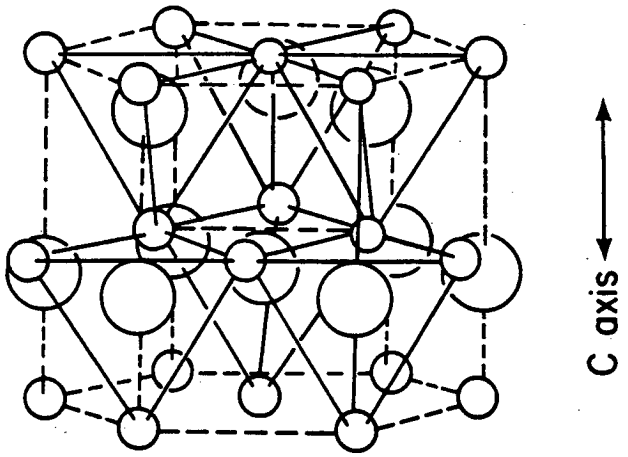

B.

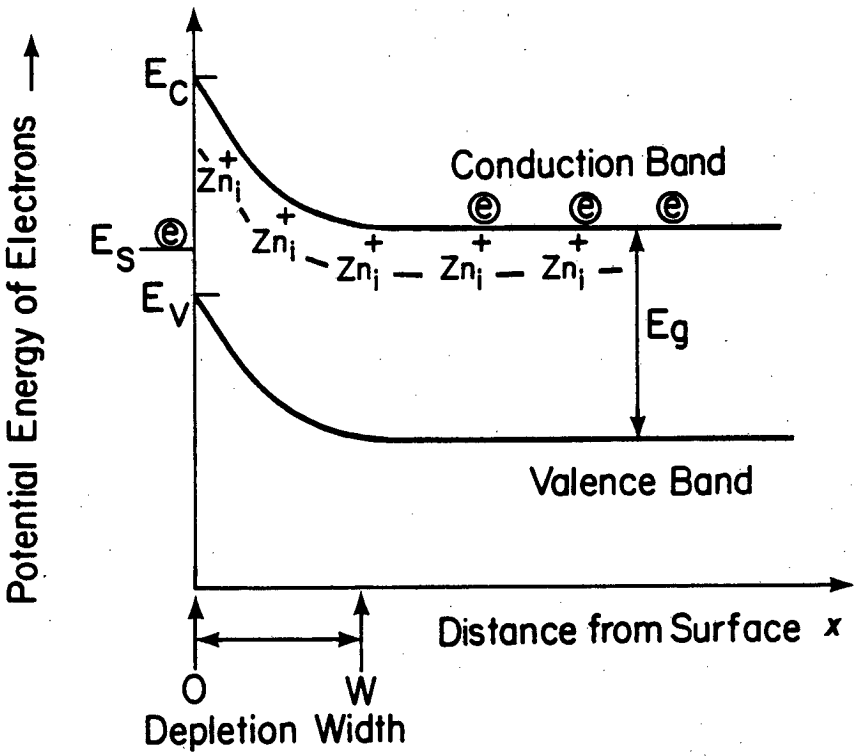

XBL 819-4684

the conduction band. In the dark, the conductive electrons originate almost exclusively from these shallow donor levels, since the probability of thermal excitation across a large band gap is very small at room temperature [11].

Most of the bulk properties of semiconductors can be easily understood when this simple energy band diagram is recalled. But, when studying the physics of semiconductor devices or liquid-junction solar cells, one must have a thorough understanding of the effects of the surface state and the distribution of charge and potential at the interface. Because of the discontinuity of a lattice structure right on surface, surface atoms have unsaturated bonds and thus different energy states. These surface states may act as traps for charge carriers, or they may interact with some foreign molecules and then also form traps. In either case, a semiconductor by itself develops an electric field and band-bending near the surface, as shown in Figure 3B. The physical picture of a typical n-type semiconductor electrode when immersed in an aqueous solution under anodic bias is shown in Figure 4A [12].

The conventional energy-band presentation is shown in Figure 4B, where the potential drops across the interface may be subdivided into three parts, namely, in the dense part of the ionic double layer, also called Helmholtz layer, in the space-charge region inside the semiconductor and in the diffuse part of the double layer in the electrolyte, known as Gouy layer. The Helmholtz layer consists mainly of oriented solvent dipoles and some strongly adsorbed ions. Both in the ionic diffuse layer and in the space-charge layer, the equilibrium concentrations of charge carriers are determined by two opposing

Figure 4. (A) Schematic diagram of charge distribution near the surface of a n-type semiconductor when it is anodically biased.

It shows also the dielectric and adsorbed ions in the double layer located at interface.

(B) The conventional energy-band diagram shows the distribution of potential [$\phi(x)$] at the semiconductor-electrolyte interface. ✱ is the ionized electron donor site localized in the space-charge layer.

In this n-type semiconductor, the concentration of holes near the surface is very small at thermal equilibrium.

E_c, E_v, and E_F are the energies at the bottom of conduction band, at the top of valence band, and at Fermi level, respectively. E_{FB} is the fermi level at flat band condition. E_c^o is the E_c when at flat-band condition.

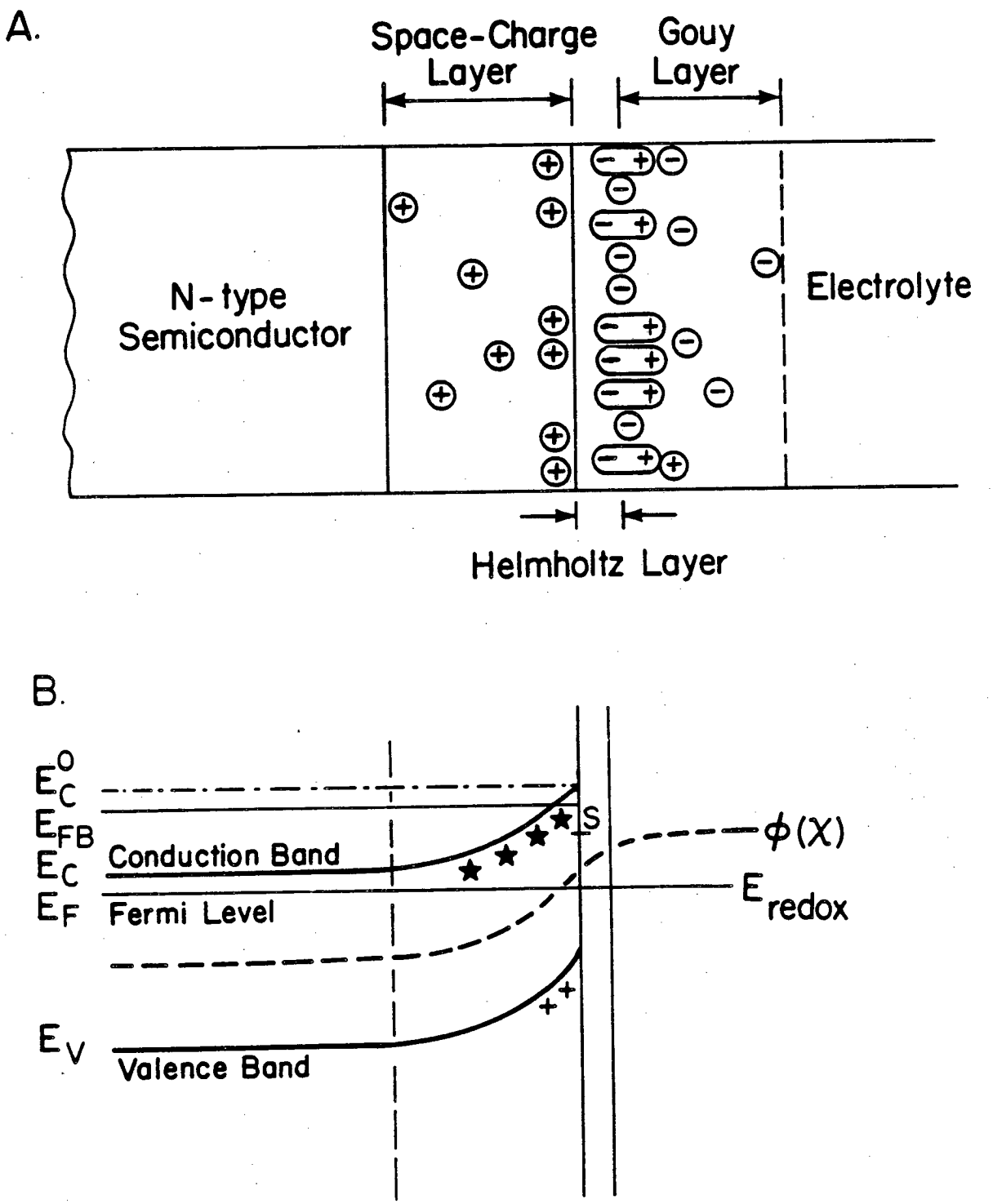
A.
Space-Charge Layer
Gouy Layer
N-type Semiconductor
Electrolyte
Helmholtz Layer
B.
E_C^0
E_{FB}
E_C
Conduction Band
E_F
Fermi Level
E_V
Valence Band
S
$\phi(X)$
E_{redox}

XBL 819-4683

forces, the thermal motion of these carriers and the electric field either intrinsic or applied externally.

The quantitative relation between charge and potential distribution can be solved by starting with the Poisson equation

$$\frac{d^2\phi(x)}{dx^2} = -\frac{\rho(x)}{\epsilon}$$

where $\phi(x)$ is the potential at x, $\rho(x)$ is the charge density, and ϵ is the dielectric constant of medium. The charge density at point x in a semiconductor is expressed as

$$\rho(x) = e\,[-n(x) + p(x) + N_D - N_A]$$

where N_D and N_A are the concentrations of donor levels and acceptor levels. In this equation, it is assumed that the donors and acceptors are completely ionized. At thermal equilibrium, the concentrations of the free carriers in a semiconductor follow the Boltzmann distribution function, so

$$n(x) = n^o \exp\left[\frac{e[\phi(x) - \phi_B]}{kT}\right]$$

$$p(x) = p^o \exp\left[\frac{-e[\phi(x) - \phi_B]}{kT}\right]$$

where n^o, p^o and ϕ_B are the concentrations of electrons and holes, and the potential in the bulk of semiconductor, respectively. A detailed derivation under several boundary conditions is given by Myamlin and Pleskov [13]. Two important conclusions from the derivation used for this study are the following:

a. In an electrochemical cell consisting of a moderately doped semiconductor and an aqueous solution with at least 0.01 N of added salt, the electric potential across the semiconductor-electrolyte interface drops mainly in the space-charge layer.

b. The differential capacitance, which is defined as

$$C = \frac{dQ}{d\phi_{12}}$$

where $\phi_{12} = \phi_c - \phi_B$ is the total potential drop across the phase boundary, ϕ_C is the potential in the bulk of the electrolyte, and Q is the total charge on each side of this 'capacitor', is determined by a series of capacitors across the solid-liquid interface. With a lightly, or moderately doped semiconductor, C is determined by the capacitance C_1 of the space charge layer in a semiconductor because C_1 is the smallest part among the series. A Mott-Schottky plot of C_1^{-2} versus the applied bias then provides the flat-band potential V_{fb} and the dopant concentration. V_{fb} is the particular electrode potential when there is no energy band bending from the interior of the solid up to the surface, as shown in Figure 4B.

In solid-state physics, the potential E is always referred to the level of an electron in a vacuum. When dealing with electrochemistry, however, chemists generally use a standard hydrogen electrode as a convenient reference. These two scales are correlated by [14]

$$E = -4.5 - e\,U$$

where U is the conventional electrochemical reduction potential.

When ZnO is exposed to UV light, the photo-generated holes are swept to the surface of the semiconductor by its built-in potential, and they cause both electrochemical dissolution of the surface and oxygen evolution. The mechanism is described as follows [15].

$$2\ ZnO + 4\ h^+ \longrightarrow 2\ Zn^{2+}_{(aq)} + O_{2(g)}$$

$$4\ OH^- + 4\ h^+ \longrightarrow H_2O + O_{2(g)}$$

In order to use this semiconductor material for solar cells and to

overcome its instability, efforts in the past years were concentrated on the dye-sensitization process [16]. However, the dye-sensitized process can be effective only for the first one or two monolayers of dye. Further deposition of dye causes an increase of resistivity and no enhanced photocurrent. Realizing this difficulty, Tsubomura has succeeded in raising the quantum yield to 1.5% energy conversion by using a porous ZnO electrode [17]. Our initial attempt was to adopt this new approach and sensitize ZnO by some stable dyes which are capable of oxidizing water after its photo-oxidation.

5.3. EXPERIMENTAL

A. Sample preparation

Sintered pellets of ultrapure grade zinc oxide (Alfa Inorganics) were prepared similarly to the technique used by McGregor[5]. ZnO powder was pre-dried at 60°C in a vacuum oven overnight and pressed into pellets of 1 mm in thickness and 1.32 cm in diameter at 740 $kg \cdot cm^{-2}$. Then, these pellets were sintered at 1100°C for 16 hours in air and doped with zinc by heating the sintered disc in a pyrex ampoule sealed together with excess zinc metal at 10^{-5} torr for 24 hours at 580°C. Before each experiment, the pellet was etched for 5 minutes in concentrated H_3PO_4 followed by a wash with doubly de-ionized water, a 10 second dip in 0.32 M HCl and a final water rinse. Electrical contacts to these pellets were provided with silver epoxy paste and a copper wire.

Dyed-ZnO polycrystalline pellets were first fabricated as above. However, after etching, the pellet was resealed in a pyrex ampoule with 30 mg reagent-grade phthalonitrile (Eastman Kodak). The degree of surface coloration depended on the duration of heating at 170°C. Usually, a visible faint blue-green color developed evenly on the surface in two hours.

A few experiments were carried out with CdS single crystals. Before each run, CdS was polished with $1\mu Al_2O_3$ and etched in 3 N HCl solution for one minute. Then, it was fitted into the photoelectrochemical cells consisting of aerated pH 7, 1 N KNO_3 aqueous solution and a platinum wire as the counter electrode. CdS cells with the surface coated by a thin film of manganese porphyrin were prepared by the vacuum deposition method. The thickness of the thin film was

determined by a Kronos thickness monitor Model QM-311.

B. Photo-electrochemical characterization

The photocurrent was measured under the potentiostatic condition with a Princeton Applied Research (PAR) 173 potentiostat and a Beckman saturated calomel electrode (SCE). Platinized Pt was used as the counter electrode. Solutions were prepared with doubly deionized water and buffered either by phosphate or by borax. They all contained 1 M KNO_3 as the supporting electrolyte. Light from a 450 W Xenon lamp was monochromatized by a Bausch and Lomb 33-86-07 monochromator. The light beam was modulated at about 5 hertz and the photocurrent was detected using a PAR HR-8 lock-in amplifier to remove the dark current. The differential capacitance at the semiconductor-electrolyte interface was measured with a universal bridge (General Radio 1650A) at a frequency of 1 kHz. Schematic diagrams of the set-up are shown in Figure 5 and Figure 6.

Constant voltage coulometry with a PAR 179 digital coulometer was carried out on both dyed and undyed ZnO pellets. After UV irradiation, aqueous solutions in contact with ZnO electrodes were collected, and the concentrations of zinc ions were analyzed by a Perkin-Elmer Atomic Absorption Spectrometer, Model 360.

Figure 5. The experimental apparatus used in the measurement of photocurrents. M: monochromator, F:filter, C:chopper, ND: neutral density filter, BS: beam splitter, I_{ph}: photocurrent, I_{tot}: the sum of I_{ph} and dark current. A simplified circuit diagram is shown in the bottom figure.

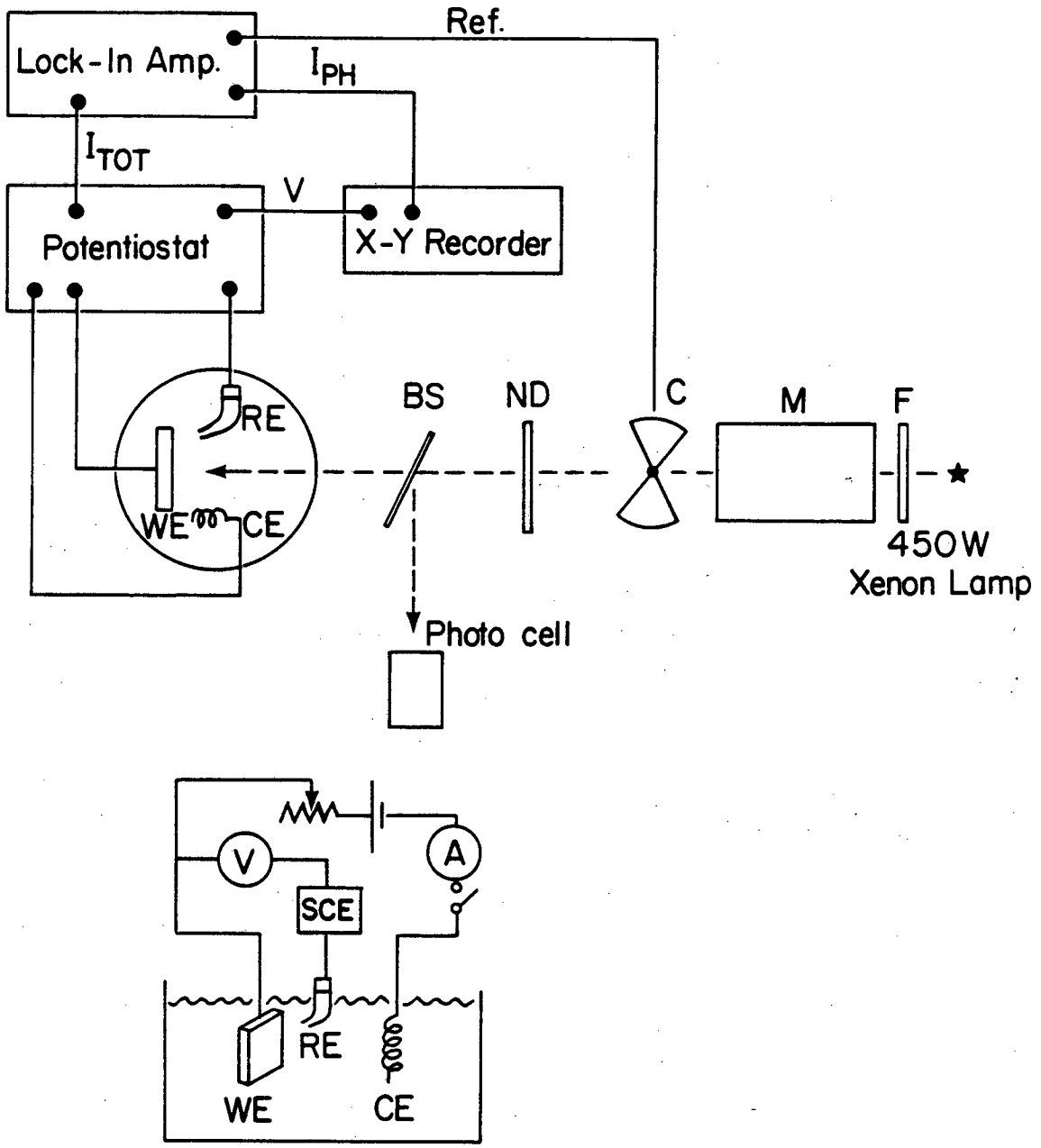
Ref.
Lock-In Amp.
I_{PH}
I_{TOT}
V
Potentiostat
X-Y Recorder
RE
WE
CE
BS
ND
C
M
F
450W
Xenon Lamp
Photo cell
V
A
SCE
RE
WE
CE

XBL 819-4682

Figure 6. Schematic diagram for capacitance measurements. A bias supplied by the dry cell is internally imposed on the circuit by the impedance bridge.

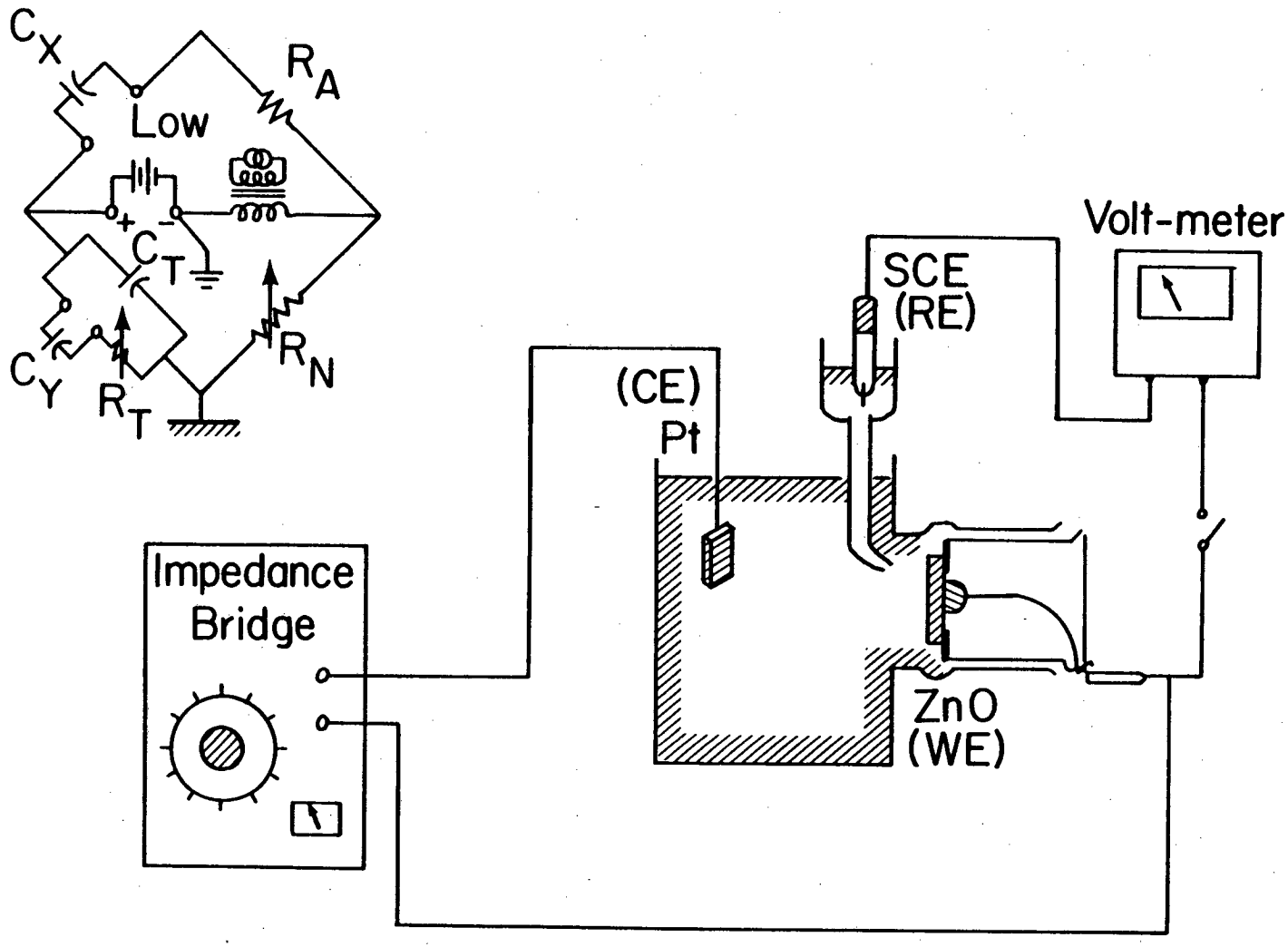
C_X
R_A
Low
C_T
C_Y
R_T
R_N
Volt-meter
SCE
(RE)
(CE)
Pt
Impedance
Bridge
ZnO
(WE)

XBL 819-4681

5.4. RESULTS AND DISCUSSION

The physical properties of sintered ZnO pellets were similar to those determined previously [5], yet some additional properties were noted. As previously reported, pellets prepared without further doping had resistivities larger than 10^8 ohm-cm and about 100 ohm-cm when doped with excess zinc. In this study, the density of sintered pellets is found to be only 56% of the value calculated from X-ray diffraction measurement [18]. This suggests that the pellets are very porous and, consequently, a large dark current results. The highly adsorptive nature of dyestuff on these pellets is due to the hydrophilic surface of ZnO and the high porosity, which allows the dye solutions to penetrate into the interior easily. This is supported by the scanning electron micrograph. Figure 7 shows a very convoluted surface structure. Although this kind of rough surface is essential to achieve a high quantum yield for the sensitized photocurrent of ZnO [19], a more compact surface is certainly more desirable when the protection of surface is concerned. After pellets were dyed with phthalonitrile, ZnPc spread all over the surface and inside of these pellets. In some cases, excess coverage of dye decreased the conductivity dramatically.

Figure 8 shows the dependence of the quantum yield of photocurrent versus the applied potential on both dyed and bare ZnO. The photocurrent of dyed ZnO saturates rapidly as compared to that of a bare ZnO. Two explanations are considered. One is that the number of defects or recombination centers in the space-charge region in dyed ZnO is considerably smaller than that in the undyed ZnO. The other is that the concentration of donors is higher in bare ZnO. This decreases the depth of the space-charge layer in bare ZnO and causes a higher pro-

Figure 7. Scanning electron micrograph of a sintered ZnO.

1 μ

Figure 8. Quantum efficiency of photocurrent versus applied potential on sintered ZnO in 1 N KNO_3 aqueous solutions buffered at pH 10. (A) dyed, (B) bare.

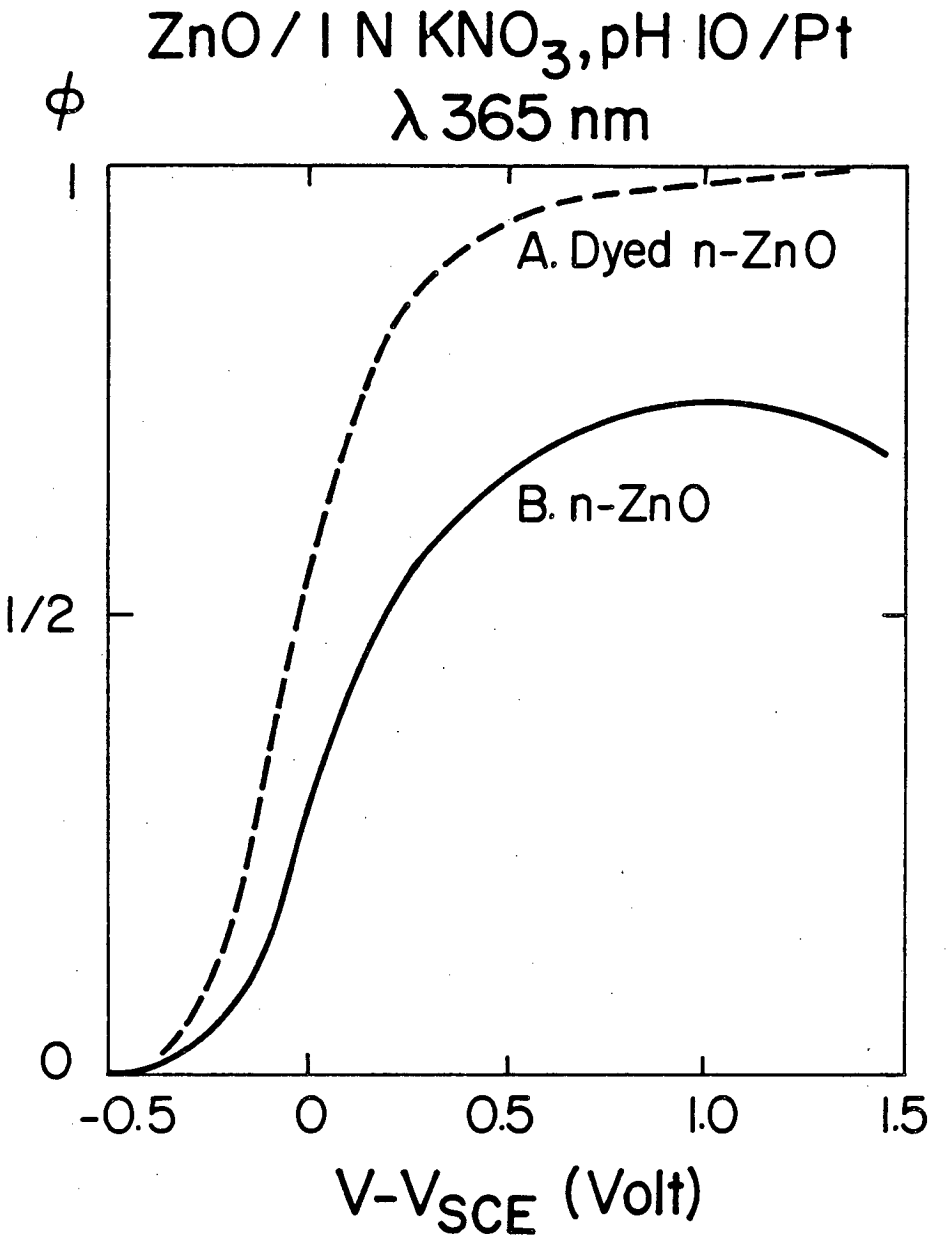
ZnO / 1 N KNO3, pH 10 / Pt
λ 365 nm
φ
1
1/2
0
A. Dyed n-ZnO
B. n-ZnO
-0.5
0
0.5
1.0
1.5
V-VSCE (Volt)

XBL 819-4680

bability of the back tunneling of electrons to recombine with holes on the surface. Both explanations are consistent with the present experimental results.

The spectral response of the sintered semiconductors is shown in Figure 9. Dyed ZnO extends its action spectrum slightly towards longer wavelength when compared with that of a single crystal. No noticeable sensitized photocurrent was detected in the region where ZnPc absorbed light. The variation of the onset potentials at different pH's is shown in Figure 10. This variation is a result of the amphoteric dissociation of -ZnOH surface group [15]. Normally, an undyed single crystal of ZnO has a slope of -0.059 Volt/pH unit. This is not the case here. The ZnPc apparently modifies the sensitivity of the surface to external pH changes. Theoretically, the onset potential of photocurrent should be the same as the flat-band potential. At the flat-band potential, there is no band bending near surface to separate the electron-hole pairs generated by band-gap illumination. If the surface coating shifts the flat-band potential in the right direction, as may be the situation here, this will greatly improve the performance of semiconductors in energy conversion.

To examine the band model of polycrystalline dyed ZnO, electron transfer processes at the interface are studied with cyclic voltammetric technique. Because the concentration of holes at the surface is very small in the dark for a n-type semiconductor and the electron tunneling from aqueous solution into the conduction band is prevented by a large potential barrier, negligible oxidation of water is observed up to +1.5 Volts (versus SCE), as is shown in Figure 11a. On the other hand, the reduction of water and other chemicals in the solution starts

Figure 9. The spectral response of ZnO.

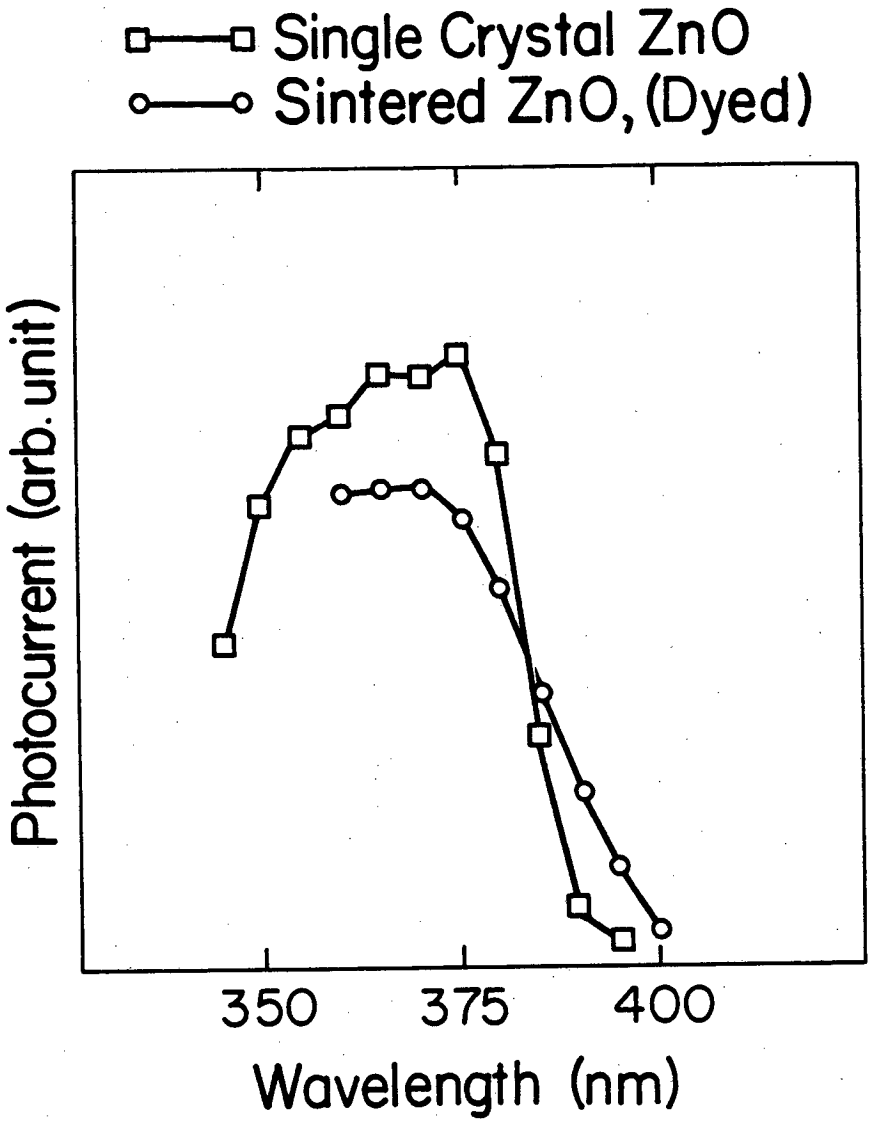
Single Crystal ZnO
Sintered ZnO, (Dyed)
Photocurrent (arb. unit)
350
375
400
Wavelength (nm)

XBL 819-4679

Figure 10. The variation of photocurrents at three different pHs in aqueous solutions.

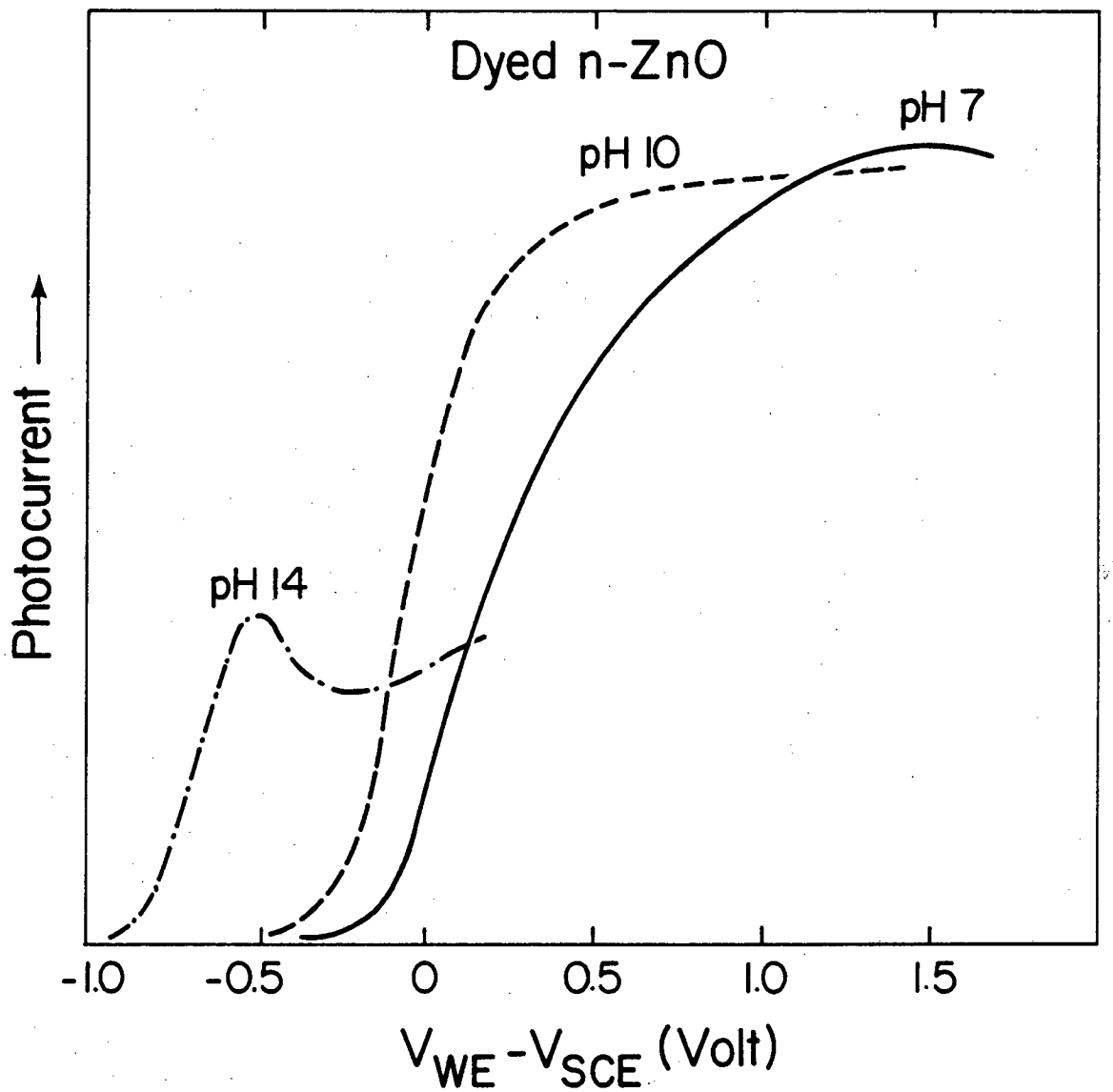
Dyed n-ZnO
pH 7
pH 10
pH 14
Photocurrent
-1.0
-0.5
0
0.5
1.0
1.5
$V_{WE} - V_{SCE}$ (Volt)

XBL 819-4678

Figure 11. Cyclic voltammograms of sintered dyed-ZnO in 1 M KNO_3 aqueous solution (pH 10). Sweep rate: 200 mV/sec.

(a) 0 M $Fe(CN)^{3-}$,

(b) and (c) 1.2 mM $Fe(CN)^{3-}$

All solutions are in the dark. 1 indicates the first scan, and 2 is the second scan. (b) and (c) are of the same kind of voltammetric scans except in the slightly different potential ranges.

The small well-behaved cyclic voltammogram in (c) is with a platinum electrode.

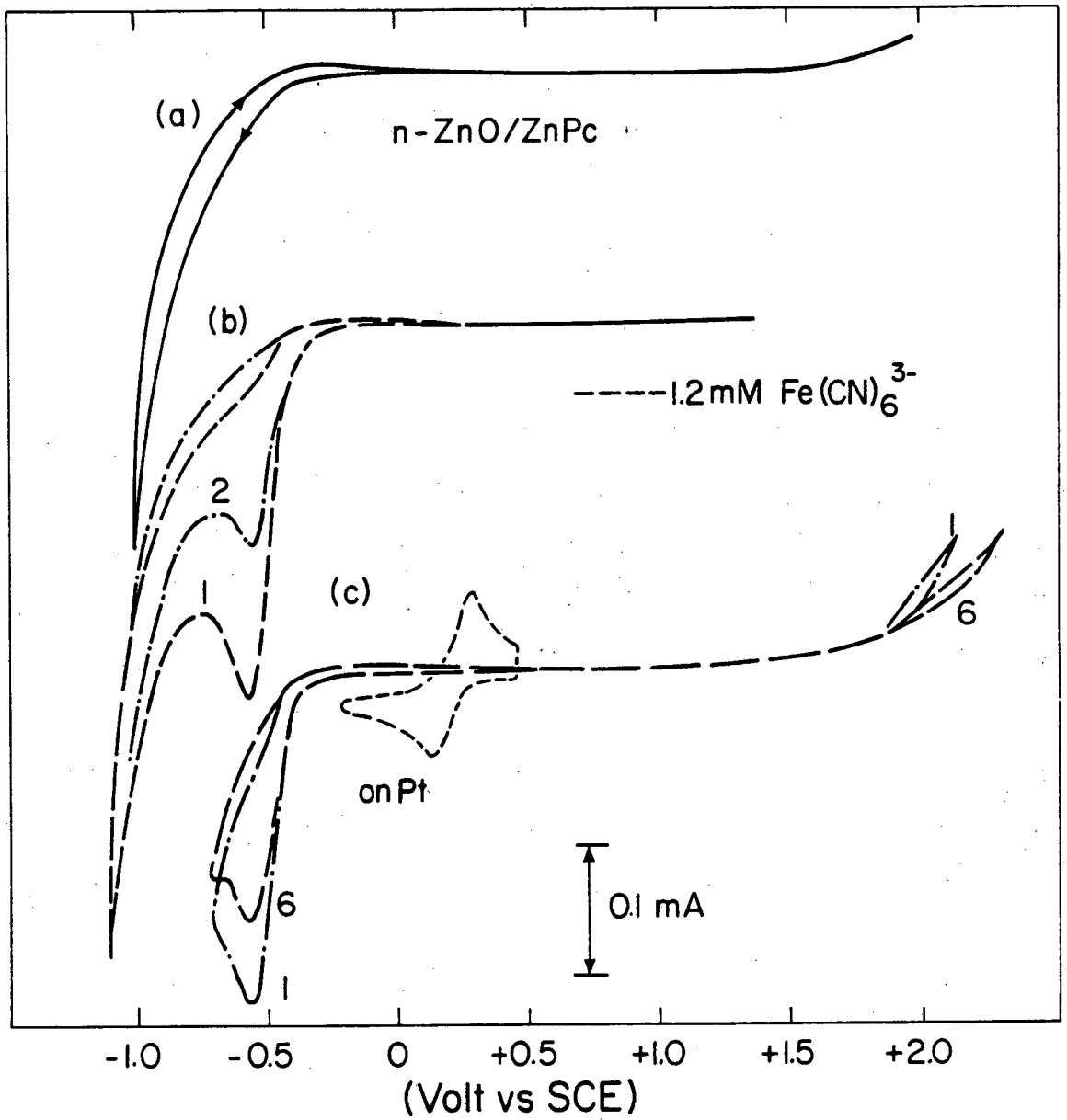
(a)
n-ZnO/ZnPc
(b)
----1.2 mM Fe(CN)$_6^{3-}$
2
1
(c)
1
6
on Pt
6
1
0.1 mA
-1.0
-0.5
0
+0.5
+1.0
+1.5
+2.0
(Volt vs SCE)

XBL 819-4675

readily at about on-set potential. With the addition of ferricyanide, reduction of $Fe(CN)_6^{3-}$ at a potential just below the flat-band potential is observed. However, no oxidation of $Fe(CN)_6^{4-}$ shows up until a very positive potential is applied (Figure 11b). This kind of redox behavior indicates the operation of a band model in such a sintered dyed ZnO electrode, as is schematically shown in Figure 12. On the contrary, two well-defined redox waves are observed in the cyclic voltammogram of $Fe(CN)_6^{3-}$ on a Pt wire (Figure 11c). This demonstrates that many features of the single crystal material with a direct band-gap are retained by its polycrystalline substrate. But the important points here are that the polycrystalline electrode is cheaper and easier to fabricate, and a good junction can be spontaneously formed between an aqueous solution and the semiconductor. However, in order to achieve a high efficiency with a polycrystalline material, the grain dimension and the thickness of the depletion layer must match the light absorption length, and the resistivity of the boundaries between grains must be low enough to conduct electronic flow [20]. To fulfill these requirements, a simple hydrolytic pressing and high temperature sintering were adopted here.

A similar experiment was performed with the bare sintered ZnO. One notices that the cathodic and anodic waves get closer in water as compared to a dyed ZnO (Figure 13a). The surface changed irreversibly during the excursion, as was shown by the shift of the first scan to the eighth scan. This might involve the oxidation of Zn atoms and loosely bound O_2^-, or some impurities adsorbed on the surface. With the addition of ferricyanide, two additional peaks are observed. These waves are not reversible in an electrochemical sense, whereas a

Figure 12. Schematic energy level diagrams of sintered ZnO immersed in an aqueous solution containing $Fe(CN)^{3-}$ and $Fe(CN)^{4-}$ couple. (a) at equilibrium, (b) under anodic bias, (c) under cathodic bias.

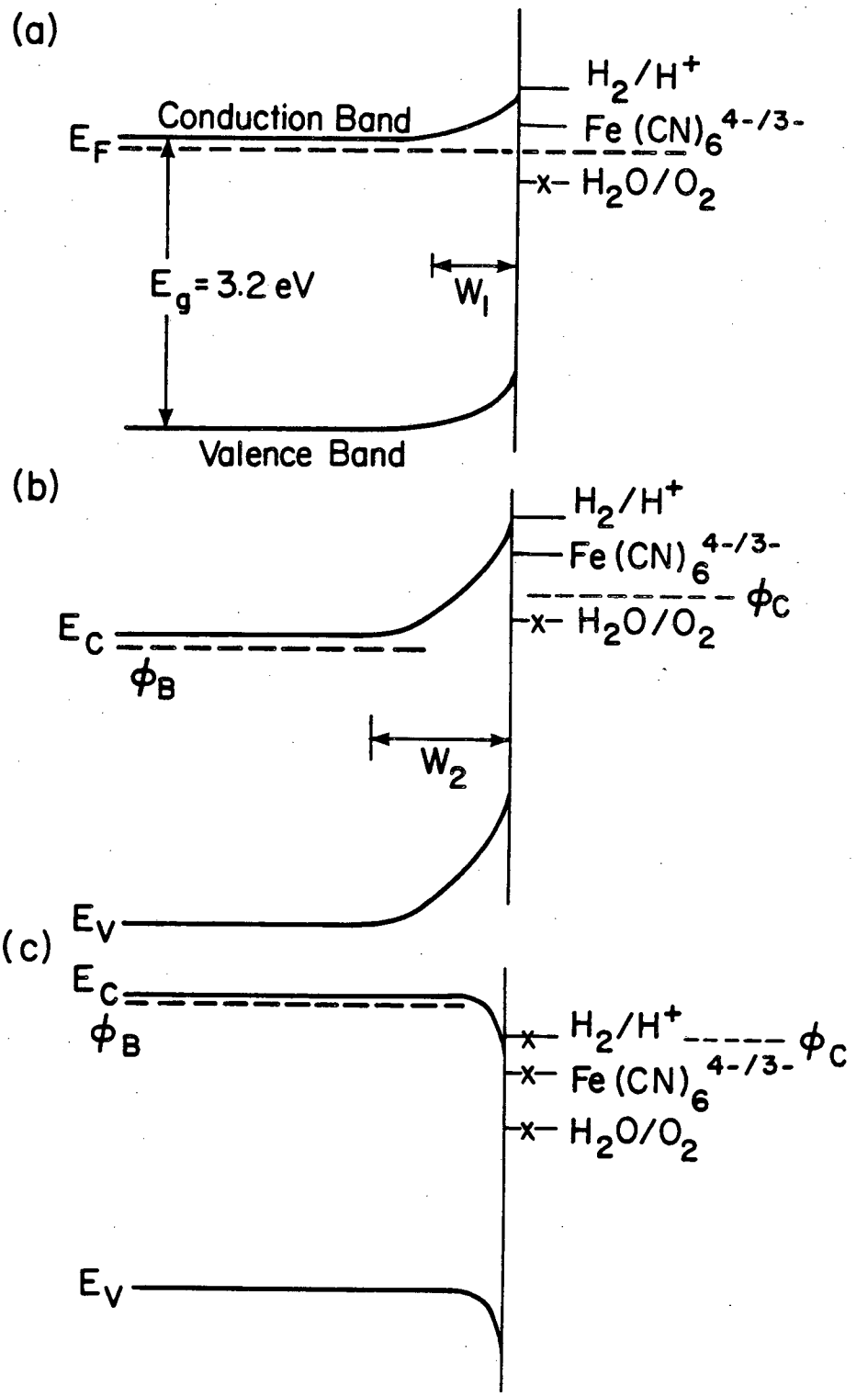
(a)
Conduction Band
E_F
H_2/H^+
$Fe(CN)_6^{4-/3-}$
H_2O/O_2
$E_g = 3.2$ eV
W_1
Valence Band
(b)
H_2/H^+
$Fe(CN)_6^{4-/3-}$
ϕ_C
H_2O/O_2
E_C
ϕ_B
W_2
E_V
(c)
E_C
ϕ_B
H_2/H^+
ϕ_C
$Fe(CN)_6^{4-/3-}$
H_2O/O_2
E_V

XBL 819-4676

Figure 13. Cyclic voltammograms of sintered bare ZnO in pH 10, 1 M KNO_3 aqueous solutions. (a) and (b) were with different sintered pellets, and were run in the dark. Figure to the right hand side of (a) was with the same electrode as (a) except the experiment was run one day later. All experiments were with 1.2 mM $Fe(CN)_6^{3-}$.

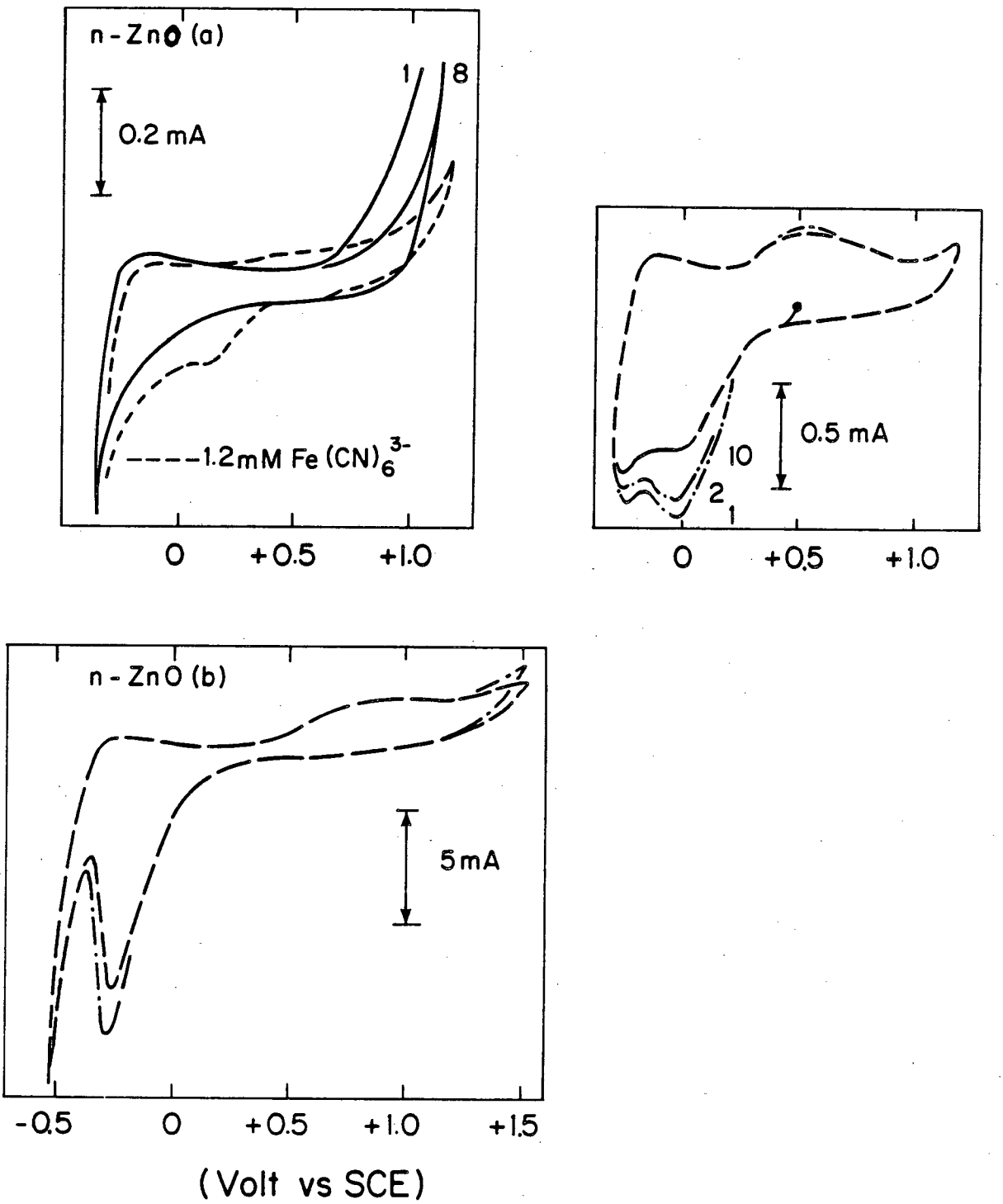
n-ZnO (a)
0.2 mA
1
8
----1.2mM Fe (CN)$_6^{3-}$
0
+0.5
+1.0
0.5 mA
10
2
1
0
+0.5
+1.0
n-ZnO (b)
5mA
-0.5
0
+0.5
+1.0
+1.5
(Volt vs SCE)

XBL 819-4674

reversible single electron redox couple has two peaks spaced by 0.059 volts. Additional voltammograms with another sintered bare ZnO are also shown in Figure 13b. Why can one observe these small re-oxidation peaks of $Fe(CN)_6^{4-}$ in Figure 13, but not in Figure 11 with dyed ZnO? Again, because the concentration of donors in a bare ZnO is higher, electrons have a higher probability to tunnel through the thinner barrier in space-charge layer. In addition, the number of the surface states and defects may be higher in undyed ZnO to facilitate electron transport. The higher dark current in Figure 13b is due to a continuous penetration of aqueous solution into these porous discs and thus the increasing contact surface. It has nothing to do with the concentration of defects and surface states, as illustrated by the wider space between the anodic and the cathodic curves in Figure 13b as compared to that in Figure 13a.

The existence of defect states and a higher concentration of dopants is reinforced by the measurements of differential capacitance in these two kinds of sintered ZnO. From Mott-Schottky plots (Figure 14),

$$C^{-2} = \frac{2}{q \varepsilon_s N_D} \left(V - V_{fb} - \frac{kT}{q} \right)$$

the density of donors in the bare ZnO is measured to be $6.4 \times 10^{20}/R^2$ cm^{-3}, and that in dyed ZnO is $1.0 \times 10^{20}/R^2$ cm^{-3}, where C is the differential capacitance ($F \cdot cm^{-2}$), q is the charge on an electron (1.6×10^{-19} C), ε_s is the dielectric constant of the semiconductor ($F \cdot cm^{-1}$) and N_D is the donor density (cm^{-3}); V is the biased potential (volt), V_{fb} is the flat-band potential, k is the Boltzmann's constant and T is the absolute temperature. Because the surface is so rough, only the apparant surface area can be measured, and R must be introduced as the

Figure 14. Mott-Schottky plots [$1/C^2$ vs V_{ZnO}] for (A) □—□ and △—△, undyed but sintered ZnO and (B) •—•, dyed and sintered ZnO. Both at a frequency of 1 kHz and in 1 N KNO_3, pH 10 aqueous solutions. The counter electrode is a platinized platinum electrode.

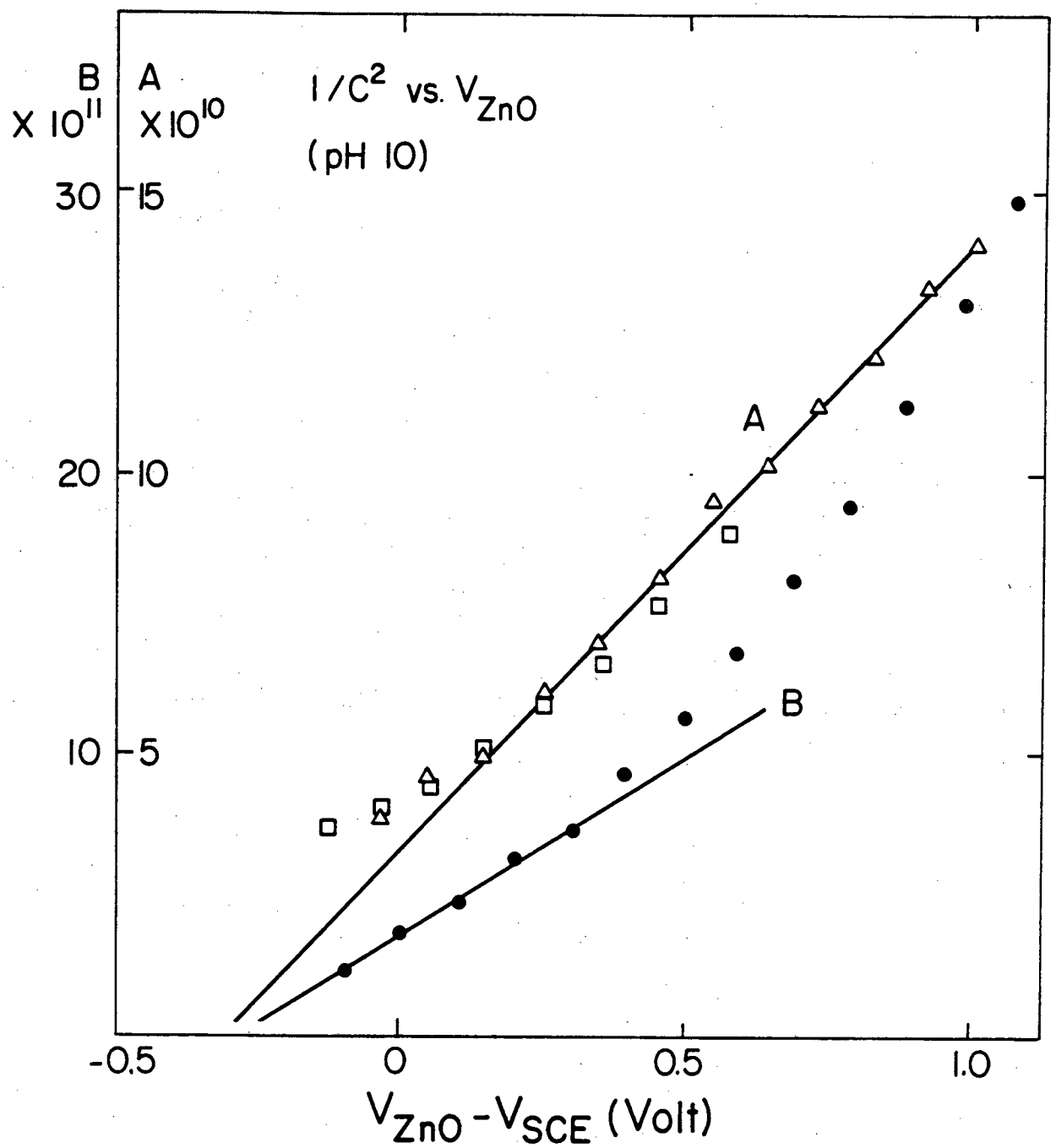
B
X 10^11
A
X 10^10
1/C^2 vs. V_ZnO
(pH 10)
30
15
20
10
10
5
A
B
-0.5
0
0.5
1.0
V_ZnO - V_SCE (Volt)

XBL 819-4687

ratio of the real surface area to the apparent surface area. For a concentration of the donors equal to 10^{20} cm^{-3}, the thickness of the space-charge region is calculated to be 36 Å [21]. With some surface states and interband defects, electron can easily hop across the surface barrier in addition to the moving by quantum-mechanical tunneling.

After having some feeling about the physical nature of these sintered ZnO electrodes, we then asked whether the surface was actually protected from photo-dissolution by the thin chemisorbed ZnPc. This problem was first attacked by exposing the ZnO electrode to UV light and measuring the concentration of zinc ions that appeared in the aqueous solution under constant bias potential. Data obtained from constant voltage coulometry and atomic absorption spectrometry are summarized in Table 1. It is clear at this point that neither bare nor dyed ZnO electrodes buffered at pH 10 show any significant dissolution. This is not consistent with results reported previously by McGregor [5]. Since bare ZnO does dissolve under band-gap illumination, this result can be interpreted only as a precipitation of zinc ions on the highly convoluted surface. At pH 14, a large excess of zinc ions with respect to the charge passed was observed for both dyed and bare ZnO. These zinc ions might come from some surface dissolution and mostly from loosely bound ZnO powders. Changing the buffers used in the contacting solutions and using a more compact ZnO electrode should clarify some of these suppositons.

Can an oxidized ZnPc oxidize water to form oxygen? The redox potential of $ZnPc^{+}/ZnPc$ is +0.68 volt versus SCE [23]. Such a redox potential is generally not high enough to oxidize water unless with

TABLE 5 - 1

SUMMARY OF THE RESULTS FROM A.A. MEASUREMENTS

AND COULOMB COUNTS FROM CONSTANT VOLTAGE COULOMETRY [a,b]

#	TYPE [c]	pH	COULOMB COUNT (C)	$[Zn^{2+}]$*(ug/ml)	$[Zn^{2+}]_{meas}$(ug/ml)
1	DYED-ZnO (faint)	10	6.012×10^{-2}	3.310	0.050 ± 0.020
2	DYED-ZnO	10	8.046×10^{-2}	4.432	0.038 0.050
3	n-ZnO	10	4.516×10^{-2}	2.233	0.000 0.020
4	n-ZnO	10	8.181×10^{-2}	4.016	0.016 0.015
5	DYED-ZnO	10	8.949×10^{-2}	4.592	0.006 0.020
6	DYED-ZnO (dark)	10	0	0	0.000 0.020
7	DYED-ZnO	7	4.043×10^{-3}	0.201	< 0.1
8	DYED-ZnO	14	2.0×10^{-2}	1.004	~ 110
9	DYED-ZnO (faint)	14	2.0×10^{-2}	1.011	~ 98
10	DYED-ZnO	14	2.002×10^{-2}	0.997	~ 57
11	DYED-ZnO	10	2.001×10^{-2}	0.874	< 0.02
12	n-ZnO	14	2.011×10^{-2}	0.973	~ 56

a. All the experiments were carried out in air-saturated solutions.

* Assuming that all current was used to dissolve ZnO surface.

b. The potentials of ZnO were all biased at 0.0 V vs SCE.

c. The color of dyed-ZnO is typically of blue-greenish. Two with (faint) mark indicate less coloration. One is highly colored.

some efficient oxygen catalyst present. In spite of this, the possibility that the chemisorbed ZnPc can be stabilized on a solid surface and at the same time be able to oxidize water at higher pHs certainly should not be excluded. Moreover, the nature of a monolayer of ZnPc assembly on a surface is expected to be different from that of an individual molecule floating in the solution.

Although there are doubts about whether the surface of ZnO is protected from photo-corrosion by ZnPc, some preliminary trials were carried out to apply the same principle to the smaller band-gap semiconductor CdS and silicon single crystal. These small band-gap semiconductors absorb a larger fraction of solar radiation, but they photocorrode rapidly when immersed in aqueous solution. For example,

$$CdS + 2\ h^+ \longrightarrow Cd^{2+} + S^\circ$$

$$Si + 4\ OH^- + 4\ h^+ \longrightarrow SiO_2 + 2\ H_2O$$

Both S° and SiO^2 left on the surfaces of the photo-corroded semiconductors act as an insulation layer and thus block the photocurrent.

In these trials, a thin layer of manganese porphyrin (Mn(TPP)OAc) was deposited on the surface of a CdS single crystal either by solvent sublimation or by vacuum deposition. Because only the surface protection was of the main interest, this thin layer was about 100 Å in thickness. Comparing the decay rates of the photocurrent between the protected and bare CdS electrodes, we found no obvious difference. In the mean time, Wrighton has derivatized the surface of a silicon crystal with ferrocene and succeeded in slowing down the photocorrosion rate [24]. Such a procedure apparently passivated almost all the surface active sites, whereas our coating method inevitably left some pinholes over the surface. This lesson suggests that only a

chemically prepared protecting layer will provide an adequate and extensively modified semiconductor surface for a photo-electrode. With some experience of preparing ZnPc-dyed zinc oxide, a Si single crystal covered with a chemisorbed SiPc layer was also manufactured, but no further study has been carried out yet. If this electrode can survive in an aqueous solution with a redox mediator, then with some oxygen catalyst deposited on the surface as small islands chemical fuel might be evolved under the sunshine.

In this study, our efforts have been focussed on the splitting of water into hydrogen and oxygen using a semiconductor as the photo-electrode. We have learned that a pressed and sintered polycrystalline material can be used as photo-electrode. Its instability can be improved by a chemically modified surface, and its depletion width can be varied by different levels of doping. Surface chemical treatment can on one hand modify the flat-band potential and on the other hand reduce the undesirable defects and recombination centers on the surface or on the grain boundary. In the future, stable molecules with high reduction potentials will be substituted for ZnPc to function both as a hole catcher and as an oxygen catalyst. Since a simple coating cannot be perfected, surface derivatization should be more favorable. An alternative approach is to use semiconductor powders as light absorber [25]. But, the intrinsic problems will be the same as those involved in the semiconductor solid electrode, i.e. the instability of powder under irradiation and the difficult selection of stable dyes used for sensitization. In these few years, significant advances have been made in research on coordination complexes suitable as the water splitting

catalyst. Immobilizing or attaching these complexes as a functional surface monolayer onto semiconductors should enable the liquid-junction cell to split water or to generate chemical fuel under solar radiation.

REFERENCES

1. A. Fujishima and K. Honda, Nature 238, 37 (1972).

2. A. J. Bard, J. Photochem. 10, 59 (1979).

3. B. A. Parkinson, A. Heller and B. Miller, Appl. Phys. Lett. 33, 521 (1978).

4. H. Maruska and A. Ghosh, Solar Energy 20, 443 (1978).

5. K. McGregor and J. Otvos, LCBQ-57, 1 (1978).

6. M. S. Wrighton, Acc. Chem. Res. 12, 303 (1979).

7. W. Schockley, Electrons and Holes in Semiconductors, Princeton, D. Van Nostrand Co., Inc., 1950.

8. S. M. Sze, Physics of Semiconductor Devices, Chapter 2, Wiley-Interscience, New York, 1969.

9. F. Gutmann and L. E. Lyons, Organic Semiconductors, Chapter 1, John Wiley & Sons, Inc., New York, 1967.

10. G. Heiland, Solid State Physics, Vol. 8, edited by F. Seitz and D. Turnbull, Academic, New York, 1959, p. 191.

11. T. Freund and W. P. Gomes, Catal. Rev. 3(1), 1 (1969).

12. J. F. Dewald, J. Phys. Chem. Solids 14, 155 (1960).

13. V. Myamlin and Y. Pleskov, Electrochemistry of Semiconductors, Plenum Press, New York, 1967.

14. F. Lohmann, Z. Naturforsch. 22a 813 (1967).

15. F. Lohmann, Ber. Bunsenges. Physik. Chem. 70, 87, 428 (1966).

16. M. Spitler and M. Calvin, J. Chem. Phys. 66, 4294 (1977), 67, 5193 (1977).

17. M. Matsumura, Y. Nomura and H. Tsubomura, Bull. Chem. Soc. Japan 50, 2533 (1977).

18. C. W. Bunn, Proc. Phys. Soc. (London) 47, 835 (1935).

19. H. Tsubomura, M. Matsumura, Y. Nomura, and T. Amamiya, Nature 261, 402 (1976).

20. B. Pettinger, H.-R. Schoppel, T. Yokoyama, and H. Gerischer, Ber. Bunsenges. Physik. Chem. 78, 450, 1024 (1974).

21. Assuming a one-sided abrupt junction, the total depletion width may be computed from the following equation:

$$W = \sqrt{\frac{2 \varepsilon_s V}{q N_D}}$$

where ε_s the dielectric constant, V is the biased voltage, q is the electron charge, and N_D is the dopant density. ε_s is assumed to be 12 for the sintered ZnO electrode.

22. A. Heller and B. Miller, Electrochimica Acta 25, 29 (1980).

23. A. B. P. Lever and J. P. Wilshire, Can. J. Chem. 54, 2514 (1976).

24. M. S. Wrighton, R. G. Austin, A. B. Bocarsly, J. M. Bolts, O. Haas, K. D. Legg, L. Naduo, M. C. Palazzotto, J. Am. Chem. Soc. 100 1602 (1978).

25. A. J. Bard, Science 207, 139 (1980).

CHAPTER VI

ELECTROCHEMICAL STUDIES OF MANGANESE(III) PORPHYRIN

The recent discovery that manganese porphyrin may provide reactive oxygen atoms for the oxidation or epoxidation of substrates has stimulated this further investigation of the redox chemistry of manganese porphyrin [1]. The specific objective of this study is to characterize the oxidation product of Mn(III) porphyrin by electrochemical techniques. Prior to this study, the oxidation product of manganese hematoporphyrin IX in alkaline aqueous solution was assigned to be Mn(IV) porphyrin based on the absorption spectrum of the oxidized product, whereas that of MnOEP(OH) in butyronitrile was assigned to be a porphyrin cation based on the separation of the reduction potentials of the first ring oxidation and reduction [2]. Since both assignments were based mainly on empirical reasons, the difference might be ascribed to the different media or different axial ligands used [3].

Experimental

(1) Materials

Tetrabutylammonium perchlorate (TBAP, Eastman Chemical Co.) was recrystallized twice from ethylacetate and vacuum dried over P_2O_5 at room temperature. Methylene chloride ('Baker Analyzed' HPLC reagent) was used without further purification. MnTPP(CH_3CO_2) was from Strem Chemical Inc. and MnTPP chloride was synthesized by the method of Adler et al. [4].

(2) Experimental procedure

Cyclic voltammetric measurements were obtained with a PAR Model 173 potentiostat and a PAR Model 175 universal programmer. IR compensation was applied in most cases. Details of this technique and

the use of thin-layer optically transparent electrodes have been described in Chapter 2.

Spectral measurements were made on a Cary 118 Spectrophotometer. All spectral and electrochemical measurements were carried out with solutions containing 0.1 M TBAP. All the potential data reported here were taken with SCE as the reference.

Results and Discussion

Cyclic voltammograms of MnTPP (OAc) were recorded at several scan rates. They displayed two quasi-reversible electron-transfer waves (Figure 1). $E_{1/2}$ of Mn(III)/Mn(II) in CH_2Cl_2 is located at -0.30 V (vs SCE), and that of Mn(IV)/Mn(III) is at +1.18V. They are called quasi-reversible electron transfer reactions because the current is controlled by both the diffusion of reactants and their charge transfer kinetics. In this case, the concentrations of the electro-active species on the electrode surface must be expressed by absolute rate theory instead of the usual Nernst equation. The separation between oxidation and reduction peaks, ΔE_p, can be used to calculate the rate of electron transfer [5] by a numerical solution of the integral equation, which correlates ΔE_p with a dimensionless function ψ given by

$$\psi = \gamma^{\alpha} \cdot k^{\circ} / \sqrt{\frac{\pi n F v}{RT} D}$$

where γ is the square root of the ratio of the diffusion coefficients D_o and D_r, α the transfer coefficient, n the number of electrons transferred from the reactant to the electrode, v the scan rate, k° the heterogeneous rate constant (cm/s), and D the diffusion coefficient of the electroactive species. k° represents the charge transfer rate constant at the standard potential, E°, of the redox couple, and it

Figure 1. Cyclic Voltammograms of Mn(III)TPP•(OAc)

(A) with 1 mM of MnTPP•(OAc) in CH_2Cl_2 solution containing 0.1 M of TBAP at a scan rate of 100 mV/s.

i_p at 1.25 V is ~40 uA.

(B) same as (A) except at several scan rates.

····· , 20 mV/s (i_p = 20 μA)

– – – – , 50 mV/s (i_p = 30 μA)

——— , 100 mV/s (i_p = 44 μA)

—·—· , 200 mV/s (i_p = 62 μA)

Both (A) and (B) were IR compensated.

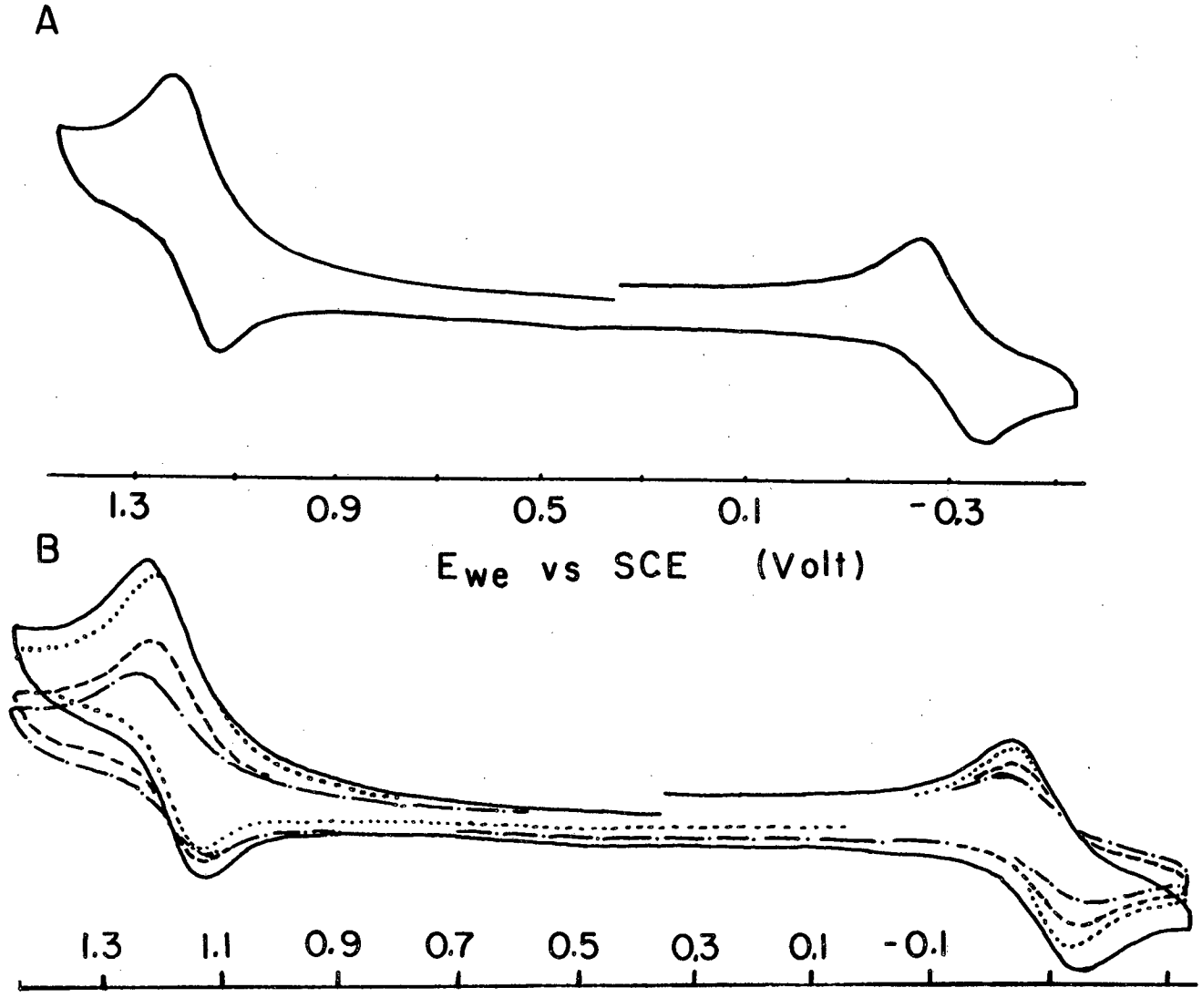

XBL 8110-7078

is writen as k_s in the discussion of the quasi-reversible charge transfer in Chapter 2. Given the value of experimental ΔE_p, k° can be calculated simply by substituting the value of ψ tabulated in the original paper into equation 1.

If D is assumed to be 5 x 10^{-7} cm^2/s, the heterogeneous rate constant, k°, of reaction (2)

$$e^- + Mn(III)TPP\cdot(OAc) \rightleftharpoons Mn(II)TPP\cdot(OAc) \qquad (2)$$

can be estimated to be 0.93 0.09x10^{-3} cm/s, and that of reaction (3)

$$Mn(III)TPP\cdot(OAc) \rightleftharpoons Mn(IV)TPP\ [\text{or } Mn(III)TPP^{+\cdot}] + e^- \qquad (3)$$

is 1.8±0.2 x 10^{-3} cm/s (Table 1).

At present, actual D is not yet available, but it can be measured with a rotating disk electrode. Since D has been reported to be 1 x 10^{-6} cm^2/s for Mn(p-Cl)TPP (Cl) in dimethyl sulfoxide [7], our actual D should be reasonably close to this number. By comparing these two rate constants with those of other metalloporphyrins [6], they are about one or two orders of magnitude lower. For example, k° = 8 x 10^{-2} for ZnOEP/$ZnOEP^{-\cdot}$, 4 x 10^{-2} for ZnTPP/$ZnTPP^{-\cdot}$, and 0.1 cm/s for MgOEP/$MgOEP^{+\cdot}$. However, my data are comparable to the rate constant of Mn(II)OEP/Mn(III)OEP (k° = 6 x 10^{-3} cm/s) and that of Mn(III)(p-Cl)TPP·(Cl)/Mn(II)(p-Cl)TPP in CH_2Cl_2 (k° = 3 x 10^{-3} cm/s from ref. 7). In order to explain this large difference in the rate constants, factors like re-orientation of solvent molecules, change of axial ligands, changes in spin state, and changes in the position of central metal ion must be carefully considered.

Since both Mn(II) and Mn(III) are in their high-spin states and a non-bonding CH_2Cl_2 solvent is used, the most probable factor, which contributes to the slowness of electron-transfer process, is the

TABLE 6 - 1

CALCULATION OF HETEROGENEOUS ELECTRON-TRANSFER RATE CONSTANTS *

$$e^- + Mn(III)TPP\cdot(OAc) \longrightarrow Mn(II)TPP + OAc^-$$

Scan rate (V/s)	ΔE_p (mV)	ψ	k° (cm/s)
0.200	144	0.24	0.84×10^{-3}
0.100	116	0.43	1.07×10^{-3}
0.050	104	0.52	0.91×10^{-3}
0.020	90	0.82	0.91×10^{-3}
		Average	$0.93 \pm 0.09 \times 10^{-3}$

$$Mn(III)TPP\cdot(OAc) \longrightarrow Mn(IV) \text{ or } Mn(III)TPP^{+\cdot} + e^-$$

Scan rate (V/s)	ΔE_p (mV)	ψ	k° (cm/s)
0.200	114	0.45	1.58×10^{-3}
0.100	90	0.82	2.04×10^{-3}
0.050	84	1.00	1.76×10^{-3}
0.020	74	1.85	2.05×10^{-3}
		Average	$1.8 \pm 0.2 \times 10^{-3}$

* In these calculations, α is assumed to be 0.5.

large out-of-plane movement of Mn atom. It has been shown recently that the rate constant of Mn(III)/Mn(II) in dimethyl sulfoxide-imidazole mixed solvent is dependent on the imidazole concentration and varies between 1 x 10^{-3} cm/s in the absence of imidazole and 4 x 10^{-6} cm/s at 0.1 M imidazole. Both axial movement of Mn atom and the displacement of the fifth ligand were suggested to be responsible for the slowest rate constant [7].

The observation of a quasi-reversible wave at +1.18 V seems inconsistent with the data given in a recent paper [8], which reported no additional oxidation or reduction of MnTPP(Cl) up to 1.2 V. Nonetheless, the cyclic voltammogram of MnTPP(Cl) was taken and found a wave at +1.13 V, which was close to the reported reduction potential of the first ring oxidation of MnOEP(OH), +1.12 V [9].

Because all of the ring oxidations and reductions of metalloporphyrins reported (including the ring reduction of MnOEP(OH)) have their k°s larger than 2 x 10^{-2} cm/s, it has been proposed that reactions which involve removing an electron from or donating it to the conjugated π-ring system proceed more rapidly than those in which the electron is added directly to or removed from the central metal [10]. Since the heterogeneous electron-transfer rate constant for the oxidation of Mn(III)TPP^+ is found to be 1.8 0.2 x 10^{-3} cm/s in methylene chloride in this experiment, the rate determining step in the oxidation of Mn(III)TPP(OAc) is deduced to be the removal of an electron from central Mn atom or from a ligand π-orbital which interacts strongly with the d-π orbitals of manganese atom.

In conjunction with electrochemical studies, the optical spectrum of the oxidized product of Mn(III)TPP(OAc) was recorded <u>in situ</u> with a

thin-layer, optically transparent electrode. Within the thin layer electrode, a complete electrolysis of Mn(III)TPP(OAc) could be achieved within a few minutes (Figure 2). The spectra of both Mn(II) and Mn(III) are consistent with the previous data, while that of the oxidation product of Mn(III)TPP(OAc) is unlike that of manganese hematoporphyrin IX in an alkaline aqueous solution [11]. Our spectrum shows broadened and decreased UV bands and a rather broad band between 550 and 700 nm. These features are similar to the π-cations of many metalloporphyrins except that there are two broad UV bands. This doublet seems to be a characteristic of manganese porphyrin and may be attributed to a strong interaction between the π orbital in the ring and the d-π orbitals in the central Mn. Furthermore, when Mn(III) was oxidized or when the oxidized product was reduced back to Mn(III), the absorption at 390 nm first increased and then decreased. This suggests that this electron transfer reaction may not be a single-step process [12 and note].

Since electron spin resonance has been frequently used in the past for the assignments of the oxidation products of porphyrins [13], the epr spectrum of the oxidized Mn(IV)TPP (or Mn(III)TPP$^{+\cdot}$) was once measured. But, no obvious signal down to a liquid nitrogen temperature was observed. In the future, an epr experiment at helium temperature should be performed. Other possible tools for the assignment of the electronic structure are NMR and Raman spectrometry.

Figure 2. Optical spectra of Mn(III)TPP (OAc) and its electrochemially oxidized or reduced compounds in CH_2Cl_2.

(A) ———————, [Mn(III)TPP]·(OAc)

(B) —-—-—-—, [Mn(II)TPP]

(C) ---------, $[Mn(IV)TPP]^{2+}$ or $[Mn(III)TPP^{+\cdot}]$

The insert (D) is taken from reference 1(d) for comparison. O=Mn(IV)TPP is synthesized by oxidizing Mn(II)TPP with iodosobenzene.

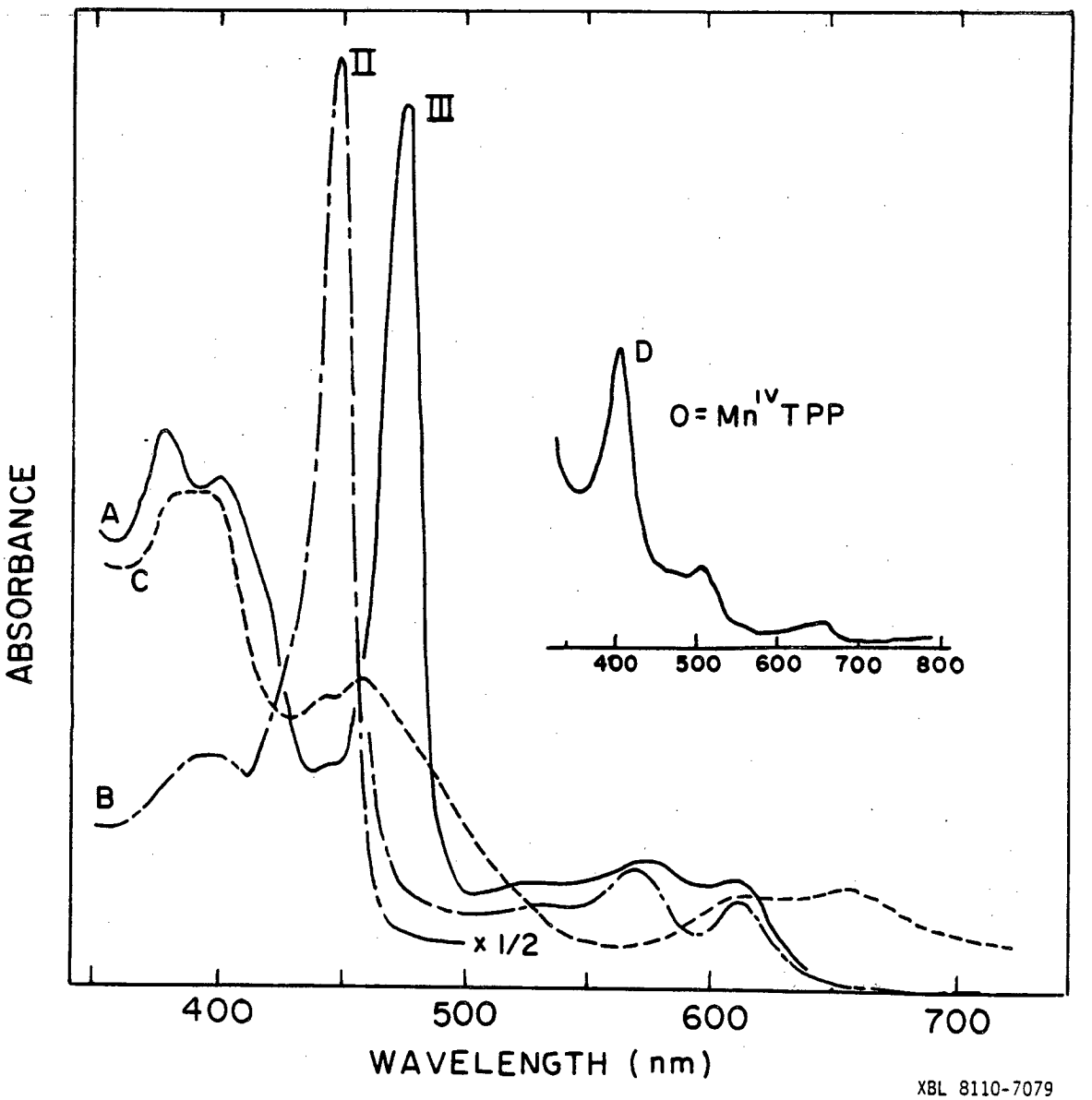
II
III
D
O=Mn^IV TPP
400
500
600
700
800
A
C
B
x 1/2
ABSORBANCE
400
500
600
700
WAVELENGTH (nm)
XBL 8110-7079

References

1. (a) M. Calvin, Science, 184, 375 (1974).

(b) J. T. Groves, T. E. Nemo, R. S. Myers, J. Amer. Chem. Soc., 101, 1032, (1979).

(c) C. K. Chang and M. S. Kuo, J. Amer. Chem. Soc., 101, 3413 (1979).

(d) I. Willner, J. W. Otvos, and M. Calvin, J.C.S. Chem. Comm., 964 (1980).

(e) M. Calvin, 'Synthetic Chloroplasts', in Faraday Discussion of the Royal Society of Chemistry, 70 , 1980.

2. L. J. Boucher, Coord. Chem. Rev., 7, 289 (1972).

3. D. Dolphin, T. Niem, R. H. Felton, and I. Fujita, J. Amer. Chem. Soc., 97, 5288 (1975).

4. A. D. Adler, F. R. Longo, F. Kampas, and J. Kim, J. Inorg. Nucl. Chem., 32, 2443 (1970).

5. R. S. Nicholson, Anal. Chem., 37, 1351 (1965).

6. K. M. Kadish and D. G. Davis, Ann. N. Y. Acad. Sci., 206, 495 (1973).

7. K. M. Kadish, M. Sweetland, and J. S. Cheng, Inog. Chem., 17, 2795 (1978).

8. K. M. Kadish and S. Kelly, Inorg. Chem., 18, 2968 (1979).

9. J.-H. Fuhrhop, K. M. Kadish, and D. G. Davis, J. Amer. Chem. Soc., 95, 5140 (1973).

10. K. M. Kadish, M. M. Morrison, L. A. Constant, L. Dickens, and D. G. Davis, J. Amer. Chem. Soc., 98, 8387 (1976).

11. M. Calvin, P. A. Loach, and A. Yamamoto, in 'Theory and Structure of Complex Compounds', ed. B. Jezouska-Trzebistowska, Macmillam (Pergamon), New York, 1964, p. 13.

12. (a) I. Tabushi and S. Kojo, Tetrahedron Letters, 17, 1577 (1974).
(b) I. Tabushi and N. Koga, J. Amer. Chem. Soc., 101, 6456 (1979).

Note: The spectral changes observed in the electrochemical experiment with the optically transparent electrode are very similar to what Tabushi and Koga observed in ref 12(b). They suggested that one was $Mn(IV)\cdot O^{2-}$ and the other was $Mn(III)\cdot O^{-}$. Since both water and oxygen were excluded in my experiment, the intermediates would not be the same as those suggested by Tabushi. Nonetheless, we may conclude that the difference in reduction potential of these two intermediates in the reaction is very small.

13. (a) D. Dolphin and R. H. Felton, Acc. Chem. Res., 7, 26 (1974).
(b) R. H. Felton, 'Primary Redox Reactions of Metalloporphyrins' in 'The Porphyrins', ed. D. Dolphin, Vol. V, Part C, p. 53, Academic Press, New York (1979).
(c) J. Fajer and M. S. Davis, 'Electron Spin Resonance of Porphyrin Cations and Anions', in 'The Porphyrins', ed. D. Dolphin, Vol. IV, p. 197, Academic Press, New York (1979).

This report was done with support from the Department of Energy. Any conclusions or opinions expressed in this report represent solely those of the author(s) and not necessarily those of The Regents of the University of California, the Lawrence Berkeley Laboratory or the Department of Energy.

Reference to a company or product name does not imply approval or recommendation of the product by the University of California or the U.S. Department of Energy to the exclusion of others that may be suitable.

TECHNICAL INFORMATION DEPARTMENT
LAWRENCE BERKELEY LABORATORY
UNIVERSITY OF CALIFORNIA
BERKELEY, CALIFORNIA 94720